DTIC
S ELECTE
MAR 6 1992
C D

CASS REPORT # GR-013

MEASUREMENTS OF MESOSPHERIC WINDS
AND WAVES

by

G.W. Adams, J.W. Brosnahan, and R.G. Roper

January 21, 1992

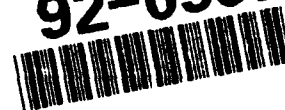FINAL REPORT: AIR FORCE OFFICE OF SCIENTIFIC RESEARCH
CONTRACT # F49620-89-C-0022

DISTRIBUTION STATEMENT A
Approved for public release;
Distribution Unlimited

UTAH STATE UNIVERSITY

CENTER FOR ATMOSPHERIC AND SPACE SCIENCES
UTAH STATE UNIVERSITY • LOGAN • UTAH • 84322

92 3 03 052

REPORT DOCUMENTATION PAGE

Form Approved
OMB No. 0704-0188

1a. REPORT SECURITY CLASSIFICATION Unclassified	1b. RESTRICTIVE MARKINGS
2a. SECURITY CLASSIFICATION AUTHORITY	3. DISTRIBUTION/AVAILABILITY OF REPORT Approved for public release; distribution unlimited.
2b. DECLASSIFICATION/DOWNGRADING SCHEDULE	
4. PERFORMING ORGANIZATION REPORT NUMBER(S) GR-013	5. MONITORING ORGANIZATION REPORT NUMBER(S) AFOSR·TR· 92 0019

6a. NAME OF PERFORMING ORGANIZATION Utah State University Center for Atmos. & Space Sci.	6b. OFFICE SYMBOL (If applicable)	7a. NAME OF MONITORING ORGANIZATION AFOSR/NL
6c. ADDRESS (City, State, and ZIP Code) Logan, UT 84322-4405		7b. ADDRESS (City, State, and ZIP Code) Building 410 Bolling AFB DC 20332-6448
8a. NAME OF FUNDING/SPONSORING ORGANIZATION Air Force Office of Scientific Research	8b. OFFICE SYMBOL (If applicable) NL	9. PROCUREMENT INSTRUMENT IDENTIFICATION NUMBER F49620-89-C-0022

8c. ADDRESS (City, State, and ZIP Code)	10. SOURCE OF FUNDING NUMBERS			
	PROGRAM ELEMENT NO.	PROJECT NO.	TASK NO	WORK UNIT ACCESSION NO
Building 410 Bolling AFB, DC 20332-6448	61102F	2310	A2	

11. TITLE (Include Security Classification)

MEASUREMENT OF MESOSPHERIC WINDS AND WAVES

12. PERSONAL AUTHOR(S) Adams, Gene W.; Brosnahan, John W., LaSalle Research Corp.;
Roper, Robert G., Georgia Institute of Technology

13a. TYPE OF REPORT Final	13b. TIME COVERED FROM 12/88 TO 1/92	14. DATE OF REPORT (Year, Month, Day) 1992 January 21	15. PAGE COUNT 94

16. SUPPLEMENTARY NOTATION

17.	COSATI CODES		18. SUBJECT TERMS (Continue on reverse if necessary and identify by block number)
FIELD	GROUP	SUB-GROUP	

19. ABSTRACT (Continue on reverse if necessary and identify by block number)
An imaging doppler interferometer (IDI) radar was operated during the three AIDA '89
campaigns in Puerto Rico over the period March through May of 1989. The output of the
IDI analysis characterizes radar scattering in terms of a number of discrete "scattering
points," also referred to as "multiple scattering centers," IDI/MSC for short. For each
of these points the three-dimensional location, radial velocity, and amplitude and phase
are determined, similar to the output of meteor radars. A detailed discussion of the
technical aspects of the AIDA campaign, together with preliminary results, have been
accepted for publication in the AIDA Special Issue of the Journal of Atmospheric and
Terrestrial Physics (1992), and appear here as Appendix A. We have applied the conventional
Groves' [1959] meteor wind radar analysis to the scattering points to produce the mean
apparent motions over the height range from 70 to 110 km; these results have also been
accepted for publication in the AIDA Special Issue, and are included here as Appendix B.
The mean apparent motion of the scattering centers is the quantity that would correspond to
the neutral atmosphere wind or bulk motion if the scattering points are physical entities

20. DISTRIBUTION/AVAILABILITY OF ABSTRACT ☒ UNCLASSIFIED/UNLIMITED ☐ SAME AS RPT ☐ DTIC USERS	21. ABSTRACT SECURITY CLASSIFICATION
22a. NAME OF RESPONSIBLE INDIVIDUAL JAMES G. STOBIE, Lt Col, USAF	22b. TELEPHONE (Include Area Code) (202) 767-5021	22c. OFFICE SYMBOL NL

19. (such as turbulent eddies) whose motions are determined solely by advection. This is the quantity which is tested as the "wind" in the analysis in Appendix B, and which should be compared to the wind measurements as deduced from the other methods employed during this campaign. There is, however, a caveat which supports the contention of Hines, et al [1992] that extreme care must be used in interpreting the velocities measured by partial reflection radars as winds. While simultaneous measurements by the Geospace Research meteor radar (unfortunately, only one hourly mean is available for comparison) show agreement over the 70 to 95km range of measurement of the incoherent scatter radar, the IDI comparisons differ significantly above 80km. The longer term prevailing winds and tides resulting from analysis of the IDI data, however, appear sound, based both on theoretical predictions of tidal phase, and previously measured wind climatologies. The current application of the Groves method of analysis has revealed motions from which one would infer a typical equatorial easterly circulation, with mean meridional circulation becoming significant only above 96km. A periodogram analysis of the complete data interval (April 5 - April 11) has shown the diurnal tide to be the most significant feature of the wind field at these altitudes, with zonal amplitudes up to some 50m/s and meridional amplitudes approximately half this value. The 12 and 6 hour tides become as significant as the diurnal above 100km. The two-day (48+-5hr) wave is the next most significant feature, with zonal amplitude increasing with height up to 30m/s at 110km. However, analysis on a day by day basis reveals a significant semi-diurnal component which is not phase coherent over the total interval. Mean vertical velocities are of the order of tens of centimeters per second, and are considered to be more realistic than the meters per second velocities usually inferred from analyses of meteor trail drifts.

MEASUREMENTS OF MESOSPHERIC WINDS
AND WAVES

ABSTRACT An imaging Doppler interferometer (IDI) radar was operated during the three AIDA '89 campaigns in Puerto Rico over the period March through May of 1989. The output of the IDI analysis characterizes radar scattering in terms of a number of discrete "scattering points," also referred to as "multiple scattering centers," IDI/MSC for short. For each of these points the three-dimensional location, radial velocity, and amplitude and phase are determined, similar to the output of meteor radars. A detailed discussion of the technical aspects of the AIDA campaign, together with preliminary results, have been accepted for publication in the AIDA Special Issue of the Journal of Atmospheric and Terrestrial Physics (1992), and appear here as Appendix A. We have applied the conventional Groves' [1959] meteor wind radar analysis to the scattering points to produce the mean apparent motions over the height range from 70 to 110km; these results have also been accepted for publication in the the AIDA Special Issue, and are included here as Appendix B.. The mean apparent motion of the scattering centers is the quantity that would correspond to the neutral atmosphere wind or bulk motion if the scattering points are physical entities (such as turbulent eddies) whose motions are determined solely by advection. This is the quantity which is treated as the "wind" in the analysis in Appendix B, and which should be compared to the wind measurements as deduced from the other methods employed during this campaign. There is, however, a caveat which supports the contention of Hines et al [1992] that extreme care must be used in interpreting the

velocities measured by partial reflection radars as winds. While simultaneous measurements by the Geospace Research meteor radar (unfortunately, only one hourly mean is available for comparison) show agreement over the 70 to 95km range of measurement of the incoherent scatter radar, the IDI comparisons differ significantly above 80km. The longer term prevailing winds and tides resulting from analysis of the IDI data, however, appear sound, based both on theoretical predictions of tidal phase, and previously measured wind climatologies. The current application of the Groves method of analysis has revealed motions from which one would infer a typical equatorial easterly circulation, with mean meridional circulation becoming significant only above 96km. A periodogram analysis of the complete data interval (April 5 - April 11) has shown the diurnal tide to be the most significant feature of the wind field at these altitudes, with zonal amplitudes up to some 50m/s and meridional amplitudes approximately half this value. The 12 and 6 hour tides become as significant as the diurnal above 100km. The two-day (48+-5hr) wave is the next most significant feature, with zonal amplitude increasing with height up to 30m/s at 110km. The semidiurnal tide is not at all well developed below 100km. However, analysis on a day by day basis reveals a significant semidiurnal component which is not phase coherent over the total interval. Mean vertical velocities are of the order of tens of centimeters per second, and are considered to be more realistic than the meters per second velocities usually inferred from analyses of meteor trail drifts.

References.

Brosnahan, J.W., and G.W. Adams, "The MAPSTAR imaging Doppler interferometer (IDI) radar: system description and first wind comparisons,"accepted for publication in the AIDA Special Issue of J. Atmos. Terrest. Phys., 1992, (see Appendix A).

Groves, G.V., "A theory for determining upper atmosphere winds from radio observations on meteor trails," J. Atmos. Terrest. Phys. 16, 344-356, 1959.

Hines, C.O., Gene W. Adams, John W. Brosnahan, Frank T. Djuth, Michael P. Sulzer, Craig A. Tepley, and Joel S. Van Baelen, " Mesospheric wind and partial reflection observations: comparisons and interpretations,"accepted for publication in the AIDA Special Issue of J. Atmos. Terrest. Phys., 1992,

Roper, R.G., G.W. Adams and J.W. Brosnahan,"Tidal Winds at Mesopause Altitudes Over Arecibo (18N,67W), April 5 - 11, 1989 (AIDA'89)," accepted for publication in the AIDA Special Issue of J. Atmos. Terrest.Phys., 1992, (see Appendix B).

iv

APPENDIX A

"The MAPSTAR imaging Doppler interferometer (IDI) radar:
description and first results,"

by

J.W. Brosnahan and G.W. Adams

The MAPSTAR Imaging Doppler Interferometer (IDI) Radar: Description and First Results

J.W. Brosnahan(1) and G.W. Adams(2)

(1) La Salle Research Corp.
   24115 WCR 40
   La Salle, CO 80645-9522

(2) Utah State University
   Logan, UT 84322-4405

Abstract

MAPSTAR is a medium-frequency imaging Doppler interferometer (IDI) radar. In this paper we describe the radar and present results from 34½ hours of data taken during the AIDA campaign in Puerto Rico during April 1989.

The IDI method uses several independent antennas and receivers, pulsed sounding, range-gating, Doppler sorting and spatial interferometry to determine a three-dimensional Doppler image of the rf scatterers within the volume being illuminated. The analysis characterizes any perturbation in the *index of refraction* that returns rf energy (clear-air turbulence, scattering from striations, meteor trails, etc.) in terms of the three-dimensional locations, Doppler velocities, and scattering amplitudes and phases of a number of apparent points in space, called "scattering points". Scattering points are defined as those Fourier voltages whose phases on the several antennas agree on the direction in the sky of the source of that spectral power. We find that most of the power scattered from the mesosphere and E region can be described in this fashion. This allows us to replace, say, 10 complex voltages by two voltages and two coordinates locating the source. The IDI characterization is therefore, *en passant*, a data-compression technique, reducing the data volume by a factor of 25-30 without losing any significant information. However, if we can so easily characterize the data <u>as if</u> discrete scattering points were responsible, the obvious question is: What physical processes do these scattering points actually represent? We don't complete an answer this question here, but we do begin an answer with a description of some of their properties and behavior.

We present in Section 2 a description of the hardware as designed, and in Section 3 a description of its deployment in Puerto Rico, where the radar was tuned to 3.175MHz and used the Arecibo Heating Facility's transmitters and transmitting antennas. In Section 4 we show the time-domain data, in which the E region and several distinct mesospheric regions can be seen. We show the power vs altitude profile, which is typical of medium-frequency

returns, and describe the phase behavior of the returns, which can be used for tracking discrete targets such as TIDs and meteors. We describe in Section 5 the IDI algorithm, which involves Fourier transforming the several independent data streams and examining (for each pulse series, at each range gate, and at each Fourier frequency) the phases of the 10 complex Fourier voltages. When it is sufficiently accurate to represent the phase variations along the two linear distributions of antennas as linear with distance, we replace the 10 complex voltages with two voltages and two phase gradients. The data are thus cast into a form that is most easily interpreted as the result of scattering from a number of simultaneous discrete points. In Section 6 we describe some of the properties of these scattering points. The polarization properties of the points are shown first, since this is used for filtering the results that follow. We show the distribution of radial velocities with altitude for the ordinary, extraordinary, and linear modes. The radial velocities show the characteristic mesospheric-scattering distribution of the ordinary-mode points (which was the transmitted mode), contrasted with the near-random distributions of the linear and extraordinary-mode points. This justifies the use of polarization filtering and introduces a powerful new filtering technique. Next we show the combined power of the scattering points (the "recovered" power) and its variation with altitude and time. The recovered power looks very much like the raw power as usually seen by medium-frequency radars (one to several mesospheric regions plus the E region), except that it has somewhat better altitude resolution (being in altitude rather than range), and better low-altitude coverage due to $\approx 10dB$ better signal/noise. Skymaps of the scattering points (i.e., their locations in the horizontal plane) are shown at several altitudes, showing the varying spread, and sometimes asymmetry, in their distribution. We then show the variation of the recovered power with zenith angle, demonstrating the aspect sensitivity of the returns, from nearly specular at 60-80km, spreading out to a maximum around 90-100km, and contracting sharply to very mirror-like above that. The motions of the scattering points are explored with contour maps of horizontal layers, and by calculating their three-dimensional mean motions. Estimates of the calculational uncertainties are made for the locations and motions of the points.

Table of Contents

1. Introduction

Radar interferometry has its roots in optical interferometry, although radar's lower frequencies make digital signal processing possible in ways just becoming available to the optical community. The optical use of simultaneous rays from two slits to generate light and dark bands ("interference fringes") has been known since the earliest days of the field. According to Loewenstein's [1966] review, the earliest use of interference spectroscopy was by Fizeau in 1862. Michelson [1890a] pointed out the possibility of using those fringes for precision location measurements, and in a series of papers [e.g., Michelson, 1890b, 1920; Michelson and Pease, 1921] applied them to astronomical measurements. Again according to Loewenstein, the first true interferogram was published in 1911 by Rubens and Wood, while Fellgett in his 1951 thesis at the University of Cambridge established the field quantitatively and showed the first numerically Fourier transformed interferogram. One principal advantage of Fourier-transform techniques, known as "Fellgett's advantage" [e.g., Mertz, 1965], is the increased system throughput that accrues because energy from the entire spectral region is gathered simultaneously.

The use of interference effects at radio wavelengths followed within a few decades. Hertz noticed the effects of nearby objects on his early propagation experiments in 1886; Tesla described his vision of electromagnetic location and ranging measurements by analogy with acoustic echoes; and a "telemobiloscop" was patented by Christian Hulsmeyer in 1904, after a successful demonstration from a river bridge, ringing a bell at the approach of ships [Fisher, 1988, pp. 42-43]. Although Breit and Tuve [1926] had begun the pulsed-radar exploration of the "conducting layer", it remained for World War II to provide the motivation for the rediscovery and practical development of these ideas. The first operational radars, the Chain Home stations that defended the British Isles, were crude interferometers: the ratios of signals received by antennas atop and half-way up the towers, each receiving both direct and ocean-bounce returns from aircraft, were empirically calibrated to determine aircraft altitudes [Fisher, 1988, pg. 119].

Spatial Fourier interferometry as an optical-analog radar technique has found application in astrometry, as realized, for example, in very-long-baseline measurements [e.g., Thompson et al., 1986]. The method requires the motion provided by the Earth's rotation, and increases resolution by maximizing the number of unique spacings between antennas.

Doppler interferometry operates digitally in a temporal, rather than spatial, Fourier space, so that a single antenna pair is adequate for some research, although, as we discuss below, a considerable increase in noise rejection and temporal resolution,

1

as well as three-dimensionality, is achieved by a modest increase in the number of antennas. The form of interferometry used in radio astronomy puts a premium on maximizing the number of antenna spacings; Doppler interferometry's need for an analogous variety of unique temporal spacings is obviated by the ease and modest incremental cost of transmitting, receiving, and analyzing many equally spaced pulses.

Time-domain Fourier (Doppler) interferometry was first suggested for use in the ionosphere by Pfister [1971], and implemented by Farley and coworkers at Cornell University [Farley et al., 1981; Kudeki et al., 1981; Providakes et al., 1983] and on the SOUSY radar [Ierkic and Röttger, 1984; Röttger and Ierkic, 1985]. It was developed into a three-dimensional imaging system, named IDI (imaging Doppler interferometry), and demonstrated as a partial-reflection technique in the mesosphere by Adams et al. [1985; 1986], using a modified digital ionosonde that operated at Boot Lake, Colorado. Doppler interferometry has also been applied to the mesosphere by Meek and Manson [1987a,b] and Kudeki and Stitt [1987].

In the mesosphere at medium frequencies there is a plurality of strong scatterers too closely spaced to be resolved by practical antenna beams; this is the fundamental motivation for using interferometric, rather than beam-forming, techniques. While a number of authors have speculated about the nature of the mesospheric "partial-reflection" scatterers [Gardner and Pawsey, 1953; Hines, 1960; Gregory, 1961; Belrose and Burke, 1964; Piggott and Thrane, 1966; Flood, 1968; Austin et al., 1969; Austin and Manson, 1969; Gregory and Manson, 1969; Manson et al., 1969; von Biel, 1971; Beer, 1972; Tanenbaum et al., 1973; Newman and Ferraro, 1973; Cohen and Ferraro, 1973; Mathews et al., 1973; Manson et al., 1973; Harper and Woodman, 1977; Schlegel et al., 1978; Schlegel et al., 1980; Jones and Grubb, 1980; Rastogi and Holt, 1981; Jones et al., 1982], only the large steerable arrays near Adelaide [Hocking, 1979] and Brisbane, Australia [Jones, 1980] have had even modest success at resolving these scatterers. The measurement problem arises because beamwidth narrows only as antenna aperture grows, and 100m wavelengths want several-kilometer arrays for adequately narrow beams. Interferometry is a solution that achieves the requisite resolution with practical antenna arrays.

The IDI analysis accomplishes a considerable compression of the data volume without significant loss of information in the course of casting the measurements into an easily interpretable form. The data sets from the several antennas are first subjected to independent complex Fourier transforms, in which no information is lost since the original complex data can be recovered by performing the inverse transforms. We observe in the mesospheric data that the phase gradients of the spectral windows across the antenna arrays are often constant, so that the transformed voltages from a row of antennas can be represented by one complex voltage

2

and the phase gradient for that row. We chose to represent the phase gradients along two orthogonal rows of antennas by the apparent cardinal elevation angles of the source of the scattered energy in the spectral window, since the simplest physical interpretation of the source of a constant phase gradient is a point scatterer. Spectral elements that fail to show sufficiently constant phase gradients along the two rows are discarded; those kept can be inversely transformed to recover most, if not all, the information available in the original data. The essence of the process lies in Pfister's [1971] insight that the phase difference between a pair of antennas is preserved in a complex Fourier transformation; the spectral phase simply represents the phase of the spectral component at t=0, so that the physical interpretation of a phase difference as a time-of-flight difference is not changed by the transformation from temporal to frequency domains.

The IDI algorithm thus represents the interferometer data as the result of scattering from a number of discrete scattering points, each characterized by its three-dimensional location, its radial velocity, and its amplitudes and phases on two orthogonal reference dipoles. The initial question this representation poses is: What physically is represented by these scattering points? Glints on shimmering surfaces, advected turbulent eddies, small meteors, and traveling wind shears causing electron bunching are four possibilities that come easily to mind. We begin to approach the question here by examining the properties of the scattering points. We show in passing that there are a number of practical benefits to the IDI characterization of the data, including the ability to polarization-filter the individual spectral elements.

The benefits of the IDI method for handling interferometer-radar data were first demonstrated on a modified digital ionosonde supplemented by a large tuned antenna array and transmitter [Adams et al., 1985, 1986] that operated at Boot Lake, Colorado. The mean apparent motions of the scatterers were shown to resemble winds, but individual wave events were also observed in both the D and E regions [Adams et al., 1988a,b]. After the IDI technique had been demonstrated with the 2.66MHz prototype, construction began on a dedicated tuneable and portable version with enough on-line computational power to give real-time results, and on a VHF version that could explore the clear-air scattering from the troposphere and stratosphere as well as from mesospheric meteor echoes. As a result, two imaging radars, MAPSTAR (Middle Atmosphere Periodic Structure Associated Radiance) and MENTOR (Meteor Echoes; No Transmitter, Only Receivers), were built in parallel to a common design.

The MAPSTAR radar is tuneable from 2-5MHz, and was tuned to 3.175MHz for the measurements in Islote, Puerto Rico, where MAPSTAR's pulse-forming and control circuitry was connected to the NAIC Heater Facility's transmitters and transmit antenna. Time-domain data were received on MAPSTAR's 10 dipoles, coherently

3

averaged, and recorded on magnetic tape so that they could be analyzed with the IDI algorithms, with the spaced-antenna algorithms, and with other interferometric approaches.

This report includes a description of the hardware both as designed and as deployed in Puerto Rico, a discussion of the data-analysis methods, and a survey of the characteristics of the data. Papers elsewhere in this issue examine some particular properties of the scattering points in more detail. The mean apparent motions of the scattering points are compared [Hines et al., this issue] with the winds measured simultaneously by the Arecibo 430MHz radar, whose antenna beam was steered to intersect the MAPSTAR beam at 85km altitude, a 50MHz meteor radar, a Fabry-Perot interferometer, and the MAPSTAR data set analyzed by spaced-antenna and other interferometric methods. Also in this issue are derived the tidal components from the mean apparent motions of the scatterers [Roper et al., this issue].

2. Hardware Description

This section describes the MAPSTAR radar as designed and built. Particular choices and modifications that were made for operation in Puerto Rico are described in the following section.

The MAPSTAR IDI radar is comprised of a clock and pulse-generation circuitry, a 150kW transmitter and antenna, 10 receiving channels, and a data-processing complement. Each receiving channel consists of a short-dipole antenna, a receiver, and a dedicated high-speed data processor (the Complex Channel Processor, or CCP). Each CCP includes three TMS-320C25 processors: two for coherent averages, the third for FFTs. The analysis complement is a 68020 CPU, a Sky Warrior array processor, and a Macintosh II for graphics. The full system travels in two 8'x8'x20' shipboard containers, which become the operations buildings when the radar is deployed.

2.1 System Deployment. The antenna deployment for MAPSTAR is shown in Fig. 1. Normally, the two shipboard containers are used as electronics housings and operations buildings: one for the transmitter, located at the transmit antenna; the other for the receiver/computer electronics, located near the vertex of the L-shaped receiving array of five crossed dipole-pairs. Communication between the two locations is by coaxial cable.

2.2 Transmitters. The MAPSTAR transmitter produces 150kW peak (10kW average) power using a pair of Eimac 3CX5000A7 grounded-grid triodes. An Eimac 3CX1200A7 provides up to 10kW peak drive and a solid-state amplifier chain provides the required 1kW peak predriving power. System monitoring and control is provided by an 8051 microprocessor that allows remote operation of the transmitter at a distance of up to 800m.

4

2.3 Transmit Antenna. MAPSTAR uses a pair of broadbanded crossed dipoles supported by a single 30m tower at the center. The dipoles are fan-shaped to increase VSWR bandwidth and are mounted with the ends near the ground for simplicity. The dipoles may be driven to provide orthogonal linear polarizations or left-hand and right-hand circular polarizations. The antenna pattern is essentially that of a dipole located $\lambda/4$ above ground. The transmit (and receive) antennas are deliberately broad-patterned, as the IDI process makes use of a large viewed volume.
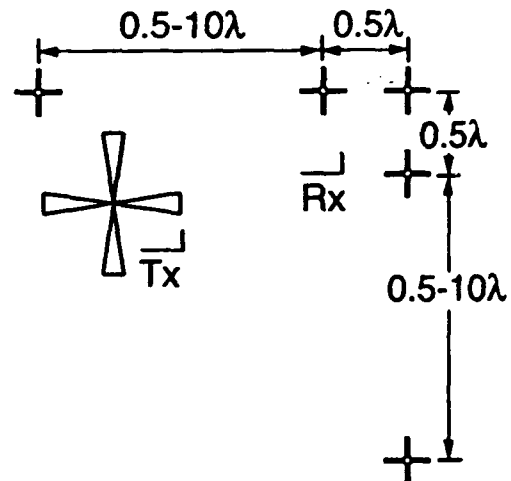
Figure 1. Typical deployment of the MAPSTAR IDI radar, showing the transmitter (Tx) building and antenna, and the separate receiving (Rx) building and antennas.

2.4 Receive Arrays. MAPSTAR uses 10 voltage-probe linear dipoles, each 7m long, for receiving. These are arrayed as five crossed dipoles as shown in Fig. 1. Each linear dipole is treated as an independent interferometer element; each is connected to its own receiver and data processor. The dipoles are located 3m above the ground and are typically deployed in an "L" configuration, providing six interferometer elements in each plane by sharing the two vertex dipoles. The receiving array, like the transmit antenna, is small and broad-beamed.

2.5 Receivers. MAPSTAR uses an up-conversion receiver technique to provide image rejection over its 2-5MHz operating range. Its intermediate frequency is 7.5MHz and, after phase detection, either of two bandwidths may be selected by choosing the appropriate linear-phase fifth-order Bessel filters. The operating frequency is generated by a phase addition synthesis, and two oscillators allow pulse-to-pulse frequency agility in 1Hz steps. Ten receiver channels are incorporated to allow flexibility in selecting operating modes. The receivers can be configured to individually receive the 10 dipoles to allow all polarizations to be available through digital processing in the computer system. The receivers can also be used to process the five left-hand polarization and the five right-hand polarization signals simultaneously when the antenna system is configured in this mode. In addition, the receiver may be configured in such a way that five receivers are active at one frequency while the remaining five receivers are active at a second frequency for more complex modes of operation. The appropriate transmit pulses are generated within the receiver. The receiver contains an 8051 controller/monitor processor for function control.

5

Table I. Complex-Channel Processor.

Analog
Channels:	2
Precision:	12 bits
Rate:	1 μsec per sample, each channel

Processing
Processors:	(3X) Texas Instruments TMS320C25
Clock Rate:	20MHz

Memory
Word Size:	16 bits
Raw Buffer:	(2X) 16K words, 35 nsec
Shared Buffer:	256K words, 45 nsec
Output Buffer:	64K words, 45 nsec
Program:	TDA processors: (2X) 4K words, 45nsec
	FFT processors: 8K words, 45nsec

Computer Interface
Bus:	IEEE 1014 (VMEBus)
Capability:	A24, D16 bus master, interrupt and DMA

2.6 Complex-Channel Processors. The complex-channel processor (CCP) is a general-purpose digital signal processing engine in a single oversized Eurocard format. Up to 10 CCPs may be used in a single radar system. Principal specifications are shown in Table I. The host processor (68020) downloads code to the CCPs in the system, and sets up the DMA controllers for transferring out the desired product. The CCPs then operate semi-autonomously as independent processing pipelines, digitizing analog data from the receiver channels and placing the specified output products in the main system memory.

2.7 General-Purpose Computers. Once the data are on the VMEBus, they can be accessed by the three general-purpose computers in the system: a Motorola 68020, a Sky Warrior Array Processor, and a Macintosh II for real-time graphics. (Fig. 8 was done with the Macintosh II, in a format that is being implemented as a real-time display along with a continuously scrolling stacked-phase plot like Fig. 4.)

3. Operations in Puerto Rico

For the AIDA campaign in Puerto Rico we operated at the NAIC Ionospheric Heater Facility (18°28'33"N; 66°39'55"W) at Islote, P.R. We used the Heater Facility's transmitters, transmit antennas, and building; rf pulses were supplied to the transmitter from MAPSTAR's pulse-generation circuitry. Operation was at 3.175MHz (λ=94.5m), which was the optimum heater frequency. Deployment was as shown in Fig. 2. In order to fit into the available space around the building and to coexist with a spaced-antenna-drift (SAD) antenna array, which was quite close, the receiving array was oriented so that the vertex of the "L" pointed north, and the antennas were spaced at λ/2 along each arm of the interferometer. This gave about 70m separation between the transmit antenna and the receiving array. Since we use no transmit-receive switches, relying on a minimally bistatic arrangement, and since the peak power was set at the maximum for continuous operation, this was uncomfortably close.
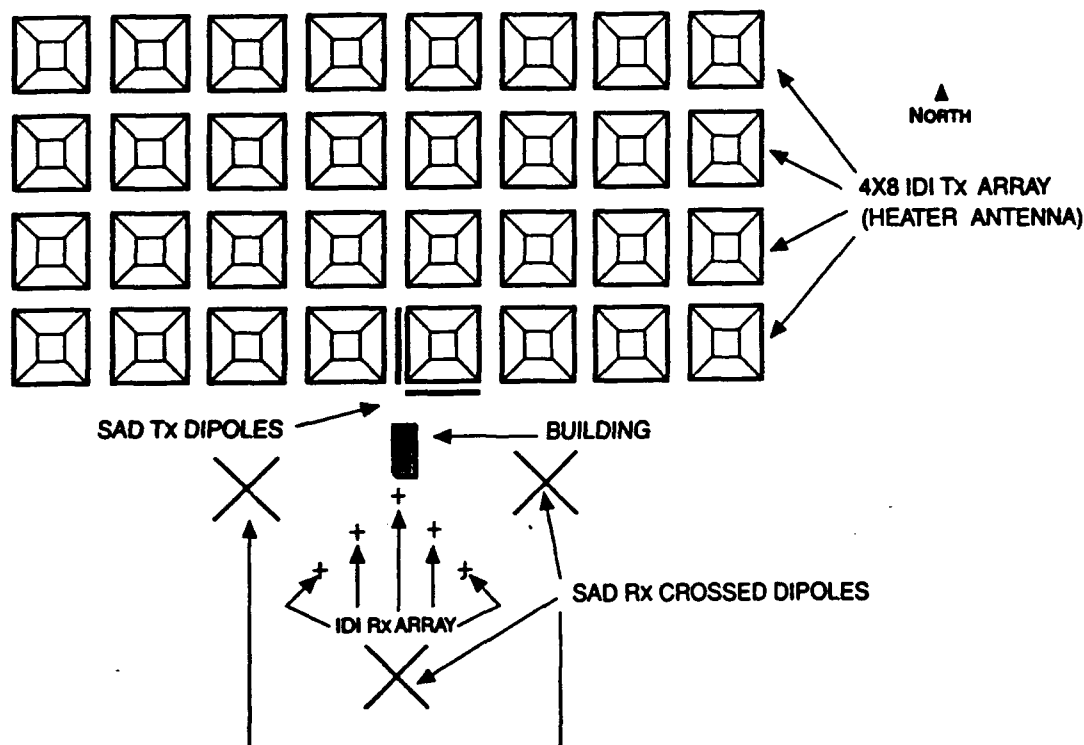
Figure 2. The MAPSTAR radar's deployment at the Arecibo Heating Facility, where we used half the large 4x8 heater array as our transmit antenna, and received on five crossed dipoles (just south of the operations building and nestled into the spaced-antenna array).

The AIDA program ("Multimethod measurement of motions at 10-110km heights") consisted of three measurement periods, labeled AIDA Act '89, Scenes I, II, and III. The dates were 7-15 March, 28 March-11 April, and 1-9 May, 1989. The operating periods started and stopped at local noon (1600UT).

Typical operation involved running two of the four transmitters at a time to one-half of the array for 24 hours while the other two transmitters and their diesel generators underwent maintenance. Typical power output varied from 75 to 150kW per transmitter during the course of three operating periods, and was about 100kW for the data presented here. The first of the three campaigns was used to debug the radar since this was its first deployment. Although there are some good data from this period, most future data analysis will be confined to the second and third periods, and the data presented here come from the final 34½ hours of the second campaign.

The operating characteristics of the radar, both as designed and as implemented in Puerto Rico, are shown in Table II.

4. Time-Domain Data

While the MAPSTAR radar was built with considerable on-line data processing capability, the data collected in Puerto Rico were recorded as time-domain data (after coherent averaging, but before any Fourier-transform processing). Other time-domain analysis methods (e.g., spaced-antenna-drift) can thus be applied to the same data set. The IDI analysis to be described in Sect. 5 begins with the Fourier transform of the data. Before leaving the time

Table II.   MAPSTAR Operating Parameters.

Feature	As designed	As implemented in Puerto Rico
Frequency	2-5MHz	3.175MHz
PRF	470kHz-1500Hz (1)	100Hz day 25Hz night
Pulse length	30 or 60µsec	30µsec
Transmit power	150kW	200kW
Range-gates	128	40
Range-gate spacing	Variable	3km
Number of points/FFT	Variable (2)	256
System Gain Relative to Boot Lake Prototype	+4dB (3)	+6dB (3)

Notes:
(1) dynamically adjusted to sync to E- or F-region returns for multi-hop reduction. The coherent averaging window is co-adjusted to maintain a constant TDA output rate. This feature was not implemented in the Puerto Rican measurements.
(2) The product of the number of range-gates and the number of FFT points is constrained to be $\leq 2^{16}$.

(3)	Boot Lake	MAPSTAR	MAPSTAR/AIDA
Transmit antenna gain:	19dB	6dB	15dB
Transmitter power:	50kW	150kW	200kW
Receive antennas:	9dB	6dB	6dB
Number of channels:	2	10	10
Maximum PRF:	100Hz	1500Hz	100Hz

domain, let us consider in this section some properties of the time-domain data.

4.1 Data Collection Format. Continuous data were written to 1600 bpi magnetic tape grouped into 819,200-byte files, each being 10 channels x 40 range-gates x 256 tda-pulses x 2 quadrature voltages x 4 bytes/quadrature voltage. The radar was operated at 100 Hz in the daytime, 25Hz at night, and the data coherently averaged down to a time-domain-average (tda) pulse rate of 2.5Hz. (See Sect. 5.2 for an explanation of these choices.) At 2.5 tda-pulses/second, a file spans 102.4sec. Tapes were changed after approximately 48 files (82min). Data were therefore continuous for 82min followed by a 5 to 30min gap for tape change and system adjustments. This pattern was broken about every other tape by tape-write errors that would cause 204.8sec gaps.

There are 10 dipoles, and therefore 10 independent streams of voltage-pairs, being the quadrature (X and Y) components of the measured complex voltage. We label the quadrature voltages according to the dipole's location in the array as

8

$$Q_{ijkqr}(t_n) \qquad (1)$$

where i = direction index (1=E-W; 2=N-S),
　　　j = interferometer element (j=1,2,3),
　　　k = dipole (1=E-W; 2=N-S),
　　　q = quadrature component (1=X; 2=Y),
　　　r = range-gate (r=1,2...40),
　　　n = tda pulse (n=0,1...255),

Since the vertex dipoles serve in both the E-W and N-S lines,

$$Q_{13kqr}(t_n) = Q_{23kqr}(t_n) .$$

$$(2)$$

Then the complex voltages are given by

$$V_{ijkr}(t_n) = Q_{ijk1r}(t_n) + iQ_{ijk2r}(t_n)$$

$$(3)$$

and the time-domain phases by

$$\varphi_{ijkr}(t_n) = \tan^{-1}\left(\frac{Q_{ijk2r}(t_n)}{Q_{ijk1r}(t_n)} \right). \qquad (4)$$

4.2 Data Pre-Processing. Each tape is processed first for dc removal, spike removal, and gain and phase adjustment. The spike removal, in which single-pulse voltages more than 20dB above the running average are removed, is occasioned partly by the need for protection against large noise spikes and partly by the misbehavior of receiver #6, which was noisy but largely restored by this filter. Phases were hardware-adjusted approximately on the ten independent receiver channels. Final phase corrections determined by averaging over several hours of data from a strong E region while assuming that the average return was ordinary mode from the zenith, since, according to Heater facility personnel, the transmitters were phase (but not amplitude) adjusted for right-hand-circular transmission, which approximates ordinary polarization in the northern hemisphere. The phase calibrations, dependent on the behavior of the E region on one afternoon, are a possible source of error.

The time delay to the first range gate was set by the operator to be 6km. This was corrected during off-line analysis for one-half the pulse length of 30μsec (timing in the radar is measured from the trailing edge of the pulse), the time delay in the receiver electronics (21μsec), the time delay in the transmit electronics (10μsec), and the lengths of receiver and transmitter cabling (.24 and .66km, respectively). Error estimates were made for each of these. As a result, the actual offset to the pulse-centered first range gate was 3.1±0.5km. Range-gate spacing was 3km, so the 40th and last range gate was at 120.1±0.5km.

4.3 Time-Domain Examples. As long is there is a single effective target (or less) in each range gate, time-domain interferometry can

9

be used to locate it. We showed with the Boot Lake results that time-domain interferometry was useful for tracking meteor trails to determine mesospheric winds [Turek, 1986] and for tracking isolated gravity waves and TIDs (Traveling Ionospheric Disturbances) directly [Halderman, 1987; Adams et al., 1988a]. In Figs. 3, 4, and 6 we present time-domain data for a single "frame" (a set of 256 pulses on 10 receivers covering 40 range-gates, lasting 102.4sec), selected because it contained an airplane overflight as well as good mesospheric returns.

Fig. 3 shows the power profile for our selected frame. The airplane, not identifiable as such except by reference to other power profiles, is evidenced by larger-than-usual power at a range of 9-12km and its capture as scattering points. A large E region is present at 100km, with weaker layers at 90 and 69km and, possibly, 79km as well. Also shown in this plot is the "recovered power", which is the power calculated in the IDI process as coming from the scattering points, discussed in Sect. 6.2. All logarithmic voltage and voltage-squared (power) values are relative to the voltage digitization unit of the radar. The vertical scale is range (km) for the raw power, and altitude (km) for the recovered power. A single value for raw power at each altitude for the entire frame was calculated as the incoherent sum

$$P_r = \sum_{ijkqn} Q^2_{ijkqr}(t_n).\qquad(5)$$

The $i=2, j=3$ contributions are omitted to avoid counting the vertex dipoles twice.

Figure 3. Raw (—) and recovered (•••) power profiles for one 102.4sec sounding. Recovered power is defined as the power remaining after analysis and noise rejection.

Fig. 4 shows a stack-plot of phase vs time for 40 ranges; the phase is calculated with eqn. (4) from the sum of the complex voltages, which is the mathematical formation of an antenna beam pointed in the zenith. In this figure, phase from each range-gate is plotted separately and, if viewed at a single range (e.g., if the plot is masked except for a thin horizontal strip whose width is the spacing of the tics on the range axis), shows the characteristic wrap-around at ±π of all such phase plots. However, our pulse length is longer than our range-gate spacing (we oversample by 1.5), so that adjacent range-gates usually have similar phase histories. The visual effect is to make the phase appear continuous across range-gate boundaries,
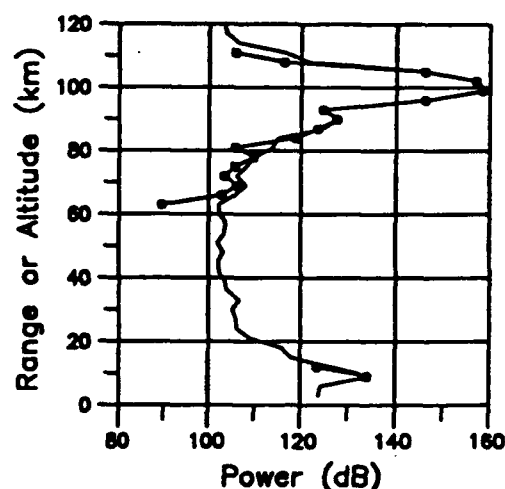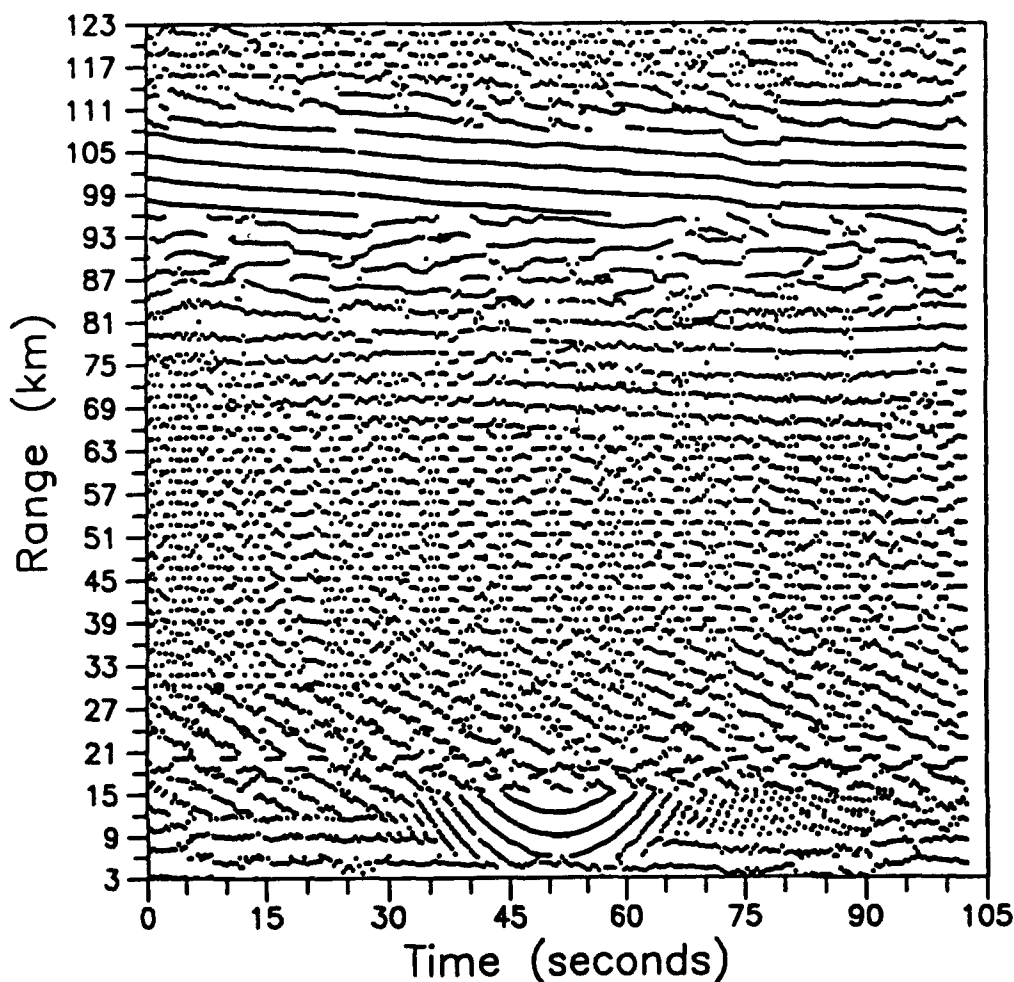
Figure 4. Phase vs time, stacked ranges, for the same 102.4sec sounding used in Fig. 3. Phase at each narrow altitude strip runs from -π to +π. Returns are atmospheric above 66km, interference below. A slowly descending E region is apparent around 110km, with more complex returns in the mesosphere/D region. Interference dominates the region below 66km, with an airplane traverse seen around 10km.

particularly in the E-region returns, and enhance the eye-brain identification of coherent patterns.

The airplane overflight is centered about a range of 9km and a time of 52sec. The nest of parabolas shows the airplane's decreasing phase with approach, passing through its point of closest approach at 52sec, and increasing phase while leaving, characteristic of any approximately linearly traveling target. (The centering of the airplane in the 102.4sec record is no accident; since the data are continuous, we can select the start

11

and stop times of a frame at will.) Both the E region around 100km and the much weaker mesospheric returns from around 65-80km show very stable regions with slowly decreasing phase. The region from 80 to 100km is more confused, suggesting multiple scatterers.

There was considerable interference from an AM radio station a few miles away during the daytime, which can be seen in the range-independent patterns from 10 to 65km, masked at lower altitudes by ground clutter, system-generated voltages and the airplane returns, and at higher altitudes by atmospheric returns. This interference mostly disappears after polarization filtering (Sect. 6.1) and is thus of no real consequence to our analysis. We will return to this data frame in Fig. 6 after a discussion of the IDI analysis procedure.

4.4   Time-Domain Interferometry.

A single target such as the airplane can be located by simple interferometry as indicated in Fig. 5. The phase difference between a pair of antennas along an E-W line is related to the elevation angle of the target by the interferometer equation:

$$\Delta\varphi_{EW} = -\frac{2\pi D}{\lambda}\cos(\theta_{EW}).\qquad(6)$$

where D is the antenna spacing and the cosine term is just the direction cosine, ℓ.   As this is the geometry that we will also use later in the frequency domain, let us pause briefly to establish the relations we will need.   For simplicity, we take the two lines of antennas as lying along the cardinal directions.   (As pointed out in Sect. 3, the array in Puerto Rico was actually rotated 45° from cardinality; an axis rotation was appended to the IDI analysis.)
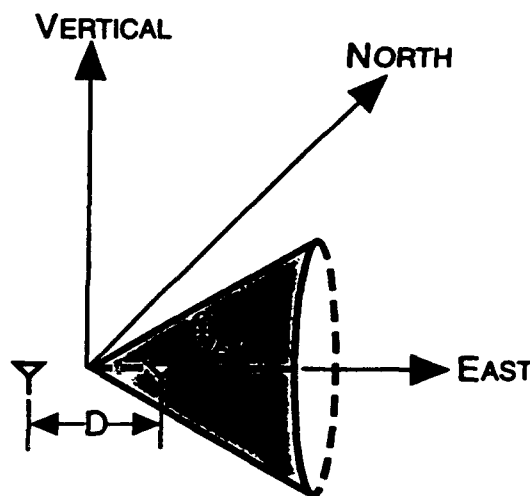
Figure 5. The phase difference for a returning pulse is measured by a pair of antennas with spacing D, which determines the cardinal angle θ_{EW} via eqn. (6).

Note that a measurement of $\Delta\varphi_{EW}$ only localizes the target to the surface of the cone formed by rotating the line-of-sight vector about the E-W axis. A second antenna-pair along the N-S axis, plus range-gating, are required to determine the target's three-dimensional location. Since the direction cosines ℓ,m and the range R are directly measured, the spatial coordinates of the target (X,Y,Z) can be calculated as

$$X = R\cos(\theta_{EW}) = R\ell$$

$$Y = R\cos(\theta_{NS}) = Rm \qquad\qquad (7)$$

$$Z = R\sqrt{1 - \ell^2 - m^2} = Rn$$

where R is the distance from radar to target, and ℓ, m, and n are the X,Y,Z direction cosines to the target. We refer to θ_{EW} and θ_{NS} as the cardinal elevation angles. It is somewhat more intuitive to use their complements, but use of the pair of cardinal zenith angles leads to some confusion since the complement locates, not the target itself, but rather the intersection of the E-W (N-S) cone with the upper half of the X-Z (Y-Z) plane.

The altitude can also be written as

$$Z = R\sin(\beta), \qquad\qquad (8)$$

where β is the zenith angle, measured from the Z axis to the target, whose Pythagorean relations to the cardinal angles and the direction cosines are

$$\sin(\beta) = \sqrt{1 - \cos^2(\theta_{EW}) - \cos^2(\theta_{NS})} = \sqrt{1 - \ell^2 - m^2}. \qquad (9)$$

5. IDI Processing

For the analysis presented here, a frame of data consisted of 256 time-domain-average (tda) pulses for 40 range-gates and 10 antenna-receiver channels; since the data are continuous, they can be regrouped into frames of any start time or length, limited by the tape capacity of 82min. (The length of a frame can be, e.g., lengthened to give maximum velocity resolution without aliasing, shortened to give maximum temporal resolution, or adjusted to match the scattering-point lifetimes.) Each channel's data are separately Fourier-transformed, and the resulting 10 complex Fourier spectra at each range-gate are examined for Doppler bins whose sources can be located by spatial interferometry.

5.1 Justification for the IDI Data Characterization. It is empirically observed that an individual spectral feature measured with a multi-antenna radar is frequently "locatable", which is to say that the antenna-to-antenna phase differences agree on the feature's location in the sky. It is also observed that most of the received power can be so located. This suggests replacing the several complex voltages by a pair of voltages and a pair of phase gradients, the latter corresponding to the horizontal coordinates of the location. This also suggests that the locatable spectral features, which we label "scattering points", might have some physical reality.

In our earlier work with data from the prototype radar, we

13

have shown that the aspect sensitivity of their scattering cross-sections is much like that measured in other experiments [Adams et al., 1989], and that the mean motions of the scattering points have magnitudes and altitude variations similar to winds [Adams et al., 1986], although we occasionally see well-defined wave motions [Halderman, 1987; Adams et al., 1988a,b]. We leave any speculation about the physical processes responsible for the scattering points until we have described the analysis and have examined some of their properties.

5.2 Experiment Design. The MAPSTAR radar can be operated with a raw pulse rate of as high as 1500Hz. In Puerto Rico we used only 100Hz in the daytime and 25Hz at night, the nighttime rate lowered to avoid multi-hop. The raw data stream is coherently integrated on-line down to a time-domain-average (tda) pulse-rate (Ψ) defined by the measurement requirements—2.5Hz in this case.

The transmit antenna at the Arecibo Heater Facility consists of a 4x8 array of vertex-down log-periodic antennas. We used half (4x4) of the array, which has a main lobe in the vertical of $\approx 11°$ beamwidth from zenith to the half-power point, with the first minor lobe at 15°. We designed for returns out to 16° from zenith, and found that useable returns were often present this far from zenith. We designed for a maximum horizontal velocity of 150m/sec, which corresponds to a maximum radial velocity at 16° zenith angle of 41m/sec, which in turn required that Ψ could not be less than the Nyquist limit determined by this radial velocity. Hence

$$\Psi \geq \frac{4 V_R F}{C},\qquad (10)$$

where V_R = maximum radial velocity (m/sec),
$\quad$ F $\;$ = radar frequency = 3.175×10^6 Hz,
$\quad$ and C $\;$ = speed of light = 3×10^8 m/sec.

Eqn. (10) then gives a minimum Ψ of 1.9Hz; because of equipment restrictions, we actually used 2.5Hz, which gave a maximum horizontal speed of 214m/sec and a maximum radial velocity of 59m/sec. Since the daytime (nighttime) PRF was 100 (25) Hz, a 40-(10-) pulse coherent average was performed on-line to reduce the effective PRF to 2.5Hz.

5.3 Spectral Analysis. Since data from each range gate are analyzed separately, the r-subscript is dropped henceforth. We Fourier transform each channel's complex voltage series separately, for which we use a conventional complex FFT:

$$V_{ijk}(\omega_d) = \sum_{n=0}^{255} e^{-i\omega_d t_n} V_{ijk}(t_n).\qquad (11)$$

(Since a complex, or phase-preserving, spectral transformation is required, many popular spectral estimation techniques such as

14

maximum entropy are not applicable to IDI.)

We use end-point averaging, which is to say that we replace both the first and last pairs of quadrature voltages of each 256-pulse sequence with the averages of the two pairs, but no other form of window function.
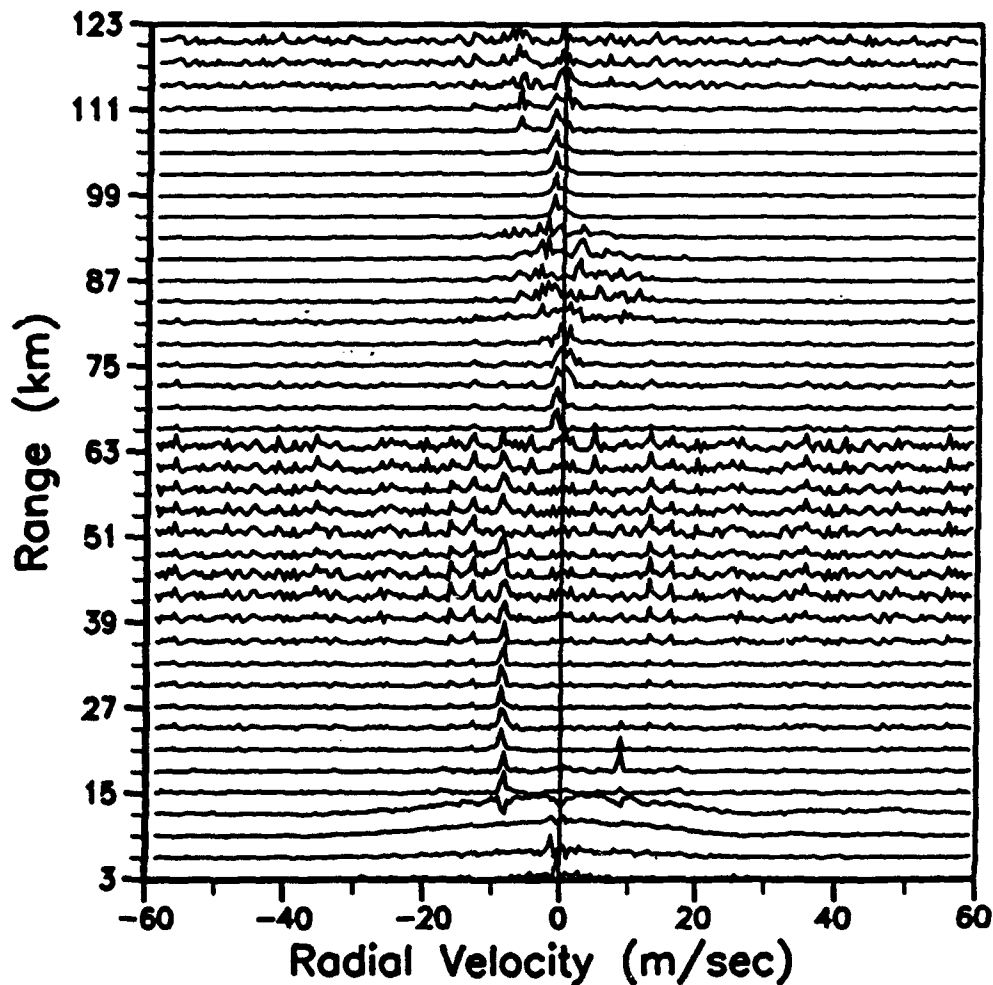

Figure 6. Normalized Fourier voltage amplitude vs radial velocity, stacked ranges, for the same 102.4sec sounding used in Figs. 3 and 4. The very broad spectrum of the airplane's traverse is seen at the lower altitudes; interference is identified up to 66km by the constancy of its spectra with range; atmospheric returns above 66km show range-to-range variability predominately around zero Doppler velocity (i.e., around the zenith).

15

Fig. 6 is the stack-plot of the Fourier-transform voltages for all ranges, again for the 10 complex voltages summed in-phase. The Fourier voltage amplitude at each range is autoscaled, i.e, amplitudes at each range are separately normalized to their maximum. This causes interference to be particularly noticeable in the 42-66km region, where atmospheric returns are weak. The airplane is seen as a very broad peak around zero Doppler, in keeping with the phase history in Fig. 4 that showed the airplane transiting from approach to departure over the period of the frame. The interference is seen as a well-defined pattern that is nearly constant with range. The D- and E-region FFTs are interesting: of the three layers noted earlier, the highest and lowest show fairly narrow negative peaks, in keeping with the simple decreasing phase shown in Fig. 3, while the middle region has a much broader spread in radial velocities, suggesting higher scattering-point speeds and/or more off-zenith contributions to the aspect sensitivity of the scattering.

5.4   Scattering-Point Analysis.   Having Fourier-transformed the voltages, we must determine which of the 256 spectral windows (each representing a separate radial velocity—half positive, half negative) satisfy the IDI requirement of representing "real" (i.e., locatable) targets, since in a real measurement every window will contain some power.   There are 10 independent measurements of complex voltages, and therefore nine independent phase differences available for this calculation.   We treat the average phase difference between the E-W dipoles and the N-S dipoles as an independent variable to be separately measured for the polarization information it contains, leaving eight phase differences (four for each cardinal direction) available to determine the reality of a scattering point and its location.

Determining whether a scattering point exists is logically separate from the process of determining the location of the point, even though, in our approach, both use antenna-to-antenna phase differences.   Each frequency in the complex Doppler (FFT) spectrum represents a potential scattering point.   We first test the 10 complex spectral voltages at each Doppler frequency to see if they collectively define a "real" scattering point; as a second step we determine the best estimate of the point's location.

Each spectral window at each range-gate is examined separately.   Potential points are rejected if any spectral voltage has both quadrature components of absolute value less than 10 radar voltage units for any of the 10 antenna-receivers, since the arctangent of the ratio of two single-digit integers is not accurate enough to be useful.   Points are also rejected if any one of the 10 channels has a spectral power less than some threshold fraction (currently 1×10^{-2}) of the total power in its range-gate. This rejects a large fraction of the possible points.   Without the 10^{-2} threshold, the E region sometimes yields a cluster of

16

scattering points near zenith with a wide distribution of Doppler velocities, through a process which we do not currently understand.

Applying eqn. (6) to the antenna array in Fig. 1, we determine eight estimates of the cardinal angles:

$$\theta_{i,k,s} = \frac{\pi}{2} - \arcsin\left(\frac{-\Delta\varphi_{i,k,s}}{\frac{2\pi D}{\lambda}}\right),$$ (12)

where $\Delta\varphi_{i,k,s} = \varphi_{i,j+1,k} - \varphi_{i,j,k}$

and $s = 1,2 = \theta$-values available for each cardinal direction i and dipole orientation k. We now require agreement among the eight estimates of the two cardinal angles as follows: We calculate the differences in the estimates of the pairs, and the differences in the averages, as

$$\theta_{i,k,2} - \theta_{i,k,1} = \delta\theta_{i,k}$$

$$\frac{(\theta_{i,1,1}+\theta_{i,1,2})}{2} - \frac{(\theta_{i,2,1}+\theta_{i,2,2})}{2} = \Delta\theta_i$$ (13)

and we require that

$$\epsilon_i = \frac{\delta\theta_{i,1} + \delta\theta_{i,2} + \Delta\theta_i}{3} \leq \Delta\theta_{max}$$ (14)

for i = 1 and 2 independently. ϵ_i is thus the average difference between pairs of independent estimates of the cardinal angle for the ith direction, and is constrained to be less than $\Delta\theta_{max}$, which is the single controlling parameter of the IDI analysis (excepting the threshold value discussed above). The value adopted for $\Delta\theta_{max}$ in the results presented here is 20°; this represents the average range in θ within which the four independent estimates for each cardinal direction must lie. Several considerations enter the choice of a value for $\Delta\theta_{max}$. It can be usefully interpreted as a spread in phases; eqn. (6) tells us that, for D=λ/2 spacing, 1° in cardinal angle for a target suitably near the zenith corresponds to 3.14° in phase. We can therefore filter in terms of either the zenith-angle window $\Delta\theta_{max} = 20°$ or the equivalent $\Delta\varphi_{max} \approx 63°$. This relationship between phase and cardinal angle only holds near the zenith; the analysis output thus depends on whether the requirement of eqn. (14) is implemented as a phase window or a cardinal-angle window. For reasons that become obvious upon contemplation of eqn. (6), implementation as a cardinal-angle window results in an additional pass-band filter on the scattering points that is unity near zenith but goes to zero at the horizons, so that is the implementation used here.

We make four independent calculations of each cardinal angle in the process of determining whether the spectral window under consideration is the result of a real scattering point. How can we

17

now do the final calculation of the two cardinal angles so as to maximize the accuracy of the result? The first step seems obvious: we should coherently combine the ten dipole-pairs into five crossed dipoles. The MAPSTAR antenna configuration then presents the interferometer-location problem in its simplest non-trivial form: three collinear antennas along each of two interferometer arms.

Let us first fashion a figure of merit with which to judge various combinatorial schemes. Retrieving the interferometer equation:

$$\Delta\varphi_{EW} = -\frac{2\pi D}{\lambda}\cos(\theta_{EW}),\tag{6}$$

we see that the accuracy of the measurement near the zenith depends linearly on the length of the baseline. Recalling that errors propagate through additive processes as the square root of the sum of their squares, and that errors vary inversely as the number of terms in a coherent average and as the square root of the number of incoherent averages, we can fashion a figure of merit for the cardinal-angle calculation as

$$\gamma = \left(\frac{D}{\lambda}\right)\sqrt{H_a H_b I},\tag{15}$$

where H is the number of coherent averages, a and b denote the two effective antennas whose phase difference is to be used, I is the number of incoherent averages, and D is the antenna spacing. Eqn. (15) reduces to

$$\gamma = \left(\frac{D}{\lambda}\right)H\sqrt{I}\tag{16}$$

when the coherent averages are applied uniformly ($H_a = H_b$).

In Table III we show the results of applying eqn. (15) first to the case of averaging the four individual linear-dipole determinations (as used above in the locational part of the problem), then to three possible ways of combining the crossed dipoles; these differ by whether and how the middle crossed dipole is included. It is aesthetically displeasing to see that the best result, according to our figure of merit, comes from the asymmetric inclusion of the middle antenna. In the data analysis presented below we forsook the 5% advantage and omitted the middle crossed dipole in the final

Table III. Figure-of-Merit Values.

	D/λ	H_a	H_b	I	γ
Individual dipoles: Average of 4 at D=λ/2	0.5	1	1	4	1
Crossed-dipole pairs: (1+2) vs (2+3)	0.5	2.8	2.8	1	1.4
(1+2) vs (3)	0.75	4	2	1	2.1
(1) vs (3)	1.0	2	2	1	2

18

cardinal-angle calculation. (The ambiguities implicit in eqn. (6) due to D>λ/2 are resolved by the approximate determinations of the cardinal angles already accomplished in the reality testing.)

Once the location is adequately determined, we require that the cardinal angles give a non-imaginary altitude when eqn. (7c) is imposed. Imaginary altitudes can result from noise or noisy data, since the two cones determined by the two cardinal angles need not intersect (imagine a point calculated to lie exactly north and exactly east simultaneously).

In the final step of the analysis, two representative complex voltages are calculated and saved as part of the scattering-point parameters—one for each dipole orientation, so that information about the polarization of the return is preserved. The just-determined cardinal angles are introduced as phase shifts on each dipole other than the vertex pair to put the five linear dipoles, on average, in-phase (i.e., the array is mathematically steered toward the scattering point). The individual linear-dipole voltages along each interferometer arm are then coherently summed to give the two scattering-point voltage amplitudes and phases. Steering maximizes the signal/noise for the sum and references both sets of complex voltages to the vertex crossed dipole. This method of mathematically steering the receiving-antenna beam, has been developed and extended as "post-set steering" [Röttger and Ierkic, 1985; Kudeki and Woodman; 1990].

5.5 The Scattering-Point Parameters. The three-dimensional location, together with the Doppler velocity of the scattering point and the amplitudes and phases of the return, comprise the "scattering-point parameters", which are:

Z = Altitude,
V_R = Radial velocity,
Θ_{EW} = E-W cardinal angle,
Θ_{NS} = N-S cardinal angle,
A_{EW} = Voltage amplitude on the E-W-oriented reference dipole,
ϕ_{EW} = Phase of the E-W-oriented reference dipole,
A_{NS} = Voltage amplitude on the N-S-oriented reference dipole,
ϕ_{NS} = Phase of the N-S-oriented reference dipole.

These parameters exist for each identified scattering point, of which there are typically 200-2000 per frame (distributed unevenly over the 40 range-gates). They represent 102.4sec averages, and along with their time of occurrence are saved as the fundamental output of the IDI processing. With each point we also save the actual values of the two cardinal-angle windows ϵ_i, defined by eqn. (14). These can be used for additional filtering and are used for estimating the errors in derived quantities (see Sect. 6.6). Some properties of the scattering points are discussed in the following section.

6. Characteristics of the Scattering Points

Processing of the data as described in Sect.s 4 and 5 has been done for 34½ hours of data, from 0530UT 10 April till 1600UT 11 April, 1989, this period being the closing 1½ days of the second AIDA campaign. In this section we examine the polarization characteristics of the scattering points, and show that selecting the ordinary-mode points eliminates a large fraction of the noise. This filtering is then applied to the scattering points before discussions of the recovered power, the aspect sensitivity, and the mean apparent motions and their spatial structure.

6.1 Polarization Properties. Since ordinary-mode pulses were being transmitted (see Sect. 4.2), we expect that atmospheric scattering will return predominately ordinary-mode signals; the principal interference, coming from a nearby commercial AM radio station, will be linearly polarized. Since the parameters for each scattering point include complex voltages for an orthogonal pair of reference dipoles, we can look at the phase relations for each point separately. Fig. 7a shows the EW vs NS phase of the individual scattering points for one hour of data (1300-1400LMT, 10 April 1989). Two distinct clusters of points are seen: one along the "ordinary" line, and one along the "(+,+) linear" line. Notice that the ordinary line wraps around to the line (-180,90 to -90,180) in the upper-left quadrant, and that the (+,+) linear wraps around to the two clusters of points in the upper left and lower right corners.

Fig. 7b-d shows the distribution of radial velocity vs altitude for these points, separated into ordinary, extraordinary, and linear groups. The modes were defined with ±45° limits, so that every point in Fig. 7a belongs to one of the three groups. The separation of characteristics is remarkable. The ordinary-mode points are clearly from atmospheric returns; their distribution defines the mesosphere and E region nicely. These returns appear as three distinct regions: 60-80km, 80-100km, and 100-120km, which for convenience we will call the mesosphere, mesopause, and E-region returns, respectively. The linear returns are clearly not associated with any atmospheric process, but are rather randomly distributed in altitude and radial velocity. The threshold filter suppresses them above 80km where the O-mode atmospheric returns are strong enough. The AM radio station that is the major source of interference lies to the SW, thus its appearance as (+,+) but not (+,-) linear, is as would be expected. The extraordinary returns are quite sparse, but show an interesting sprinkling of points at low altitudes around -9m/sec, with a weaker image around +9m/sec. This seems to be accompanied by corresponding absences of linear-mode points at the same Doppler velocities. Since the ±9m/sec features are a constant feature in the six days' data we have examined to date, we suspect that they are somehow connected to sea scatter.
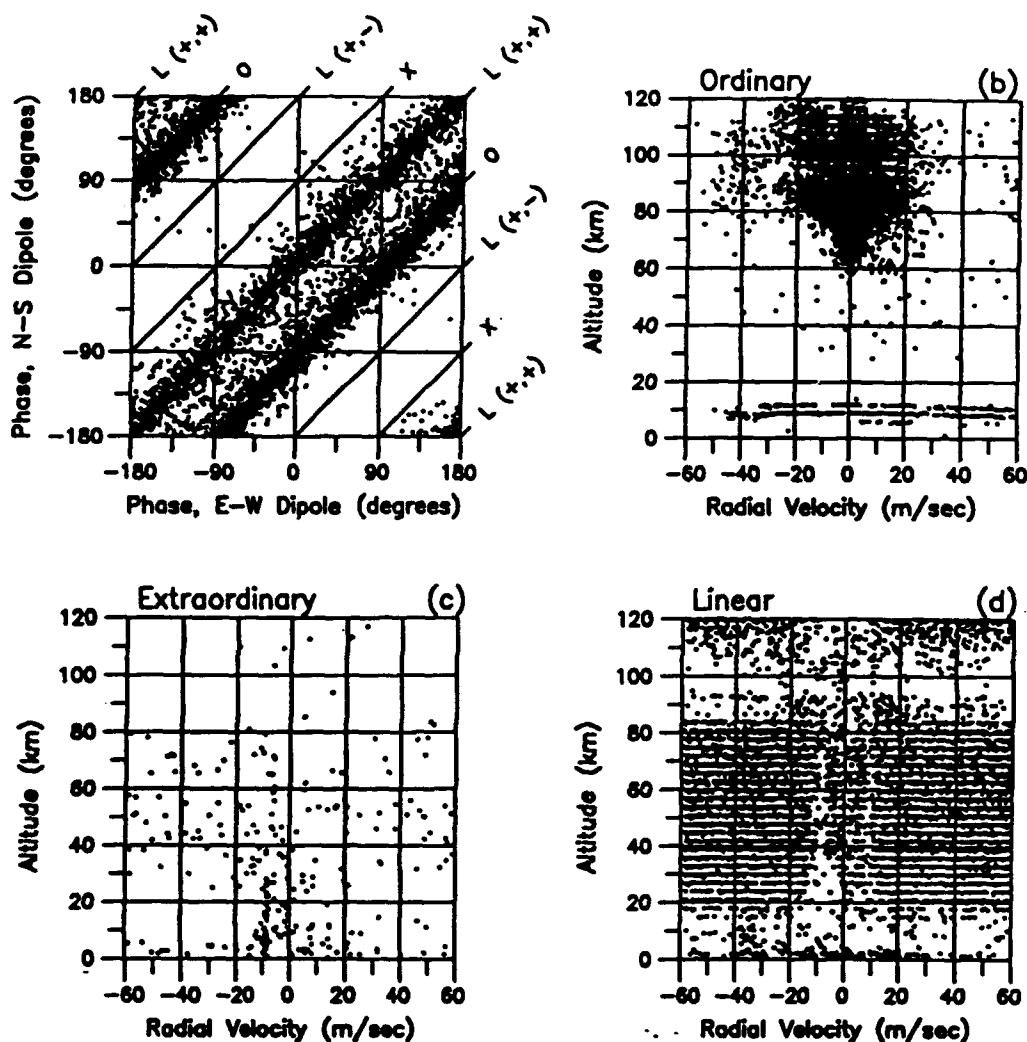
Figure 7. The polarization properties of the scattering points in a 1-hour interval (1300-1400LMT, 10 April 1989).
Fig. 7a shows an EW vs NS phase plot for all the scattering points identified at all altitudes, showing large clusters around the ordinary-mode (O) and (+,+) linear-mode (L) lines.
Figs. 7b-d show radial velocities vs altitude for the three modes: O-mode points (7b), which have a clearly atmospheric distribution (O was the mode transmitted); X-mode points (7c), which are sparse and not obviously related to the atmosphere; and L-mode points (7d), which are plentiful and predominately random.

Filtering to select only the ordinary-mode points is clearly indicated, and shows one of the particular advantages of the scattering-point representation. It allows polarization filters with 100% out-of-mode rejection. This filtering has been applied to the scattering-point parameters discussed in the remainder of this paper.

21

6.2 Recovered Power. The recovered power (by which we mean the power recovered by the scattering-point analysis) vs. altitude was shown in Fig. 3. This power is calculated as

$$P_{sp}(z) = \sum_{j=1}^{J(z)} \sum_{k=1}^{2} A_{j,k}^2 \qquad (17)$$

where $J(z)$ is the total number of scattering points in the 3km altitude (not range) interval at z. Fig. 3 indicates the complete recovery of the power available from the E-region returns, and the recovery of information at levels of 10dB or more below the raw-power level at altitudes below 70km. Notice that no scattering points were identified at some altitudes, and that the appropriate vertical scale is altitude rather than range, since we have determined the three-dimensional spatial location of each point.

Fig. 8 shows recovered power (as color) vs altitude vs time plot for 24 hours of individual (102.4sec) frames of scattering points. The daytime formation and descent of the E region and the sporadic presence of lower-altitude layers are clearly seen. The persistence of mesospheric echoes throughout the night is promising for mesospheric studies; notice also the development of as many as four discrete layers in the morning and late afternoon. The regular gaps are due to tape changes; the streaks of power across altitudes during the night are due to unfiltered bursts of interference (probably European teletype traffic).

6.3 Horizontal Distributions of Scattering Points. Fig. 9 shows horizontal "skymaps" of scattering points in 3km-thick horizontal slices at six altitudes: 60, 70, 80, 90, 100, and 110km. The map is plotted with coordinates of the cardinal zenith angles (degrees E-W vs degrees N-S). Most of the points come well within the 12° zenith angle of the transmit antenna's main lobe; the points outside this circle are illuminated by the weaker side and grating lobes of the transmit array. The zenithal symmetry at 60 and 70km should be contrasted with the distinct asymmetry at 90 and 110km.

6.4 Variation of Power with Zenith Angle. The distribution of power with zenith angle, or aspect sensitivity, has been examined in the mesosphere with both beam-forming [Vincent and Belrose, 1978; Hocking, 1979; Jones, 1980] and interferometric [Adams et al., 1989] medium-frequency radars. The scattering is generally found to be approximately specular at altitudes below 80km, but tending towards isotropic scattering above that. In Fig. 10 we show the average variation of recovered power with zenith angle for our 1hr data sample. These results have not been corrected for

MAPSTAR IDI Radar – AIDA Act '89

Islote, Puerto Rico. Monday, April 10, 1989

Recovered Power (db)

Altitude (km)

125 100 75 50 25 0

02:00 LT 05:00 LT 08:00 LT 11:00 LT 14:00 LT 17:00 LT 20:00 LT 23:00 LT

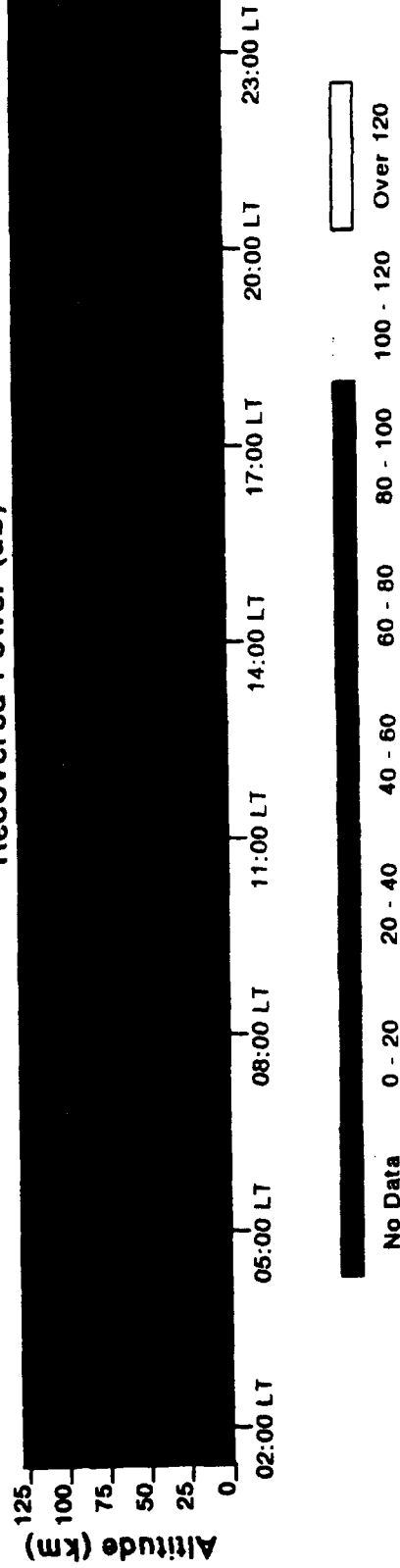No Data   0 - 20   20 - 40   40 - 60   60 - 80   80 - 100   100 - 120   Over 120

Figure 8. The recovered power (color; dB) vs time (abscissa; 1 day) vs altitude (ordinate; 0–120km). Note dynamic behavior of E region, and afternoon striations in the mesosphere. Stripes across ranges are interference.
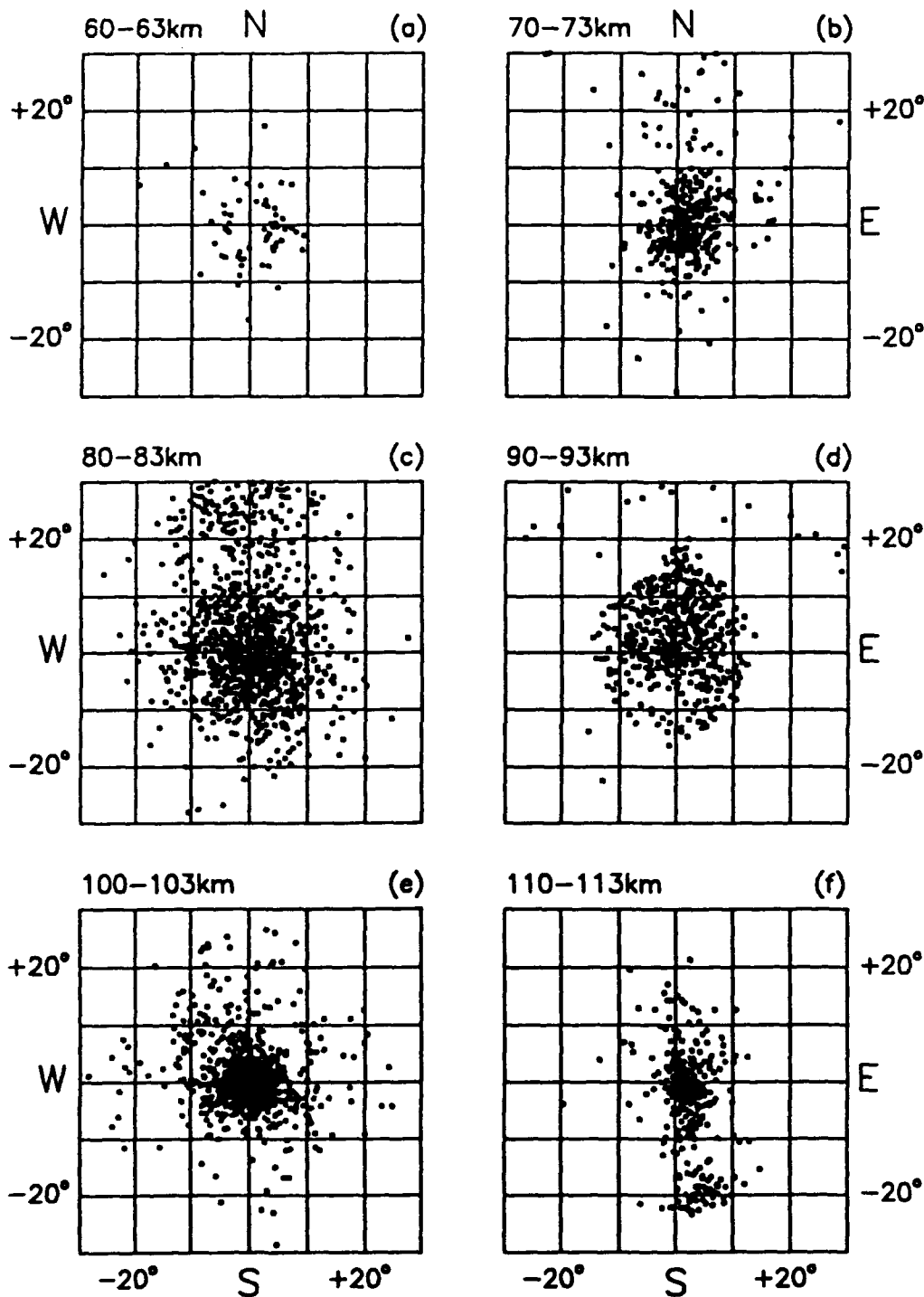
Figure 9. Horizontal maps of scattering-point locations at six altitudes: 60-63km (9a), 70-73km (9b), 80-83km (9c), 90-93km (9d), 100-103km (9e), and 110-113km (9f). Zenith is at the center of each figure; axes are in degrees from zenith. Data are from the same 1-hour interval as in Fig. 7. Note the considerable asymmetry in the distributions at 90 and 110km.

the gain patterns of the transmit and receive antennas; when corrected the curves will be stretched toward larger zenith angles. Fig. 10 shows the zenith angles that contain 25%, 50%, and 75% of the recovered power. The behavior is typical of the profiles that we've looked at to date; it shows half the power being contained within about 5° zenith angle up to 80km, then increasing rapidly above that to a maximum of about 8° at 93km, above which if falls very rapidly to 1-2°. We know from Fig. 9, however, that the asymmetry in the distribution is comparable to these values at some altitudes, and that a more complex description is needed to accurately represent the distribution of recovered power in the sky.
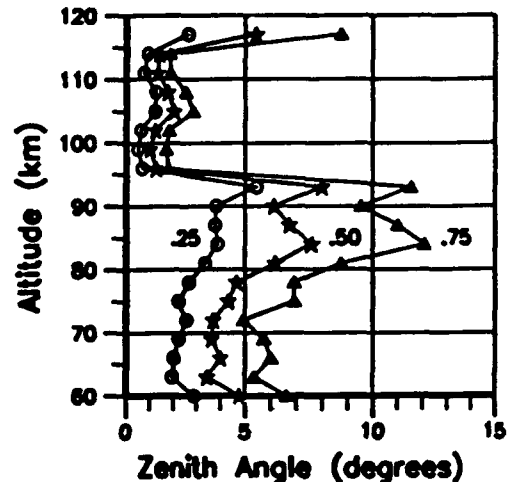
Figure 10. Width of the scattering vs altitude (aspect sensitivity). Lines show the zenith angles that contain 25%, 50%, and 75% of the recovered power.

6.5 Mean Apparent Motions. Now let us examine some of the dynamical characteristics of these points. Fig. 11 shows contour maps of the distribution of radial velocities every 10km (60-110km) for our 1hr accumulation of scattering points (1300-1400LMT, 10 April 1989); these plots match the five plots in Fig. 9. The results at the lower altitudes show just what we should expect for an atmosphere in predominately horizontal motion; the gradient from negative (blue, approaching) to positive (red, receding) Doppler velocities is obvious. Irregularities in that pattern are seen at 90km, and grow larger above that. Each location on the 25x25 contour grid is smoothed by averaging the nearest 40 points, weighted as $r^{-\frac{1}{2}}$.

The calculation of the vector mean apparent motion of the scattering points is a straight-forward least-squares fitting problem [Adams et al.,1986]. We describe the mean apparent motion as

$$\vec{U} = u\vec{1}_x + v\vec{1}_y + w\vec{1}_z \qquad (18)$$

where u,v,w are the eastward (zonal), northward (meridional), and upward components, and the bold 1's are unit vectors along the indicated axes. Scattering points from all frames within the time period of interest are used in ensemble for these calculations. We reject points more than 16° from zenith, points more than 1° from zenith whose horizontally projected speed exceeds 300m/sec, and points that differ from the fitted mean-apparent-motion vector by
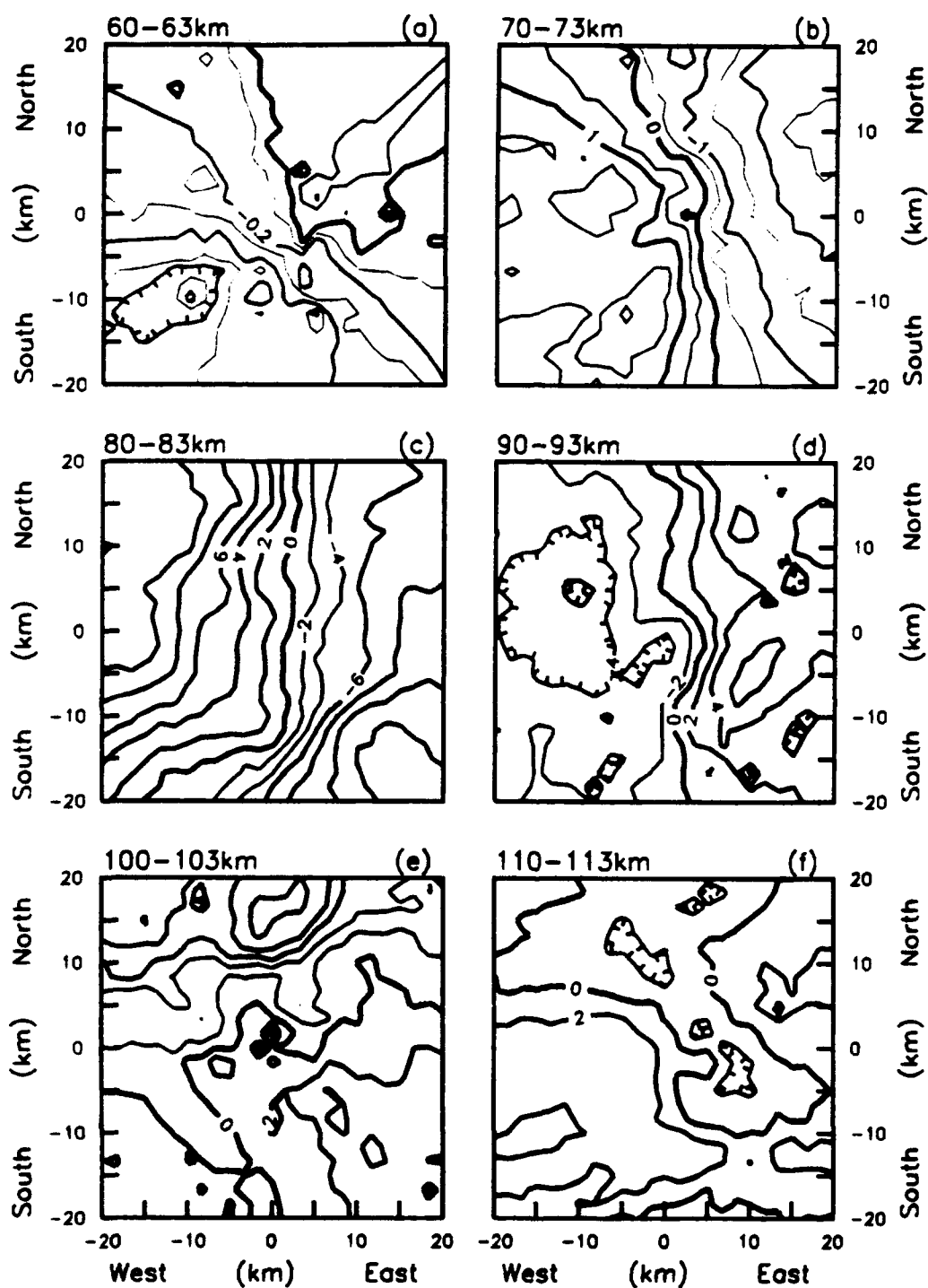
25

Figure 11. Horizontal maps of radial velocities at six altitudes corresponding to Fig. 9. Zenith is at the center; units are km from zenith. Data are from the same 1-hour interval as in Figs. 7, 9, and 10. Dark red: $V_r < -5m/sec$; light red: $-5 < V_r < 0m/sec$; green: $V_r = 0m/sec$; light blue: $0 < V_r < 5m/sec$; dark blue: $5m/sec < V_r$. Contour spacing: a:0.1m/sec; b:0.5m/sec; c-f:2m/sec.

more than 3 standard deviations (the solution is iterated until no more points are rejected). The fit is done in two stages: first all points with zenith angles less than 5° are used for a 3-vector fit, and the vertical velocity w is saved. Next, all points with zenith angles between 3° and 16°, and w from the previous fit, are used to get a two-vector fit to the horizontal components u and v. (This generalizes a method sometimes used for MST radars, in which the vertical beam is used as a measure of the vertical velocity, which is then used with the two off-zenith beams to get the horizontal components.) All the points within a 3km window that meet the criteria are used in the fit; if the number of available points available falls below five for either the vertical or horizontal calculation, no solution is produced. No smoothing in altitude or time is used.

Fig. 12 shows the results of the mean-apparent-motion calculation for a 10min interval near the center of the 1hr accumulation of scattering points used in Figs. 7, 9, 10, and 11. To reduce confusion, only the zonal (positive when east-going) and vertical (positive when upgoing) components are shown. The zonal component shows a strong west-going peak at 81km (-60m/sec) and 105km (-35m/sec), with an eastward peak at 93km (30m/sec). The vertical component (plotted at x10) shows upward maxima of 2m/sec at 93 and 104km, and is otherwise quite small. The determination of the calculational uncertainties is described in the following section.

The uncertainties for this 10min data sample in the zonal component are typically ±10m/sec, and ±1m/sec in the vertical. These will vary as the square root of the length of the data sample, and be considerably larger at night.

Figure 12. Vector motion field, 1-hour average. ΔΔΔ = zonal component, positive when east-going. ●●● = vertical component x 10, positive when up-going.

6.6   Uncertainty Estimates.   The transmitted pulse length was 4.5km at the half-power points, with the output of the four transmitters being, on average, flat-topped over the central half of the pulse. The range-gate spacing was 3km; the range itself has an estimated uncertainty (see Sect. 4.2) of ±0.5km. From this we can estimate the uncertainty in range, and therefore altitude, as ±2.5km. We take the uncertainty in Doppler
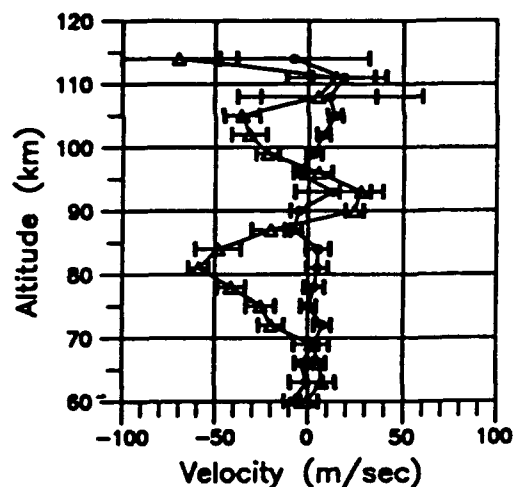
27

velocity as $\pm\frac{1}{2}$ the Doppler-window width, which becomes $\pm.23$m/sec for our operating parameters. The spread of values in the two cardinal angles are determined separately for each scattering point (see Sect. 5.4); these values are saved with each scattering point. To determine the uncertainties in the mean apparent motions, we calculate the motion profiles for all combinations of the measured parameters at their extrema, with the perturbations weighted by

$$W = \frac{1}{\sqrt{N/3}} , \qquad (19)$$

where N is the number of scattering points used and there are three degrees of freedom in the fit. N varies from a minimum allowed value of 5 to a few thousand, depending on the altitude, time of day, and duration of average. This gives 128 profiles, since we use both symmetrical and antisymmetrical combinations of the radial-velocity and zenith-angle extrema. The final values of the motion components, denoted by the lines in Fig. 12, are taken as the centers of the distributions rather than as the output of the unperturbed calculation.

The uncertainties in range and in radial velocity are determined largely by equipment-parameter choices, while the uncertainties in the horizontal coordinates are determined more directly by noise. Noise means, in our case, the existence, after filtering, of two kinds of scattering points: scattering points caused by a collection of purely random voltages that manage to get through the filters, and scattering points whose parameters are only approximately correct due to the presence of non-atmospheric returns. Noise sources include random background noise, interfering signals, internally generated signals, ground clutter, side-lobe echoes, and multi-hop returns. We will consider each briefly:

As described in Sect. 5.4, cardinal angles determined by different antenna pairs are required to agree to within a window of width $\Delta\theta_{max}$, which corresponds to a phase window of $\Delta\varphi_{max}$ as determined by eqn. (6). The probability P that random phases can give such agreement on N independent antenna pairs is given by

$$P = \left(\frac{|\Delta\varphi_{max}|}{\pi} \right)^N . \qquad (20)$$

As we discussed in Sect. 5.4, there are eight independent determinations of phase differences, and therefore four estimates each for the two cardinal angles, since there are 10 independent channels taken as five E-W oriented dipoles and five N-S-oriented dipoles (see Figs. 1 and 2). The remaining information is saved as the absolute phases of the E-W and N-S dipoles at the vertex site. Eqn. (20) thus predicts less than 2 random points per 40-range-gate image when using $\Delta\varphi_{max} = 63°$, as we did here. The use of multiple antennas is seen to geometrically reduce the probability that

28

random noise can be interpreted as a scattering point. Polarization filtering further reduces random points by 65%. Purely random points are therefore predicted to be identified as real scattering points less than one point in 40 range gates in each sounding.

The density of scattering points due to interfering signals can be estimated from Fig. 7a, where a weak overlap of the linear and ordinary populations is small but distinct. These will contribute noise to any calculation that selects the ordinary-mode points but does no further filtering (e.g., the aspect sensitivity in Fig. 10). How many of these get through the additional filters in the motion calculations (the restriction of zenith angles to <16°, the rejection of points with horizontally projected speeds > 300m/sec, and the 3σ "outlier rejection" algorithm), we have not yet determined.

Internally generated signals include the ringing that follows the transmitted pulse. Since this appears as a large repeating pattern at the lowest altitudes, it may be possible to subtract the ringing and use the tropospheric and stratospheric returns.

Ground clutter is generally stationary. Since we remove the dc component of the time-domain signal as part of the data preprocessing, stationary targets are rejected. Any moving target (e.g., automobile, airplane) could possibly be identified as a scattering point, but since there is no ambiguity about the altitude and location of any of the scattering points, no matter where they are in the sky, targets near the horizon are identified as such. We can, for example, identify and track airplane overflights, which we frequently see (at the correct altitudes) out to zenith angles of ≈60°.

Since there is no ambiguity about the locations of any of the scatterers, no side-lobe problems exist. The receiving-antenna spacing is $\lambda/2$, so there are no grating lobes either, except in the final calculation of the cardinal angles when the 1λ spacings are used (see Sect. 5.4). The transmit antenna has many side and grating lobes, so there are regions well off zenith being weakly illuminated. In fact, the first minor lobe is at 15°, which is how those points with zenith angles of 12-16° are being illuminated. These scatterers are located without ambiguity; we also expect to find a number of meteors in these side lobes. Ideally we would illuminate the entire sky; the heater's transmit beam was broadened to its maximum for these measurements, but a wider beam would have been better.

Nighttime multi-hop, caused by the absence of the absorbing D region, has been identified on a few occasions, even at the glacial nighttime pulse rate of 25Hz. It is easily identified by diagonal patterns in radial velocity vs altitude plots of the scattering points. The MAPSTAR radar was built with the capability to

synchronize the pulse rate to the return from a reflecting region, so that the multi-hop echoes would be coincident with the primary returns, leaving the returns from below the reflection point uncontaminated. This feature was not implemented in Puerto Rico; it would have increased our signal/noise considerably, especially at night when it is needed the most.

7. Algorithmic Shortcomings

The imaging Doppler interferometer method is a new way of looking at mesospheric radar returns, but it is important to keep in mind that no new physical processes are involved: the radar returns from the atmosphere are the same that all medium-frequency radars see, although the data are collected in somewhat more thorough fashion and certainly analyzed differently. A number of potential problems and questions concerning the IDI method have been recognized by others and by us; these divide into two categories: those concerned with the IDI analysis as implemented here (which can generally be ameliorated or eliminated by known or suspected improvements), and those concerned with the physical identity of the scattering points and the interpretation of the results, which are, of course, the more interesting problems. We will deal with deficiencies of analysis in this section, and speculate about the physical explanation of the results in Sect. 8.

7.1 Velocity Limits. The operating parameters were set (see Sect. 5.2) for a maximum radial velocity of 59m/sec, which gives a maximum horizontal speed of 214m/sec. That should accommodate most bulk wind motions, but would result in aliasing for many gravity waves, if the effects of these waves are indeed present in the data. The extent to which these waves are detectable by atmospheric radars has been the subject of some considerable discussion. We have analyzed data from the prototype [Adams et al., 1988a, b] in which wave motions are clearly identified around the mesopause and the E region. These involve large single waves during nighttime, which may be relatively rare. However, the evidence that wave motions are directly detectable by medium-frequency radars implies a continuous and significant contribution to radar wind measurements by the saturated spectrum of smaller-amplitude waves thought to be present in this part of the atmosphere. Acoustic wave detection is also a distinct possibility at these wavelengths, since acoustic waves with wavelength matching the half-wavelength of the radar (a la the RASS technique) can propagate from near the ground, where there are many natural sources, to 100km with little attenuation. The comparison of IDI mean apparent motions with winds measured by the Arecibo 430MHz incoherent-scatter radar [Hines et al., this issue] shows that medium-frequency scattering is affected both by winds and, above 85km, by waves as well. We could resolve some of these questions by increasing the radial-velocity limit to ≈1000m/sec.

30

7.2 Excess Scatterers. If there are enough scatterers that two or more will occupy the same Doppler window, then there is a potential problem. Whether this is a substantive problem depends partly on the information that is desired. If the scatterers really do exist as isolated and relatively small (compared to the diameter of the cone of observation) scattering regions, then two such regions existing in the same Doppler window will be interpreted as a single scatterer, with its location aliased to the amplitude-weighted mean of the two locations. The apparent scatterer would still lie in the proper Doppler window, so that the motion calculation will be unaffected. Even so, the locations should tend to cluster along the line of motion, distorting the image; so far we have seen no indication of such an effect, although the high density of points around the zenith probably masks such effects. The extent to which multiple scatterers are present in a single Doppler window can be estimated by looking at the constancy of voltage amplitudes along a line of antennas; multiple scatterers cause an interference pattern across the antenna array, and can be rejected if they do. We expect to implement this test soon.

7.3 Spectral-Analysis Algorithms. A conventional complex FFT software routine was used for the spectral transforms. The associated experimental parameters (256 pulses in 102.4sec) were chosen partly from our experience with the Boot Lake IDI prototype, and partly for convenience. Undoubtedly we could make better use of the capabilities at hand: the Doppler-window width can be adjusted by increasing the frame length or zero-filling, for instance, and there may be better phase-preserving transform algorithms than the FFT available. If we knew more about the characteristics of the individual scatterers, particularly their lifetimes and their amplitude and frequency histories (see following section), we could tailor a spectral-analysis algorithm that would be more accurate and would yield more information.

7.4 Spectral Smearing. The Doppler velocity of a target being advected horizontally isn't constant over the averaging time required by the FFT, but rather varies linearly, often across several Doppler windows, as the point's perspective from the radar changes. For a scatterer traveling horizontally not too far from zenith, the time required to traverse a Doppler window is

$$\tau = \frac{\lambda Z}{4 \pi U^2 T},$$ (21)

where τ = time measured from zenith crossing,
λ = radar wavelength,
Z = altitude,
U = speed,
and T = length of data stream.

At 85km, τ=2.5-62sec for U=50-10m/sec, so in a 102.4sec frame, a scatterer will certainly appear in several Doppler windows *if* it

31

lasts long enough. This effect can be removed iteratively [Adams et al., 1988b] by linearly changing the phases of the time-domain data in time in accord with the calculated mean apparent motion— another potential improvement not implemented here. We had anticipated, and Meek and Manson [1987b] have suggested, that uncorrected spectral smearing would be a significant problem. It appears now that this is not so; we have tracked several airplanes passing overhead, and find that the phase differences are preserved by the FFT even when the Doppler velocity changes rapidly. The result is a string of scattering points from a single target, mapping the target's motion. (We were able to track the airplane in Figs. 4 and 6 across 60° of zenith angle.) In casual observation, we have seen no indication of such tracking behavior in the atmospheric returns, but no focused search has been made.

7.5   Scatterer Lifetimes.   The lifetimes of turbulent eddies generated by gravity waves in the mesosphere are of the order of a minute [Hines, 1977]; the lifetimes of stratifications appear to be significantly longer, and recent work [Röttger, 1987] suggests that the occurrence of turbulent layers is often not related to gravity wave breaking at all. Meek and Manson [1987a,b] tried to track individual scatterers from one 72sec frame to the next, with only a few successes. If there are scatterers with lifetimes less than the FFT period of 102.4sec, then the apparent Doppler frequency should be broadened and the returned energy distributed across multiple Doppler windows, decreasing the probability of any of them being identified as scattering points. Since any lifetime broadening would affect the spectrum symmetrically it would be unlikely to have first-order impact on the velocity calculation, but it might cause a false multiplicity of points.

This section and the preceding one taken together seem to say that, for the experiment parameters chosen here, virtually all the scatterers should come through the analysis process as multiple scatterers, yet we see no obvious indication that this is true. It may be that the locational analysis is sufficiently noisy that multiple points are present but not obvious, in which case the points would actually represent a much smaller number of actual scatterers. This may be so; we lack adequate evidence to know.

7.6   The Lack of Use of Amplitude Information.   The relative amplitudes and phases on the crossed dipoles can be used to determine the electron-density profile from the birefringent properties of the mesosphere, but except for filtering low-amplitude points, the amplitudes are not used in the IDI processing described here; the identity and location of the scattering points, and the resultant motions, derive entirely from the phase information. The amplitudes are shown directly, of course, in Figs. 3 and 8 and used in the aspect-sensitivity profile in Fig. 10, and were mentioned in Sect. 7.2 as a possible way to identify and reject multiple scatterers. Also, the method clearly selects for the largest-amplitude scatterers, these being the ones whose

32

phase will be sufficiently well defined that they can be recovered as scattering points.

7.7   Motion-Fitting Schemes.   Once the scattering points are identified, the question of how best to fit a mean-apparent-motion vector arises. We have used both unweighted and spatially gridded radial velocities as input to the least-squares fitting of the motion vector; unweighted results were presented here. Spatial gridding may be preferable, as it reduces the domination by numbers of the points clustered around zenith. Meek and Manson [1987a] tried both unweighted and weighted fitting schemes, and discarded points with zenith angles >5°. When we use all the points in a three-dimensional motion-vector fitting scheme, as described in Adams et al. [1985, 1986], there are two undesirable effects: a noticeable tendency for the magnitude of the motion to decrease with increasing zenith-angle limit, and a corresponding tendency for the vertical-motion profiles to become more erratic. When we implemented the MST-like scheme of using near-zenith points (0-5°) to get the vertical velocity, and the vertical velocity plus more off-zenith points (3-16°) to get the horizontal velocity (see Sect. 6.5), both effects were ameliorated.

It may be that the velocity distributions are bimodal, or worse, caused by, for example, separate wind and wave motions. We make no tests for multimodality, and would currently not be aware of such distributions if they existed.

8.   Discussion and Conclusions

The MAPSTAR IDI radar performed well in its first measurement campaign. We have described this radar as it was designed and as it was implemented in Puerto Rico, where we used the Heater Facility's amplifiers and transmit array. We have discussed the IDI technique and the scattering-point characterization. In this section we will follow a consideration of the IDI results with a brief speculation about the physical identity of the scattering points.

8.1   The IDI Technique.   Interferometry is clearly a useful improvement over beam-forming radars for studying the mesosphere, since antenna beams adequately narrow to resolve multiple scatterers are impractical at medium frequencies. Now that hardware is available, interferometric methods can be expected to replace beam-forming approaches in many applications.

The ideas of Doppler sorting and spatial interferometry are not new, but in IDI have been combined and extended to provide a three-dimensional Doppler image of the illuminated volume, which allows us to identify and locate multiple scatterers within individual range-gates. The IDI analysis characterizes interferometric data with a compact and accessible description of

the scattering region. It remains to be seen whether this description elucidates the as-yet-unknown physical processes causing the scattering better than other descriptions, but the results presented here show some distinct advantages and insights that are unique to the IDI approach.

With an ideal data-processing algorithm, one would specify a mathematical description of all measured variables based on a physical model of the important scattering processes, and the free parameters of the model would be simultaneously fitted to the data. We have done the inverse by letting the form of the data dictate the model: since the variation of Fourier phase with distance is so often linear, we keep the data that are accurately represented by such variations and discard the rest.

We break the fitting process into several steps (Fourier transform, scattering-point reality, and scattering-point location), making a number of assumptions in the process (constant Doppler velocity over the averaging period, only one scatterer within any Doppler window, etc.). At best, each step only approximates its role in a fully developed model. A considerable improvement can be made by following the concept developed in radio astronomy with the CLEAN algorithm [Högbom, 1974], in which the effects of the strongest scattering point would be removed from the time-domain data and the IDI analysis repeated until no more significant power could be removed. We plan to implement this soon.

We have done a simple implementation of the IDI analysis, arguing that the algorithmic shortcomings can be improved in a number of ways (spectral analysis tailored to the problem, multiple scatterers identified, etc.) once the simple results are understood. Even so, the results demonstrate four distinct advantages of the method: 1) It retrieves three-dimensional Doppler images with a time-domain signal/noise of -10dB or better, a benefit ("Fellgett's advantage") that accrues to Fourier-transform methods. 2) It allows polarization filtering with extremely good separation of circular from linear modes. 3) It generates a description of the three-dimensional spatial structure of the scattering amplitudes and peculiar velocities. 4) It results in high-resolution radars with minimal antenna arrays whose portability and flexibility, even at 100m wavelengths, make their use in campaigns like AIDA practical.

The ability to polarization-filter (Sect. 6.1) is an example of a manipulation not possible in other data characterizations. Separation of linear- from ordinary-mode returns in the time domain is particularly difficult, since any linear return can be decomposed into half ordinary and half extraordinary components, while any ordinary return can similarly be expressed as two orthogonal linears. The separation possible once the polarizations of the individual scattering points are known is nearly exact;

34

there is very little overlap between the two populations in Fig. 7a. This is promising for the determination of the electron-density variation with altitude by transmitting ordinary and extraordinary pulses alternately. The clustering of the atmospheric-return scattering points along the ordinary line in Fig. 7a is to be expected, since ordinary-mode returns were assumed in the phase calibration (see Sect. 4.2). The clustering of the interference along the linear line is strong evidence that the atmospheric returns are indeed circular. (We can't resolve from this evidence whether the transmitted signals and the atmospheric returns are ordinary or extraordinary.)

Sky-scanning observations with Doppler-beam radars have shown a 20-30dB range of returned power. By selecting the brightest scatterers in the sky, IDI gains ≈20dB advantage over Doppler-beam radars, which are obliged to use whatever scatterers happen to lie in their beams. This advantage is balanced in practice by the decreased illumination intensity that accompanies wider transmit antenna beams; the net result is an atmospheric radar with very modest antenna arrays whose capabilities are nonetheless comparable to much larger systems.

Describing radar scattering in terms of a number of scattering points gives us a new way to look at an old problem, for there is nothing different about the mesosphere we study from the mesosphere studied by Gardner and Pawsey [1953], and nothing different about the returns we study from the ones they studied. Certainly we have collected a more detailed set of data than they were able to—we should not forget that much of what we know about the radar-scattering mesosphere was determined by Gardner and Pawsey with a dozen or so photographs of an oscilloscope screen. But the IDI characterization is fundamentally different. The description is quantized, and thus lends itself to manipulations not possible with continuous-function descriptions.

The quantized data description has other advantages, as suggested by the skymaps in Fig. 9 and the Doppler-velocity maps in Fig. 11. Spatial structures with scales of 1-40km in the occurrence patterns of the scatterers, in their amplitudes, and in their Doppler velocities can be studied with descriptions like these. A full three-dimensional analysis of spatial structures and their temporal evolution can be determined from the data in this form.

The validation and location process described here is considerably different from that used for the IDI prototype at Boot Lake, Colorado [Adams et al., 1985, 1986]; we offer our current understanding of our past analysis by way of explanation for the change. The Boot Lake prototype IDI radar had five equally spaced antennas in each cardinal direction. The identifications of the scattering points, as well as their locations, were determined by least-squares fitting straight lines to the two sets of phases at

35

each Doppler frequency. The rms errors of the two fits determined whether the point was real, and the slopes gave the two cardinal angles. Further analysis demonstrates that this is not a very satisfactory method for either detecting real scatterers or locating them; a least-squares fit of a straight line to a set of collinear phase measurements weights the phases by their distance from the center; with an odd number of antennas, the center one contributes not at all. The approach used here, in which N independent measurements yield N-1 independent differences among which agreement is required, is far preferable. Combinations that use each measurement the same number of times are optimal. Here we have used the four terminal dipoles once, and the six interior dipoles twice, when determining the acceptability of the scattering points. The four terminal dipoles and two vertex dipoles are used again in the final locations of the points—not ideal, but an improvement over using a least-squares fit as we did with the prototype.

A side benefit of the IDI approach is the compression effected on the time-domain data; the data volume was reduced here by a factor of 28, which when implemented as a real-time process in the radar's computers will allow us to expand from 40 to 128 range-gates while decreasing our tape usage to about two tapes per day, or about one 4mm DAT tape every two weeks.

8.2 The Physical Mechanisms Responsible for Radar Scattering. If we did a three-dimensional analysis of spatial structures, what would it be the structure of? What are the physical processes responsible for the existence of these scattering points and for their behavior? Part of the answer is in the results presented here; other parts are in the motion vs winds comparison [Hines et al., this issue] and in the tidal-mode study of these data [Roper et al., this issue]; certainly a large part of the answer remains unknown.

It has often been argued that medium-frequency radars measure winds directly [e.g., Meek and Manson, 1985; Reid, 1988]. We have shown [Adams et al., 1988a,b] that medium-frequency radars can occasionally detect and track gravity waves and TIDs in the 85-110km region. Hines et al. [this issue] show that motions at medium frequency track the incoherent-scatter radar (ISR) measurements accurately below 80km, but that frequently the measurements diverge above that altitude, with the medium-frequency radar apparently responding to a combination of the wind and to effects associated with the critical-layer dissipation of gravity waves. Roper et al. [this issue, 1991] shows that the tidal modes, deduced from the scattering-point description using the Groves [1959] analysis method (treating the scattering points as if they were meteors), give good tidal information over the full 70-110km region. Since the ISR results are known to be unusable above 95km, the reasons for the frequent disagreement between IDI and ISR in the 80-95km region remain unknown.

How are we to interpret these results? Two possible models suggest themselves: first, as suggested by Hines et al., is that scattering surfaces become so distorted by critical-layer dissipation of gravity waves that off-zenith glints develop, and that above 80km the radar returns are determined by the effects of wave motions on the glints; in the second model scattering is from turbulent eddies, seen from their instant of creation caused by breaking waves, and with velocities determined initially by the wave parameters, but then changing speed until they are fully entrained by the wind.

If their lifetimes were comparable to or longer than the frame rate of the IDI radar ($\approx$100sec), glints would make an adequate model for the results presented here; if their lifetimes were much shorter, they would approximate delta functions, their transforms would be distributed across the spectrum of radial velocities, and no identification of them as scattering points would be made. The IDI method would thus be selective for glints with longer lifetimes.

Turbulent eddies, and more generally any perturbations of the local refractivity with spatial scales of $\lambda/2$, are also a plausible explanation for the scattering points. Their lifetimes are predicted to be [e.g., Hines, 1977] of the order of the IDI frame rate used here. If they are indeed created with a velocity different from the local wind, then slow down or speed up until their velocities match the wind, then they would form an adequate model.

Meteors must also play some role in scattering at these altitudes. Individual large meteors are easily identified and analyzed separately in the IDI data [Turek, 1986; Thomas, 1989]. At medium frequencies the trails often last 30-60 seconds, much longer than VHF returns (<1 second), and comparable to the 102.4sec frame length we used here. We plan to examine the data to locate large individual meteors, and determine whether and how they appear in the scattering-point description, and how their mean motions compare with those determined from the scattering points. This is only possible with meteors that are large enough to be identified as such, but the number flux of meteors is much larger at smaller sizes, so there should be a significant population of small meteor trails throughout the mesosphere and lower thermosphere. These are likely to be some of our scattering points. However, it is unlikely that meteors are a very significant fraction: Meteors appear preferentially at large zenith angles, while the scattering points appear preferentially around zenith, and meteor trails occur with a strong diurnal variation maximizing at dawn and with a minimum at dusk, while the scattering points have strong local-noon maxima.

Whatever the physical mechanisms responsible for the radar scattering from the mesosphere, it is clear that Doppler

interferometer radars give us a powerful new tool for their study.

9. Acknowledgements

10. References

Adams, G.W., J.W. Brosnahan, and D.P. Edwards, The imaging Doppler interferometer: Data analysis, Radio Sci. 20(6), 1481-1492, 1985.

Adams, G.W., J.W. Brosnahan, and T.D. Halderman, Direct radar observations of TIDs in the D- and E-regions, J. Atmos. Terrest. Phys. 50(10/11), 931-935, 1988a.

Adams, G.W., A.W. Peterson, J.W. Brosnahan, and J.W. Neuschaefer, Radar and optical observations of mesospheric wave activity during the lunar eclipse of 6 July 1982, J. Atmos. Terrest. Phys.50(1), 11-20, 1988b.

Adams, G.W., J.W. Brosnahan, and R.E. Johnson, Aspect sensitivity of 2.66-Mhz radar returns from the mesosphere, Radio Sci. 24(2), 127-132, 1989.

Adams, G.W., J.W. Brosnahan, D.C. Walden, and S.F. Nerney, Mesospheric observations using a 2.66 Mhz radar as an imaging Doppler interferometer: Description and first results, J. Geophys. Res. 91(A2), 1671-1683, 1986.

Adams, G.W., M.A. Ghafourian, and J.W. Brosnahan, Turbulence and wave spectra in the mesosphere, to be presented at the Spring AGU, Baltimore, 1990.

Adams, G.W., A.W. Peterson, J.W. Brosnahan, and J.W. Neuschaefer, Radar and optical observations of mesospheric wave activity during the lunar eclipse of 6 July 1982, J. Atmos. Terrest. Phys. 50(1), 11-20, 1988b.

Austin, G.L., R.G.T. Bennett, and M.R. Thorpe, The phase of waves

partially reflected from the lower ionosphere (70-120 km), J. Atmos. Terrest. Phys. 31, 1099-1106, 1969.

Austin, G.L., and A.G. Manson, On the nature of the irregularities that produce partial reflections of radio waves from the lower ionosphere (70-100 km), Radio Sci. 4(1), 35-40, 1969.

Beer, Tom, D-region parameters from the extraordinary component of partial reflections, Ann. Geophys. 28, 341-347, 1972.

Belrose, J.S., and M.J. Burke, Study of the lower ionosphere using partial reflection, 1. Experimental technique and method of analysis, J. Geophys. Res. 69(13), 2799-2818, 1964.

Breit, G., and M.A. Tuve, A test of the existence of the conducting layer, Phys. Rev. 28, 554-575, 1926.

Briggs, B.G., Radar observations of atmospheric winds and turbulence: a comparison of techniques, J. Atmos. Terrest. Phys. 42, 823-833, 1980.

Brosnahan, J.W., and G.W. Adams, Imaging-radar measurements of middle-atmosphere winds, presented at the XIX General Assembly of the International Union of Geodesy and Geophysics, Vancouver, British Columbia, Canada, August 9-22, 1987.

Cohen, D.J., and A.J. Ferraro, Modeling the D-region partial reflection experiment, Radio Sci. 8, 459-465, 1973.

Dalaudier, F., M. Crochet, and C. Sidi, Direct comparison between in situ and radar measurements of temperature fluctuation spectra: A puzzling result, Radio Sci. 24(3), 311-324, 1989.

Devlin, J.C., P.L. Dyson, and P.R. Hammer, A pulse synthesis technique for improving ionosonde resolution, Radio Sci. 12(5), 767-772, 1977.

Dewan, E.M., and R.E. Good, Saturation and the "Universal" spectrum for Vertical Profiles of Horizontal Scalar Winds in the Atmosphere, J. Geophys. Res., 91, D2, 2742, 1986.

Farley, D.T., H.M. Ierkic, and B.G. Fejer, Radar interferometry: A new technique for studying plasma turbulence in the ionosphere, J. Geophys. Res. 86(A3), 1467-1472, 1981.

Fisher, David E., A Race on the Edge of Time, McGraw-Hill, New York, 1988.

Flood, W.A., Revised theory for partial reflection D-region measurements, J. Geophys. Res. 73(17), 5585-5598, 1968.

From, W.R., J. MacGibbon, and J.D. Whitehead, A strange result in

the measurement of the angles of arrival of the first and second echoes from the ionosphere at high radio frequencies, J. Atmos. Terrest. Phys. 51(3), 223-231, 1989.

Gage, K.S., B.B. Balsley, and R. Garello, Comparisons of horizontal and vertical velocity spectra in the mesosphere, stratosphere and troposphere: observations and theory, Geophys. Res. Lett. 13(11), 1125-1128, 1986.

Gardner, F.F., and J.L. Pawsey, Study of the ionospheric D-region using partial reflections, J. Atmos. Terrest. Phys. 3, 321-344, 1953.

Gordon, W.E., and J.A. Dobelman, Comparison of measured and calculated antenna patterns for the Islote heater, Rice University Report, 13 July 1982.

Gregory, J.B., Radio wave reflections from the mesosphere, J. Geophys. Res. 66, 429-445, 1961.

Gregory, J.B., and A.G. Manson, Seasonal variations of electron densities below 100 km at mid-latitude I. Differential absorption measurements, J. Atmos. Terrest. Phys. 31, 683-701, 1969.

Groves, G.V., A theory for determining upper atmosphere winds from radio observations on meteor trails, J. Atmos. Terrest. Phys. 16, 344-356, 1959.

Halderman, T.D., An analysis of apparent-motion vectors in and the structure of a mid-latitude sporadic E layer using a 2.66 Mhz radar, (Master's thesis), CASS Rpt. GR-08, Utah State University, Logan, 84322-4405, 1987.

Hammer, P.R., and I.A. Bourne, A high resolution ionosonde--1. Technique and analysis methods, J. Atmos. Terrest. Phys. 38, 935-943, 1976a.

Hammer, P.R., and I.A. Bourne, A high resolution ionosonde--2. Equipment and preliminary results, J. Atmos. Terrest. Phys. 38, 945-956, 1976b.

Harper, R.M., and R.F. Woodman, Preliminary multiheight radar observations of waves and winds in the mesosphere over Jicamarca, J. Atmos. Terrest. Phys. 39, 959-963, 1977.

Hines, C.O., Internal atmospheric gravity waves at ionospheric heights, Can. J. Phys. 38, 1441-1481, 1960.

Hines, C.O., Relaxational dissipation in atmospheric waves—II. Application to Earth's upper atmosphere, Planet. Space Sci. 25, 1061-1074, 1977.

Hines, C.O., G.W. Adams, J.W. Brosnahan, F.T. Djuth, M.P. Sulzer, C.A. Tepley, and J.S. Van Baelen, Mesospheric wind and partial-reflection observations: Comparisons and interpretations, submitted to the AIDA Special Issue, J. Atmos. Terrest. Phys., 1992.

Hocking, W.K., Angular and temporal characteristics of partial reflections from the D-region of the ionosphere, J. Geophys. Res. 84(A3), 845-851, 1979.

Högbom, J.A., Aperture synthesis with a non-regular distribution of interferometer baselines, Astron. Astrophys. Suppl. 15, 417-426, 1974.

Ierkic, H.M., and J. Röttger, Mesospheric me surements of irregularity patches using a 3 antenna interferometer, Proceedings, Second Workshop on Technical Aspects of MST Radar, Urbana, Illinois, 21-25 May, 1984.

Jones, K.L., Angular variation of partial reflections from the D-region using a steerable beam radar, J. Atmos. Terrest. Phys. 42, 569-575, 1980.

Jones, R.M., G.W. Adams, and D.C. Walden, Preliminary partial reflection measurements at Brighton, Colorado on 9 January 1981, NOAA Tech. Memo ERL SEL-80, 1982.

Jones, R.M., and R.N. Grubb, D-Region partial reflection Doppler measurements with the NOAA/MPE digital HF radar, Max-Planck Institut fur Aeronomie Rpt. No. MPAE-W-02-80-20, Sept. 1980.

Kudeki, E., B.G. Fejer, D.T. Farley, and H.M. Ierkic, Interferometer studies of equatorial F region irregularities and drifts, Geophys. Res. Lett. 8(4), 377-380, 1981.

Kudeki, E., and G.R. Stitt, Frequency domain interferometry: A high resolution radar technique for studies of atmospheric turbulence, Geophys. Res. Lett. 14(3), 198-201, 1987.

Kudeki, E., and R. Woodman, A post-statistic steering technique for MST radar applications, Radio Sci., in press, 1990.

Lindner, B.C., The nature of D-region scattering of vertical incidence radio waves I. Generalized statistical theory of diversity effects between spaced receiving antennas, Aust. J. Phys. 28, 163-170, 1975a.

Lindner, B.C., The nature of D-region scattering of vertical incidence radio waves II. Experimental observations using spaced antenna reception, Aust. J. Phys. 28, 171-184, 1975b.

Loewenstein, E.V., The history and current status of Fourier transform spectroscopy, Applied Optics 5(5), 845-854, 1966.

Manson, A.G., J.B. Gregory, and D.G. Stephenson, Winds and wave motions (70-100 km) as measured by a partial reflection radiowave system, J. Atmos. Terrest. Phys. 35, 2055-2067, 1973.

Manson, A.G., M.W.J. Merry, and R.A. Vincent, Relationship between the partial reflection of radio waves from the lower ionosphere and irregularities as measured by rocket probes, Radio Sci.4(10), 955-958, 1969.

Mathews, J.D., J.G. Shapiro, and B.S. Tanenbaum, Evidence for distributed scattering in D region partial-reflection processes, J. Geophys. Res. 78(34), 8266-8275, 1973.

Meek, C.E., An efficient method for analysing ionospheric drifts data, J. Atmos. Terrest. Phys. 42, 835-839, 1980.

Meek, C.E., and A.H. Manson, Combination of primrose Lake (54°N, 110°W) ROCOB winds (20-60km) and Saskatoon (52°N, 107°W) M.F. radar winds (60-110km): 1978-1983, J. Atmos. Terrest. Phys. 47(5), 477-487, 1985.

Meek, C.E., and A.H. Manson, Mesospheric motions observed by simultaneous medium-frequency interferometer and spaced antenna experiments, J. Geophys. Res. 92(D5), 5627-5639, 1987a.

Meek, C.E., and A.H. Manson, Medium frequency interferometry at Saskatoon, Canada, Physica Scripta 35, 917-921, 1987b.

Mertz, Lawrence, Transformations in Optics, John Wiley and Sons, 1965.

Michelson, A.A., Measurement by Light-Waves, American J. Sci. 39(230), 115-121, 1890b.

Michelson, A.A., On the application of interference methods to astronomical measurements, Phil. Mag. Series 5, 30(182), 1-21, 1890a.

Michelson, A.A., On the application of interference methods to astronomical measurements, Astrophys. J. LI(5), 257-262, 1920.

Michelson, A.A., and F.G. Pease, Measurement of the diameter of α Orionis with the interferometer, Astrophys. J. 53, 249-259, 1921.

Newman, D.B., Jr., and A.J. Ferraro, Sensitivity study of the partial reflection experiment, J. Geophys. Res. 78, 774-777, 1973.

Pfister, W., The wave-like nature of inhomogeneities in the E-region, J. Atmos. Terrest. Phys. 33, 999-1025, 1971.

Piggott, W.R., and E.V. Thrane, The effect of irregularities in collision frequency on the amplitude of weak partial reflections,

J. Atmos. Terrest. Phys. 28, 311-314, 1966.

Providakes, J.F., W.E. Swartz, D.T. Farley, and B.G. Fejer, First VHF auroral radar interferometer observations, Geophys. Res. Lett. 10(5), 401-404, 1983.

Rastogi, P.K., and O. Holt, On detecting reflections in presence of scattering from amplitude statistics with application to D region partial reflections, radio Sci. 16(6), 1431-1443, 1981.

Reid, I.M., MF Doppler and spaced antenna radar measurements of upper middle atmosphere winds, J. Atmos. Terrest. Phys. 50(2), 117-134, 1988.

Roper, R.G., G.W. Adams, and J.W. Brosnahan, Tidal winds at mesopause altitudes over Arecibo (18N,67W), April 5-11, 1989 (AIDA '89), submitted to the AIDA Special Issue, J. Atmos. Terrest. Phys., 1992.

Röttger, J., The relation of gravity waves and turbulence in the mesosphere, Adv. Space Res. 7(10), 10345-10348, 1987.

Röttger, J., and H.M. Ierkic, Postset beam steering and interferometer applications of VHF radars to study winds, waves, and turbulence in the lower and middle atmosphere, Radio Sci. 20(6), 1461-1480, 1985.

Schlegel, K., A. Brekke, and A. Haug, Some characteristics of the quiet polar D-region and mesosphere obtained with the partial reflection method, J. Atmos. Terrest. Phys. 40, 205-213, 1978.

Schlegel, K., E.V. Thrane, and A. Brekke, Partial reflection results in the auroral D-region explained in terms of acoustic waves, J. Atmos. Terrest. Phys. 42, 809-814, 1980.

Tanenbaum, B.S., J. H. Shapiro, and J.E. Reed, Phase-difference distributions in a D-region partial reflection experiment, Radio Sci. 8, 437-448, 1973.

Thomas, D.R., Meteor observations using the 50 Mhz MENTOR imaging Doppler interferometer, (Master's thesis), CASS Rpt. GR-09, Utah State University, Logan, 84322-4405, 1989.

Thompson, A.R., J.M. Moran, and G.W. Swenson, Jr., Interferometry and Synthesis in Radio Astronomy, John Wiley and Sons, New York, 1986.

Turek, R.S., An analysis of upper atmospheric parameters derived from the observation of meteor echoes by a 2.66 Mhz radar, (Master's thesis), CASS Rpt. GR-06, Utah State University, Logan, 84322-4405, 1986.

Von Biel, H.A., Amplitude distributions of D-region partial
reflections, J. Geophys. Res. 76, 8365-8367, 1971.

Vincent, R.A., and J.S. Belrose, The angular distribution of radio
waves partially reflected from the lower ionosphere, J. Atmos.
Terrest. Phys. 40, 35-47, 1978.

APPENDIX B

"Tidal Winds at Mesopause Altitudes Over Arecibo(18N,67W),
April 5 - 11, 1989 (AIDA'89)"

by

R.G. Roper, G.W. Adams and J.W. Brosnahan

TIDAL WINDS AT MESOPAUSE ALTITUDES OVER ARECIBO (18º N,67º W), APRIL 5 - 11, 1989 (AIDA'89)

by

R.G. Roper (1), G.W. Adams (2) and J.W. Brosnahan (3)

(1) School of Earth and Atmospheric Sciences,
   Georgia Institute of Technology,
   Atlanta, Georgia, 30332-0340
(2) Utah State University,
   Logan, Utah, 84322-4405
(3) La Salle Research Corporation,
   24115 Weld Co. Rd. 40,
   La Salle, Colorado, 80645-9522

ABSTRACT   An imaging Doppler interferometer (IDI) radar was operated during the three AIDA '89 campaigns in Puerto Rico over the period March through May of 1989. The output of the IDI analysis characterizes radar scattering in terms of a number of discrete "scattering points," also referred to as "multiple scattering centers," IDI/MSC for short. For each of these points the three-dimensional location, radial velocity, and amplitude and phase are determined, similar to the output of meteor radars. We have applied the conventional Groves' [1959] meteor wind radar analysis to the scattering points to produce the mean apparent motions over the height range from 70 to 110km which are presented here. The mean apparent motion of the scattering centers is the quantity that would correspond to the neutral atmosphere wind or bulk motion if the scattering points are physical entities (such as turbulent eddies) whose motions are determined solely by advection. This is the quantity which is treated as the "wind" in the analysis which follows, and which should be compared to the wind measurements as deduced from the other methods employed during this campaign. There is, however, a caveat which supports the contention of Hines et al [1992] that extreme care must be used in interpreting the velocities measured by partial reflection radars as winds. The current application of the Groves method of analysis has revealed motions from which one would infer a typical equatorial easterly circulation, with mean meridional circulation becoming significant only above 96km. A periodogram analysis of the complete data interval (April 5 - April 11) has shown the diurnal tide to be the most significant feature of the wind field at these altitudes, with zonal amplitudes up to some 50m/s and meridional amplitudes approximately half this value. The 12 and 6 hour tides become as significant as the diurnal above 100km. The two-day (48+-5hr) wave is the next most significant feature, with zonal amplitude increasing with height up to 30m/s at 110km. The semidiurnal

tide is not at all well developed below 100km. However, analysis on a day by day basis reveals a significant semidiurnal component which is not phase coherent over the total interval. Mean vertical velocities are of the order of tens of centimeters per second, and are considered to be more realistic than the meters per second velocities usually inferred from analyses of meteor trail drifts.

INTRODUCTION. The AIDA '89 measurement campaign in Puerto Rico was designed to explore the relationships among several radar methods for mesospheric wind measurement, and to combine radar and optical measurements to study wave propagation in the middle atmosphere. The imaging Doppler interferometer (IDI) radar method [Adams et al., 1985, 1986] is one of several interferometric techniques currently being explored by the atmospheric radar community. During the AIDA campaign we operated the Arecibo Heating Facility as a pulsed Doppler radar transmitting at 3.175MHz, with 10 independent receiving antennas and receivers. The details and some first results are described by Brosnahan and Adams [1992]. In the IDI approach, we first Fourier transform each antenna's data stream separately, and ask (via spatial interferometry, which is to say by the antenna-to-antenna spectral phase differences) from what unique direction in the sky, if any, each element of the Doppler spectrum originates. If the several antenna pairs agree on the location, the spectral element, or "scattering point", is considered to have been located and validated. Using two orthogonal lines of antennas plus range-gating thus gives us the three-dimensional location of each spectral element. For each "frame" of data (102.4 seconds of data coherently averaged to 256 pulses at each range gate and antenna), a number of scattering points are determined, each characterized by its three-dimensional location, its radial velocity, and its amplitudes and phases. This characterization is what would be obtained, for instance, from an ST/MST radar with multiple beams (each beam corresponding to one scattering point), or by a meteor radar, since a scattering point could represent a meteor echo as well as a clear-air-turbulence or mesospheric stratification return. About 6 weeks' data were taken, with the time-domain data being recorded directly to tape. Six days' data (from April 5 - April 11, 1989) have been reduced for the results presented here. We have applied the conventional Groves' [1959] meteor wind radar analysis to the scattering points to produce the mean apparent motions over the height range from 70 to 110km. The mean apparent motion of the scattering centers is the quantity that would correspond to the neutral atmosphere wind or bulk motion if the scattering points are physical entities (such as turbulent eddies) whose motions are determined solely by advection. This is the quantity which is treated as the "wind" in the analysis

which follows, and which should be compared to the wind measurements from other methods (Hines et al., [1992]).

Figure 1 shows the number of scattering points per sounding per range gate for the six day period. A two day variation in the number of points is obvious, with days 1, 3 and 5 having more scattering points than the even numbered days. As will be shown later, there is a significant two day wave present in the wind results. Another feature of interest is the weak relative minimum occurring around noon in the neighborhood of 96km, which may possibly be related to the minimum in metallic ions evident in Figure 2 (from Mathews et al. [1992]); the descending layers of metallic ions evident in Figure 2 correspond to the compressional node in the zonal shear regime of the diurnal tide (see Figure 3) - in keeping with the wind shear theory of sporadic E (Whitehead [1989]). The shear at 96km at noon acts to disperse any metallic ions present.

.PREVAILING AND TIDAL WINDS.

Tidal winds for the period April 5 - 11, 1989, have been deduced from the IDI scattering point data by using the analysis developed by Groves [1959], which has for many years been used by the meteor wind radar community. Application of the technique to the IDI data revealed one significant difference - a scattering point "rate" some ten times greater than that of meteors was needed in order to stabilize the inversion and produce consistent results with acceptable errors. This is our first clue that individual scattering points may not measure the same motion as a meteor trail; fortunately, the number of scattering point returns per hour from the IDI radar is some one hundred times greater than the usual meteor radar echo rate, making application of the Groves analysis possible.

In addition to a Fourier series fit to the data in time, usually determining the mean, 24 hour (diurnal) and 12 hour (semidiurnal) tides, the Groves' analysis allows polynomial variations in height of the mean or prevailing wind (the constant component of the Fourier fit) and the Fourier component amplitudes and phases. In previous studies, cubic fits describing the variation with height of the zonal and meridional components, with the vertical components being considered constant with height, have been experimentally determined to provide the best fits to meteor radar data over the height range from 80 to 100km. Since the IDI produces useful returns over twice the height range of the typical meteor radar, a higher order fit is appropriate; a fifth order variation has been fitted to the horizontal components of the IDI data over the range 70 to 110km, but with the added dimension of cubic fits with height to the vertical components, thus allowing for the representation of possible convergence/divergence in the vertical motion. Because of the large amount of data collected by the IDI system, to conserve computer time (all computations were performed on a

Macintosh IIcx) only those echoes falling between 5 and 10 degrees of zenith were processed. The effect of the influence of possible specularity in the scattering process is discussed later, and is not found to unduly affect the mean wind plus tidal extraction.

The first IDI radar data set reduced is from the second AIDA'89 campaign, for the interval from 1351UT on April 5 through 1530UT on April 11, 1989. Note that all of the wind results presented here refer to local mean solar time (LMST - UT - 4 hours 28 minutes), since tides are LMST phenomena. Following conventional wisdom regarding tidal extraction, the data set has first been analysed in toto, to provide an average measure of the mean wind and tidal amplitudes over the six day interval. The results are summarized in Table 1, and are presented in contour plot form in Figure 3a-c. The positive contours of the zonal plot denote eastward winds (westerlies); negative contours westward winds (easterlies). Similarly, meridional winds are northward (southerly) if positive, and southward (northerly) if negative. A positive vertical wind is directed upwards. The zonal mean wind is easterly throughout the height range from 70 to 110km; the meridional mean wind achieves significant amplitude only at 94km and above. The diurnal tide is well established, with zonal amplitude larger than meridional (Table 1), and well behaved phase (Figure 4), with the meridional leading the zonal by 7 hours at 74km, 8 hours at 90km and 6 hours at 100km i.e. in quadrature at the highest altitude, and with only small departures from quadrature below. Note the dashed lines (the short is the zonal and the long the meridional) which plot the phases of the S_1^I mode for equinox at 15° latitude (from Lindzen and Chapman, 1969). The Lindzen and Chapman model predicts a vertical wavelength of 28km. A least squares fit to the measured data yields a vertical wavelength of 29(+-3)km.

The semidiurnal tide is somewhat less developed than the diurnal, with the meridional component achieving significance only above 96km, where the phase progression of both components is in quadrature. These results from the Groves analysis (which assumes that each scattering point line of sight velocity is that of the wind), together with the further analyses which follow, would appear to require no other interpretation but that, at least on a diurnal timescale, mean (prevailing) winds and tides are measured by the IDI over the altitude range from 70 to 110km. Note, however, that alternative interpretations are possible - see, for example, Hines et al [1992], and that we ourselves have discovered a caveat to this interpretation..

Groves' analysis performs a three dimensional fit to the line of sight drift vectors and thus has the potential for determining vertical winds. This potential has not, in fact, been very satisfactorily realized in applications to meteor radar data, resulting in typical mean vertical winds of the order of meters per second, which are impossible to justify thermodynamically. The present application of the technique to the IDI radar data, however, results

in mean vertical winds of order tens of centimeters per second, quite comparable with those measured by MST radars (see, for example, Wang and Fritts [1990]). In fact, the downward motion of some 0.3 m/s observed by Wang and Fritts is also observed (quite fortuitously!) during this interval over Arecibo at 94km, but is balanced by upward motion below 90km. (see Table 1). Neither the significance of this convergence nor the behaviour of the vertical tidal motions has been investigated further at this stage..

While one has confidence that the mean (prevailing) winds and tides are the major contributors to the wind energy spectrum in the neighborhood of the mesopause (at least at discrete frequencies), it is also true that analysis of a noise spectrum will provide values of amplitude and phase at discrete frequencies. A periodogram analysis based on the Groves' procedure was used to determine the spectrum of the measured wind. The six days of data were analysed for the amplitudes and phases of frequencies ranging from 0.2 cycles per day (a 5 day period) to 4.5 cpd (a 5.33 hour period) in steps of 0.1 cpd, fitting, as before, fifth order variations with height to the zonal and meridional components and a cubic to the vertical. The result is the three dimensional surface plot of Figure 5, where wind energy is plotted as the sum of the squares of the zonal, meridional and vertical wind amplitudes. The dominant feature of this equatorial spectrum is the diurnal tide at 1.0 cpd, (as previously noted by Mathews [1976] and others) which undergoes significant variation with height, as detailed in Figure 6. The height structure of the diurnal tide had previously been thought to be due to the presence of a standing wave - most unlikely when one examines Figure 4, which shows no sign of the expected 180° phase changes at the amplitude minima which would accompany a standing wave - or possibly to indicate a breakdown and dissipation of the tide at certain altitudes. The behaviour can be explained in terms of day to day variations, as described in the next section. Figure 6 also shows the height variation of the energy in the 12 hour (as significant as the 24 hour above 100km), 8 hour and 6 hour periods. These latter two components are quite insignificant in comparison to the 24 hour component below 98km, but rapidly achieve significance above, with the 6 hour component having as much energy as the 12 and 24 hour components at 110km. The next most significant feature is the 0.5 cpd two day wave, which, while present at all heights, increases significantly with height.

DAY BY DAY ANALYSIS   After performing a tidal analysis of the complete six day period, a day by day analysis was attempted, commencing at noon LMST on April 5 and proceeding in 24 hour increments through noon on April 11, with the idea that such results might be useful in defining the background wind appropriate to measurements of airglow winds. We use these results in the next section to demonstrate the self consistency of the

IDI hour by hour winds (i.e. "instantaneous" profiles produced by averaging one to two hours of IDI data), which have been found to significantly differ from the simultaneous short term measurements by the 430 Mhz Arecibo incoherent scatter radar (ISR), as detailed in Hines et al [1992].

The results of the day by day analysis are presented in the montages of Figures 7a through 7c. Note that each noon to noon contour representation results from the completely independent IDI data set gathered during each of these twentyfour hour intervals. The discontinuities at noon on each day are minimal, contributing some substantiality to the validity of this approach. Note that even with the relatively simple model fitted by the Groves analysis, complex variations of the total wind field in both height (with gradients up to 25 m/s/km) and time (with, for example, zonal changes up to 20 m/s/hr at a given height) are forthcoming.

The most obvious feature of the day by day plots of the zonal wind as presented in Figure 7a is the fact that, in contrast to the other days, the period from noon on April 7 to 1700hrs on April 8 the wind has no westerly component, with the exception of two small cells around 1900hrs on April 7 at 75 and 105km altitude. This is in contrast to the pattern of westerly cells associated with the strong diurnal tide observed on all of the other days, maximizing at increasingly higher altitudes from 88km on April 5 to 100km on April 10 and 11. On April 5 and 6, this maximum occurs around dusk, while on April 9, 10 and 11 it occurs in mid morning. This is almost solely due to the diurnal tide - the phase plot of Figure 4 predicts a westerly maximum at 1800hrs when the maximum is at 86km, and at 0800hrs when the maximum is at 100km. This day by day variation also explains the waxing and waning of the diurnal wind energy with height, previously referred to when discussing the energy spectrum in the last section. What is apparent from Figure 7a is that the diurnal tide, propagating from below, maximizes at different altitudes in the lower thermosphere as time progresses. A breakdown of the diurnal tide as it traverses the equatorial mesopause was first proposed in an application by Lindzen [1968] of classical tidal theory. It is the variation in this day by day dissipation that leads to the unusual height profile of the diurnal tidal energy in the spectrum averaged over the full six day interval.

The apparently anomalous behaviour of the zonal wind on April 7 and 8 does not appear in the meridional wind (Figure 7b), although the overall behaviour of the meridional circulation during the campaign period is by no means simple; note, again, the dominant diurnal tide.

The vertical winds of Figure 7c are presented simply as a matter of interest - we have so far given only minor consideration to their significance, other than to note that their mean magnitudes over most of the height range are of the order of tens of centimeters per second, with tidal components less than a few meters per second in amplitude. One should note that the

51

apparent enhancement of the vertical velocities at the upper and lower height boundaries may simply be an artifact resulting from decreasing data rates and the tendency for increased error in the Groves fit as it approaches the height extremes. This limitation applies to the horizontal components also.

SELF CONSISTENCY OF THE IDI DATA. The lack of agreement between the ISR and IDI winds in Hines et al [1992] renders questionable the apparent magnitudes of the mean circulation and both of the tides over Arecibo during the April AIDA campaign as deduced above since, if the IDI is measuring waves rather than winds above 80km, then the inferred behaviour is questionable. However, if the winds derived above are real, then they should define the background wind contribution to the short term measurements made during these same IDI/ISR comparisons of Hines et al.

To test the consistency of the IDI hour by hour and Groves analyses, the hour by hour winds determined from the Groves coefficients (referred to as IDIG winds) as presented above are linearly interpolated to the midpoint times of the thirteen IDI/ISR profile determinations. The comparisons are presented in the zonal and meridional planes, as Figures 8a - n inclusive. The upshot of these comparisons is that, far more often than not, the IDIG winds provide a mean to the IDI profiles, with agreement often better above than below 80km. This is, of course, fortuitous, since the IDIG winds represent only the background winds, and cannot hope in any way to represent the winds and shears associated with the gravity wave portion of the total wind field as measured by the IDI in any given hourly interval. However, at times or in propagation directions when or where the inferred short period wave component is small (e.g. in the meridional components below 100km of Figures 8c; 8e; 8g; 8l; 8m; and 8n, where the peak deviations are less than 15m/s, and less than 8m/s on occasion, and the zonal component of Figure 8f), the agreement is remarkable. The wavelike character of most of the residuals would appear to provide evidence of the presence of internal gravity waves. The fact that the comparisons sometimes show large deviations at the upper and lower altitudes is probably related to the diurnal variability of scatterers above 100 and below 75km - the Groves fitting technique is weighted to minimize errors where the data is most abundant.

The deviations of the IDI hour by hour winds from the background have been summed for all heights in each of the zonal and meridional directions. The results are summarized in Figures 9a and b. The zonal deviations have a mean of -2m/s with standard deviation 24m/s, while the meridional deviations have a mean of -1m/s with standard deviation 17m/s.

Also plotted in Figures 8a-n are the zonal and meridional components of the winds derived from the incoherent scatter radar data from

measurements made in both the line of sight over the IDI facility and for some 7 1/2 minutes centered roughly 13 minutes before the start or after the end of the basic measurement intervals in a direction orthogonal to the IDI/ISR line of sight (as detailed by Hines et al [1992]). As will be discussed later in reference to a further test of the self consistency of the IDI data, one should note that there may be agreement between one or other of the zonal or meridional components of the IDI and ISR measurements even when there is considerable disparity between the line of sight vectors, and, conversely, discrepancies can exist in the zonal and meridional components when the line of sight measurements are in good agreement.

The significance of the self consistency of the IDI/MSC analyses needs to be emphasized. The "hour by hour" IDI/MSC analysis averages the data appropriate to 10 to 30 of the profiles measured every 102.4s, each hourly profile consisting of the three velocity components determined independently from the line of sight vectors of the total number of scattering points in each 3km height interval - thus each averaged profile is fixed in time, with the velocity at each height showing only a slight dependence on the velocities at immediately adjacent heights (the transmitted pulse length is 4.5km). The Groves analysis, in contrast, models from the data a time series consisting of *only* a constant component (the prevailing wind) and diurnal and semidiurnal components, constrained to follow up to a fifth order variation with height. This height variation was chosen, not necessarily to provide a best fit to the measured height profiles, but rather as a consequence of the experience of one of us (RGR) with radio meteor data, which had been found, on the average, to provide a best fit over the 80 to 100km meteor region if cubic polynomials were employed. Bearing in mind the considerable increase in computer time involved in processing the much larger IDI/MSC data set, it was decided that fifth order fits to the 70 to 110km height range would be adequate. Such a fit allows for vertical "wavelengths" as short as some 24km, which is of the order of that of the S_1^1 tide, expected to be the shortest wavelength tidal mode of any consequence at equatorial latitudes. One consequence of this modeling approach is that all data points are correlated - the first scattering point at the highest altitude is related to the last scattering point at the lowest altitude. Thus the Groves procedure places quite severe constraints on the outcome of the analysis. The best any profile derived from the Groves analysis at a given time can hope to do is to provide the background wind (defined as the prevailing plus diurnal and semidiurnal components) at that time. The self consistency evident in the results presented here, together with the day by day repeatability, and the apparently minimal effect of specular reflection detailed in the next section, could be used to argue for the IDI/MSC technique measuring winds, at least on a diurnal timescale.

ECHO SPECULARITY ON A DIURNAL TIMESCALE.   In order to test the effect
that specular reflection from refractive index discontinuities associated with
waves (which would move with the phase speed of the wave and not trace
bulk motion) would have on the measurement of the mean wind plus tides,
the Groves analysis was applied to the scattering point parameter data for
four different ranges of zenith angle - 0 to 5, 5 to 10, 10 to 15 and 15 to 20
degrees, for the interval from April 5 to April 11. The results are presented
as a montage in Figures 10a through c. Note that these montages are plotted
using the same technique employed in Figure 7 - the contours are fitted to
the 21 heights by 96 hours (the four 24 hour segments) as a single plot; thus
the match between each of the four is an indication of the consistency of the
analysis. Differences of a few meters per second can result in what appear to
be major changes in the contour levels - for example, at midday at 85km in
the 10 to 15 degree meridional data set of Figure 10b, a 20m/s contour has
disappeared, contingent on the peak velocity having decreased from 23 to
18m/s. The changes in the midday easterly maximum at 80km in the zonal
winds of Figure 10a is more serious - while the -40m/s contour is preserved,
the maximum decreases from 82m/s to 58m/s between the 0 to 5 and the
10 to 15 degree data sets. However, we would expect the effects of
specularity to be most evident close to the zenith, since half of the returned
signal power comes from scatterers within 5 degrees of the zenith (see
Brosnahan and Adams,1992). Note, again, that the wind results reported
here use only scatterers occurring between 5 and 10 degrees from zenith.
Even though some differences occur in the magnitudes of the measured
velocities between the four data sets, the overall characteristics, particularly
the dominance of the diurnal tide, are preserved.

ISR/IDI COMPARISONS   The results presented above demonstrate the self
consistency of the quite different analyses (hour by hour and tidal) applied
to the data and the apparent lack of specularity in the scattering process on
a diurnal timescale. They also appear to support the results of Stubbs
(1973), Franke et al (1990) and others that partial reflection wind radars
measure prevailing and tidal winds over the 70 to 110km height range. If,
in fact, all of the comparisons of the ISR and IDI data were as shown in
Figure 11a (0936hrs, April 10, Interval 20, from Hines et al [1992], with the
Groves horizontal projection of the ISR line of sight direction superimposed),
no further comments would be necessary. However, several of the
comparisons disagree to the extent shown in Figure 11b (as for Figure 11a,
but for the comparison at 1124hrs, April 6 (Interval 4, of Hines et al
[1992])), with the IDI and ISR results differing by as much as 80m/s at
89km. One should note that such differences occur only at those times and
altitudes when and where large transient wind velocities and shears are

present - that is, at times of substantial gravity wave activity. This can be confirmed by examination of the high shear regions of Figures 8a-n.

If one considers only the evidence presented so far, one can only guess at the reason for the apparent failure of the IDI short term profiles to agree with the ISR winds, while the same system appears capable of apparently supplying detailed information on the background wind. If the discrepancy in the short term really is due to random waves, then these could disappear in the long term average. The difference between the IDI and ISR sampling volumes may introduce greater variability into the IDI winds, particularly at high shear altitudes. Again, at high shear altitudes the 4.5 kilometer IDI pulse could wash out a shear that would still appear in the ISR data with its 600m pulse - the method of averaging then becomes crucial to the comparison. There are differences in the time domain sampling - the ISR method of averaging the velocity spectra can bias the time of measurement toward a specific interval within the averaging time, and this interval of time is range gate dependent, while the higher signal to noise of the IDI makes that system much less prone to such bias.

AZIMUTHAL SYMMETRY.   A further test has been applied to the IDI data which appears, however, to demonstrate that there is considerable merit in the caution expressed by Hines et al [1992] in the interpretation of partial reflection radar velocity measurements as winds. As already mentioned, the Groves analysis had as its origin a need to model winds as deduced from meteor radar data. Most meteor radars use two orthogonal beam antennae in order to measure both the zonal and meridional wind components. Since the IDI system records data from all azimuths, incorporation of a simple algorithm into the Groves analysis easily facilitates the choice of such a configuration - in our case, two orthogonal beams with +- 45° beam width and elevation angle 80° to 85° (zenith angle 5° to 10° - totally unsuitable for a meteor radar, but commensurate with the previous IDI data reductions). These beams were "deployed" in four different directions for four "runs" - run "A," with the bisector of the two beams the eastward axis; run "B," the southward; run "C," the westward and run "D," the northward (Figure 12). The results are presented in Figure 13. The disparities in both meridional and zonal contours are obvious - while the contour shapes are similar (one should remember that changes in velocity of only a few meters per second can cause what appear to be significant changes in the contour lines), we see differences of as much as 40m/s at several times and altitudes. What this test demonstrates is that, even on a six day timescale, the magnitude of any given wind component depends on the azimuthal direction in which the radar is looking! One might invoke the postulate of Hines et al [1992] that the IDI radar velocities do suffer interference from gravity wave motions, and that these waves have

preferred directions of propagation. However, for this to be true, one would expect the winds deduced from opposite directions (A and C; B and D) to show the same behaviour, which is not the case. Is there a difference in the specularity and thus apparent motion of wave induced tilts approaching the observer from that of tilts produced by a wave receding from the observer? Such an asymmetry is not intuitively obvious. Whatever the cause, this apparent lack of azimuthal symmetry does, however, support the contention of Hines et al that care must be exercised in the interpretation of IDI winds.

The question then arises - does the apparent self consistency of the IDI results when averaged over all azimuths warrant the publication of the inferred velocities as winds or not? Since they are the best that we can do at this juncture, we believe that the answer is "yes," with an appropriate word of caution. We are confident that the IDI data contains most, if not all, of the information necessary to determine both the bulk motion (the wind) and the wave spectrum, if an appropriate analysis can be devised. With only six days of the six weeks measurements so far subject to scrutiny, the potential certainly exists for significantly increasing our understanding of both the measurement technique and the dynamics of the equatorial mesopause.

WINDS AND IONIZATION As previously mentioned, there is an anomaly in the scattering point population around noon. Interaction between the zonal wind shear and the Earth's magnetic field can result in the "compression" of ionization into a layer at the maximum shear point, provided one has the right sign for the shear - this requires a westward wind at higher altitudes, an eastward wind below (Whitehead, 1989). Arecibo is at 18N geographic latitude, with a magnetic dip angle of 50 degrees. We are able to measure both vertical motion and wind shear, which at mesopause levels we consider to be those of the neutral atmosphere. The vertical shear in the horizontal wind during our measurements was almost entirely due to the diurnal tide, and as can be seen from Figure 3, results at around noon in an eastward wind over a westward, yielding a *dispersive* shear maximizing (at 10m/sec/km) at 96km, the peak of the observed "trough" in metallic ion (Figure 2) and scattering point (Figure 1) densities. While this application of the wind shear theory of sporadic E works in our favor, we cannot overlook the mean vertical motion, which is *downward* over the whole height range for several hours pre to post noon (see Figure 3), with a maximum descent velocity of some 2km/hr. However, as previously discussed in relation to Figures 1 and 2, the observed "trough" in ionization appears at just those times (around noon) when the metallic ions have, to all intents and purposes, disappeared. Thus, the presence of metallic ions may be an important element in the scattering process, at least during these observations.

CONCLUSIONS   Subject to the caveat detailed above, we present a tidal analysis of the IDI scattering point parameter data at upper mesosphere - lower thermosphere altitudes (70 - 110km), using the procedure developed by Groves (1959), over the interval April 5 - 11, 1989 at Arecibo as part of Project AIDA; this analysis has revealed a typical equatorial easterly circulation, with mean meridional circulation becoming significant only above 96km. A periodogram analysis has shown the diurnal tide to be the most significant feature of the wind field at these altitudes, with zonal amplitudes up to some 50 m/s and meridional amplitudes approximately half this value. The two day (48 +-5hr) wave is a significant feature, with an amplitude increasing with height up to some 30 m/s at 110km. The semidiurnal tide is well developed in both zonal and meridional directions only above 96km. Both 8 and 6 hour components become significant above 100km - in fact, the 6 hour component is as strong as both the 24 and 12 hour tides at 110km.

Much of the evidence substantiating the above as winds is circumstantial - for example, if it looks like a tide and behaves like a tide, it must be a tide; because of the azimuthal inhomogeniety evident in these results, the absolute values of the amplitudes and phases deduced may be questionable.

The anomalous lack of scattering points after noon has been explained in terms of the wind shear theory of sporadic E (Whitehead, 1989).

REFERENCES.

Adams, G.W., J.W. Brosnahan, and D.P. Edwards, "The imaging Doppler interferometer: Data analysis," Radio Sci. 20(6), 1481-1492, 1985.

Adams, G.W., J.W. Brosnahan, D.C. Walden, and S.F. Nerney, "Mesospheric observations using a 2.66 MHz radar as an imaging Doppler interferometer: Description and first results," J. Geophys. Res. 91(A2), 1671-1683, 1986.

Adams, G.W., A.W. Peterson, J.W. Brosnahan, and J.W. Neuschaefer, "Radar and optical observations of mesospheric wave activity during the lunar eclipse of 6 July 1982," J. Atmos. Terrest. Phys. 50(1),11-20, 1988a.

Adams, G.W., J.W. Brosnahan, and T.D. Halderman, "Direct radar observations of TIDs in the D- and E-regions," J. Atmos. Terrest. Phys. 50(10/11), 931-935, 1988b.

Brosnahan, J.W., and G.W. Adams, "The MAPSTAR imaging Doppler interferometer (IDI) radar: system description and first wind comparisons," J. Atmos. Terrest. Phys., (this issue), 1992

Franke, Patricia M., Denise Thorsen, Mark Champion, Steven J, Franke, and Erhan Kudeki, "Comparison of time and frequency domain techniques for wind velocity estimation using multiple receiver MF radar data," Geophys. Res. Lett., 17, 2193-2196, 1990.

Groves, G.V., "A theory for determining upper atmosphere winds from radio observations on meteor trails," J. Atmos. Terrest. Phys. 16, 344-356, 1959.
Hines, C.O., Gene W. Adams, John W. Brosnahan, Frank T. Djuth, Michael P. Sulzer, Craig A. Tepley, and Joel S. Van Baelen, " Mesospheric wind and partial reflection observations: comparisons and interpretations," J. Atmos. Terrest. Phys., (this issue), 1992

Lindzen, R.S., "The application of classical atmospheric tidal theory," Proc. R. Soc. London Ser. A303, 299-316, 1968.

Lindzen, Richard S. and Sydney Chapman, "Atmospheric Tides," Space Sci. Rev., 10, 3-188, 1969

Mathews, J.D., "Measurement of the diurnal tide in the 80 to 100 km altitude range at Arecibo," J. Geophys. Res., 41, 4671, 1976.

Mathews, J.D., Y.T. Morton and Q. Zhou, "Tides and acoustic-gravity waves observed in the motions of ionospheric E region meteoric ion layers." J. Atmos. Terrest. Phys., (this issue), 1992

Stubbs, T.J. "The measurement of winds in the D-region of the ionosphere by the use of partially reflected radio waves," J. Atmos. Terrest. Phys., 35, 909-919, 1973.

Whitehead, J.D. "Recent work on midlatitude and equatorial sporadic E," J. Atmos. Terrest. Phys., 51, 401-424, 1989.

Wang, Ding-Yi and David C. Fritts, "Mesospheric momentum fluxes observed by the MST radar at Poker Flat, Alaska," J. Atmos. Sci., 47, 1512-1521, 1990.

EAST-WEST WIND COMPONENTS,   ARECIBO (18N,67W)
APL 5 - APL 11 1989

| | | | 24 HOUR | | | | 12 HOUR | | |
HEIGHT	MEAN	ERROR	AMP	ERROR	PHI	ERROR	AMP	ERROR	PHI	ERROR
110	-9.	2.	22.	3.	21.	1.	30.	3.	6.	0.
106	-8.	2.	9.	2.	1.	1.	27.	2.	7.	0.
102	-6.	1.	22.	2.	7.	0.	23.	2.	7.	0.
98	-5.	1.	30.	2.	9.	0.	18.	1.	7.	0.
94	-8.	1.	26.	1.	11.	0.	13.	1.	7.	0.
90	-13.	1.	20.	1.	14.	0.	12.	1.	5.	0.
86	-20.	1.	23.	2.	18.	0.	11.	1.	5.	0.
82	-24.	1.	33.	2.	21.	0.	5.	2.	3.	1.
78	-24.	2.	45.	2.	24.	0.	10.	3.	11.	0.
74	-18.	2.	48.	3.	2.	0.	22.	3.	11.	0.
70	-2.	4.	3.	6.	22.	8.	18.	6.	11.	1.

NORTH-SOUTH WIND COMPONENTS ARECIBO (18N,67W)
APL 5 - APL 11 1989

| | | | 24 HOUR | | | | 12 HOUR | | |
HEIGHT	MEAN	ERROR	AMP	ERROR	PHI	ERROR	AMP	ERROR	PHI	ERROR
110	-8.	2.	32.	3.	16.	0.	29.	3.	3.	0.
106	-13.	2.	22.	2.	19.	0.	29.	2.	3.	0.
102	-15.	1.	19.	2.	23.	0.	22.	1.	4.	0.
98	-13.	1.	23.	1.	2.	0.	12.	1.	4.	0.
94	-8.	1.	22.	1.	4.	0.	4.	1.	4.	1.
90	-3.	1.	19.	1.	6.	0.	1.	1.	11.	3.
86	1.	1.	20.	1.	9.	0.	2.	1.	11.	1.
82	1.	1.	20.	2.	12.	0.	2.	1.	2.	1.
78	-2.	2.	16.	2.	14.	1.	5.	2.	4.	1.
74	-5.	2.	12.	3.	18.	1.	8.	3.	5.	1.
70	-1.	3.	7.	4.	1.	3.	4.	5.	6.	2.

VERTICAL WIND COMPONENTS,   ARECIBO (18N,67W)
NOTE - VELOCITIES ARE IN CM/S
APL 5 - APL 11 1989

| | | | 24 HOUR | | | | 12 HOUR | | |
HEIGHT	MEAN	ERROR	AMP	ERROR	PHI	ERROR	AMP	ERROR	PHI	ERROR
110	-9.	20.	92.	33.	7.	1.	234.	30.	4.	0.
106	-18.	14.	54.	25.	6.	2.	186.	23.	4.	0.
102	-35.	10.	33.	16.	14.	2.	95.	17.	4.	0.
98	-41.	8.	61.	15.	15.	1.	35.	15.	3.	1.
94	-33.	7.	34.	13.	15.	2.	17.	13.	2.	1.
90	-13.	6.	17.	13.	3.	3.	17.	13.	5.	1.
86	11.	8.	41.	15.	2.	1.	53.	15.	6.	1.
82	29.	10.	31.	18.	21.	2.	95.	17.	7.	0.
78	36.	15.	115.	25.	17.	1.	137.	23.	7.	0.
74	33.	21.	188.	33.	16.	1.	160.	31.	7.	0.
70	34.	36.	58.	50.	14.	4.	212.	53.	6.	0.

Table 1.   The variation with height of the zonal (m/s), meridional (m/s) and vertical (cm/s) mean (prevailing), diurnal and semidiurnal winds.

Note that the tidal phases are local mean solar time.

Number of Scattering Points per Sounding

Day in April 1989 (marked at noon LMT)
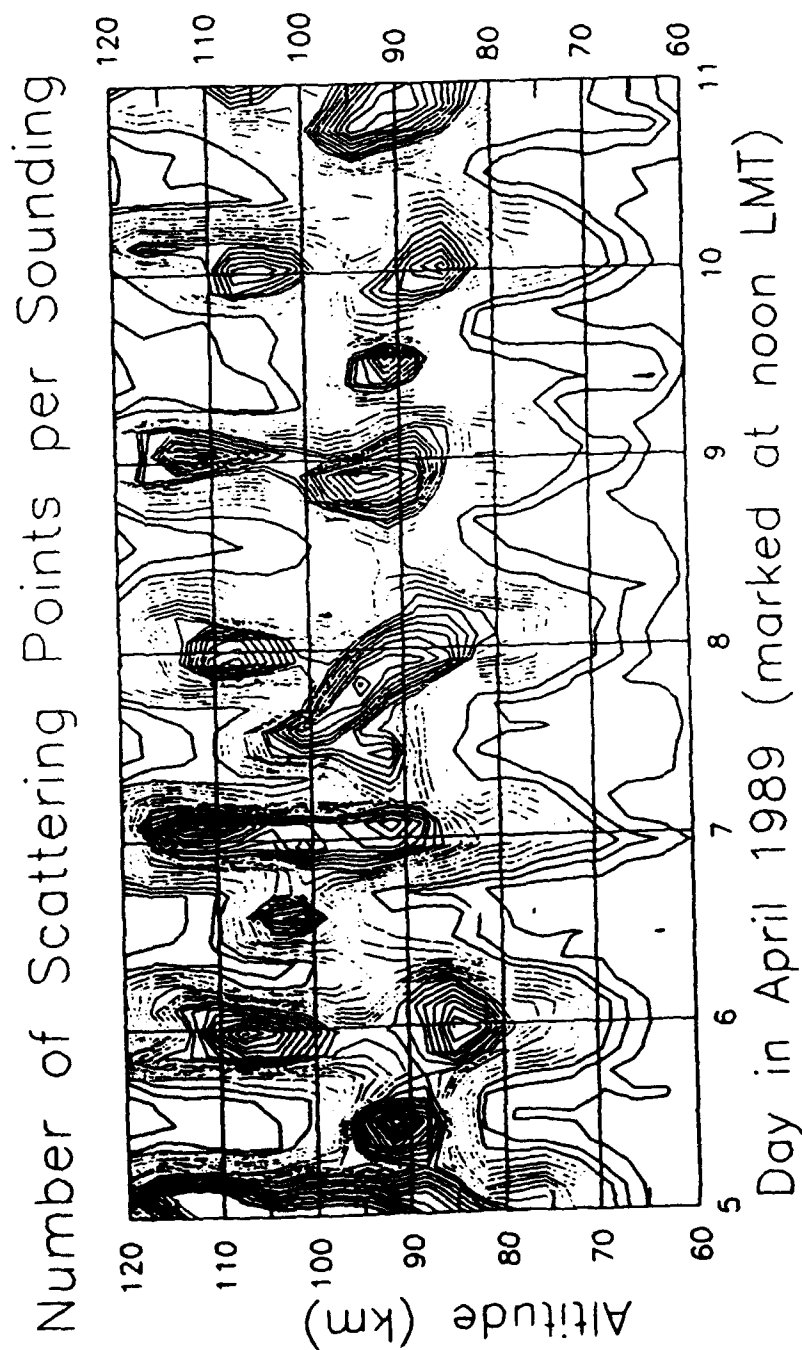
Altitude (km)

Figure 1. The distribution, in altitude and time, of the number of scattering points per sounding per range gate.

Red - 0 to 9

Green - 10 to 29

Blue > 30 points.

61
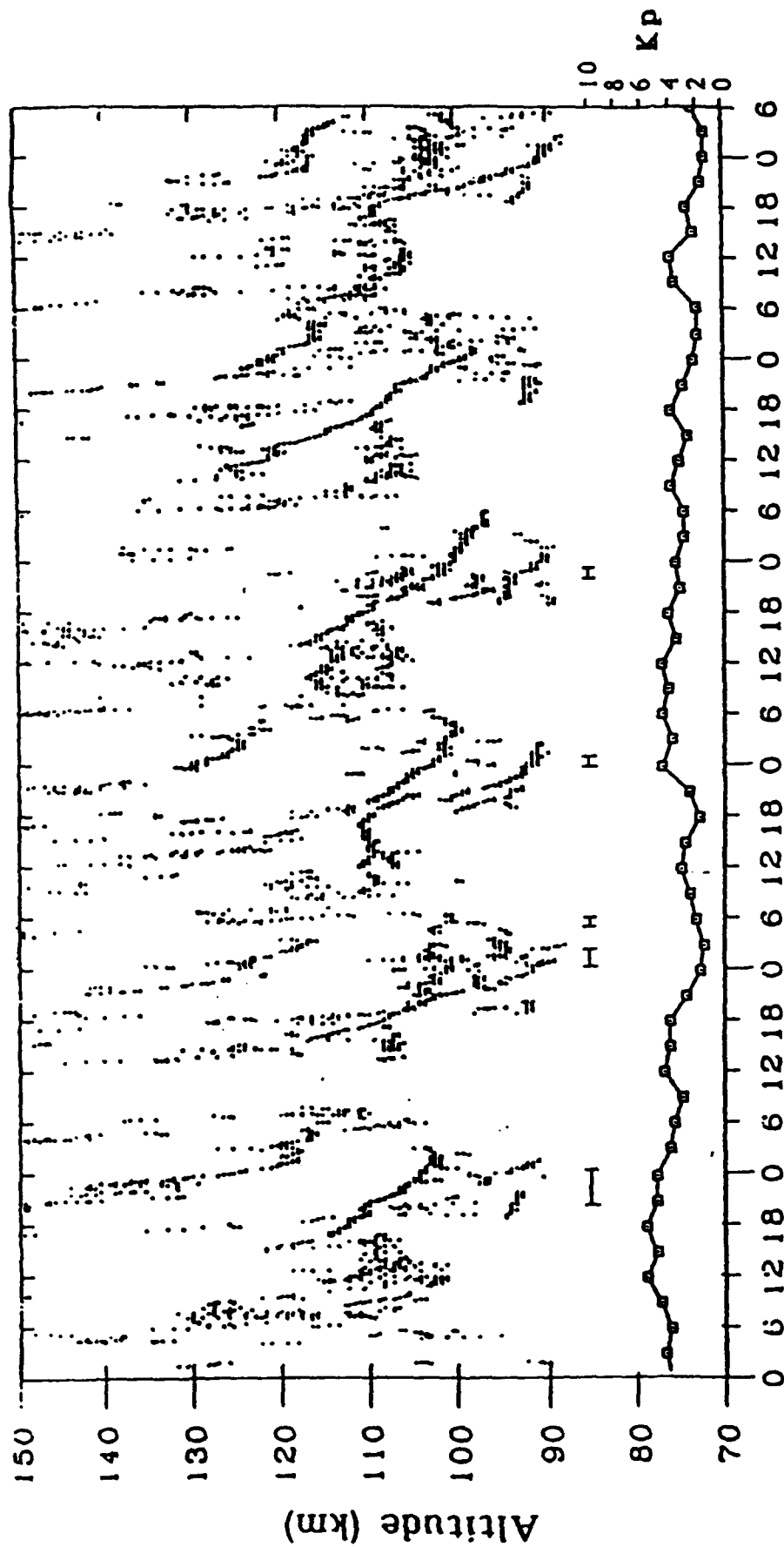
Figure 2. Layer (metallic ion) trajectories obtained with the Arecibo Incoherent Scatter Radar for April 4 - 10, 1989, as part of the AIDA'89 campaign (from Mathews et al., this issue)
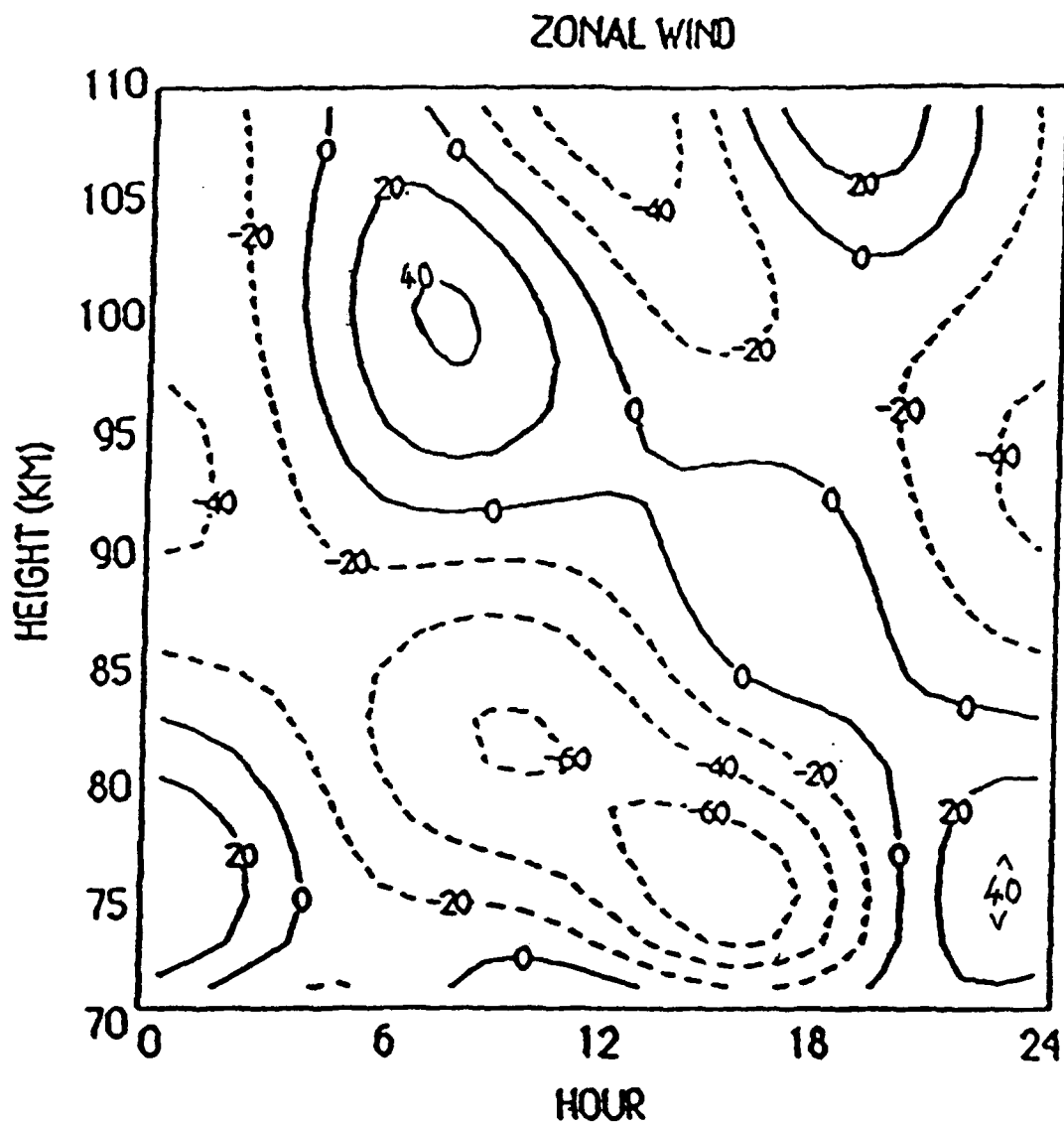
ZONAL WIND

Figure 3a.   Contour plot of the zonal wind component and its variation
             with height, over the height range 70 to 110km. Note that
             this is the average behaviour of the mean, diurnal and
             semidiurnal winds over the interval April 5 - 11, 1989.
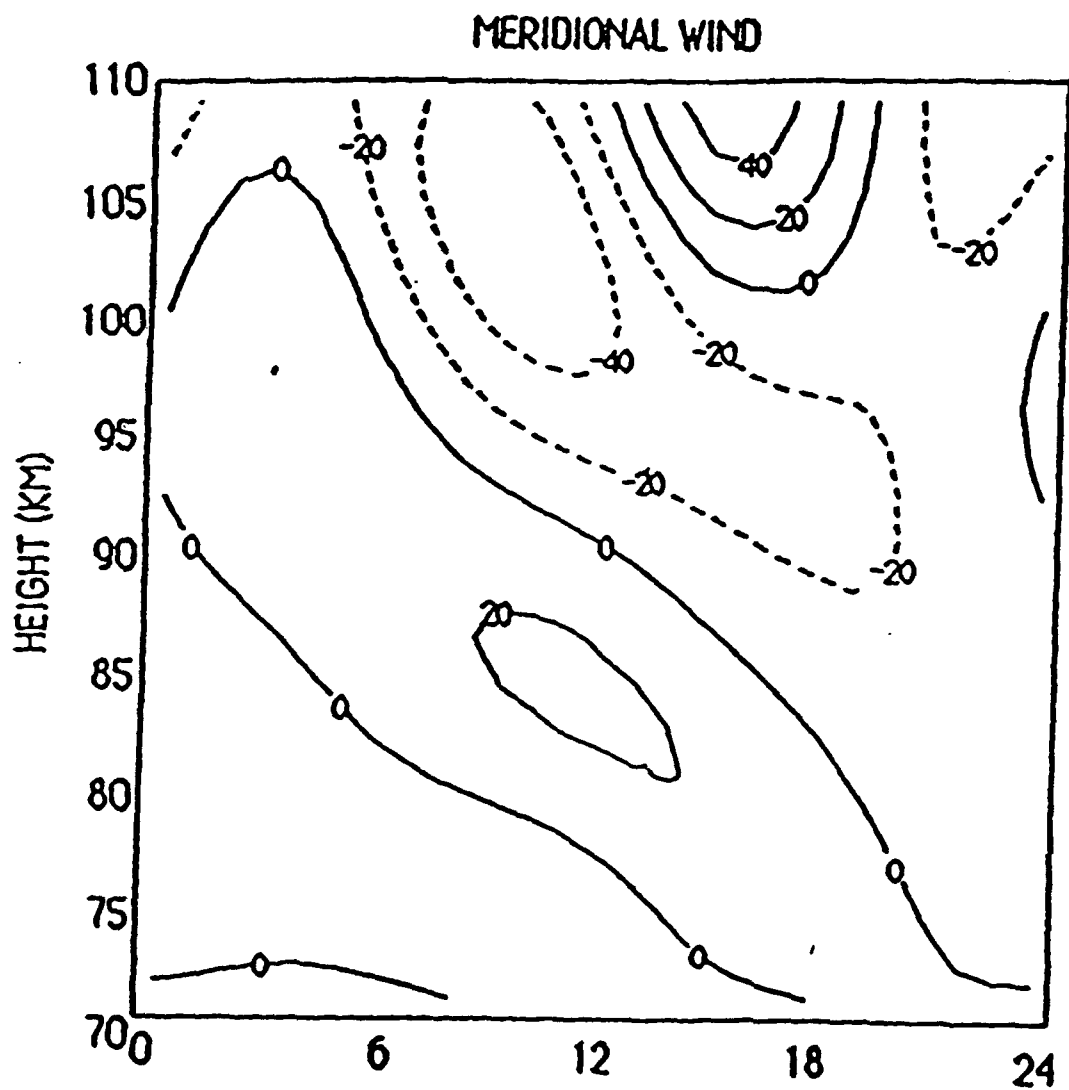
Figure 3b.   As for Figure 3a, but for the meridional wind component.
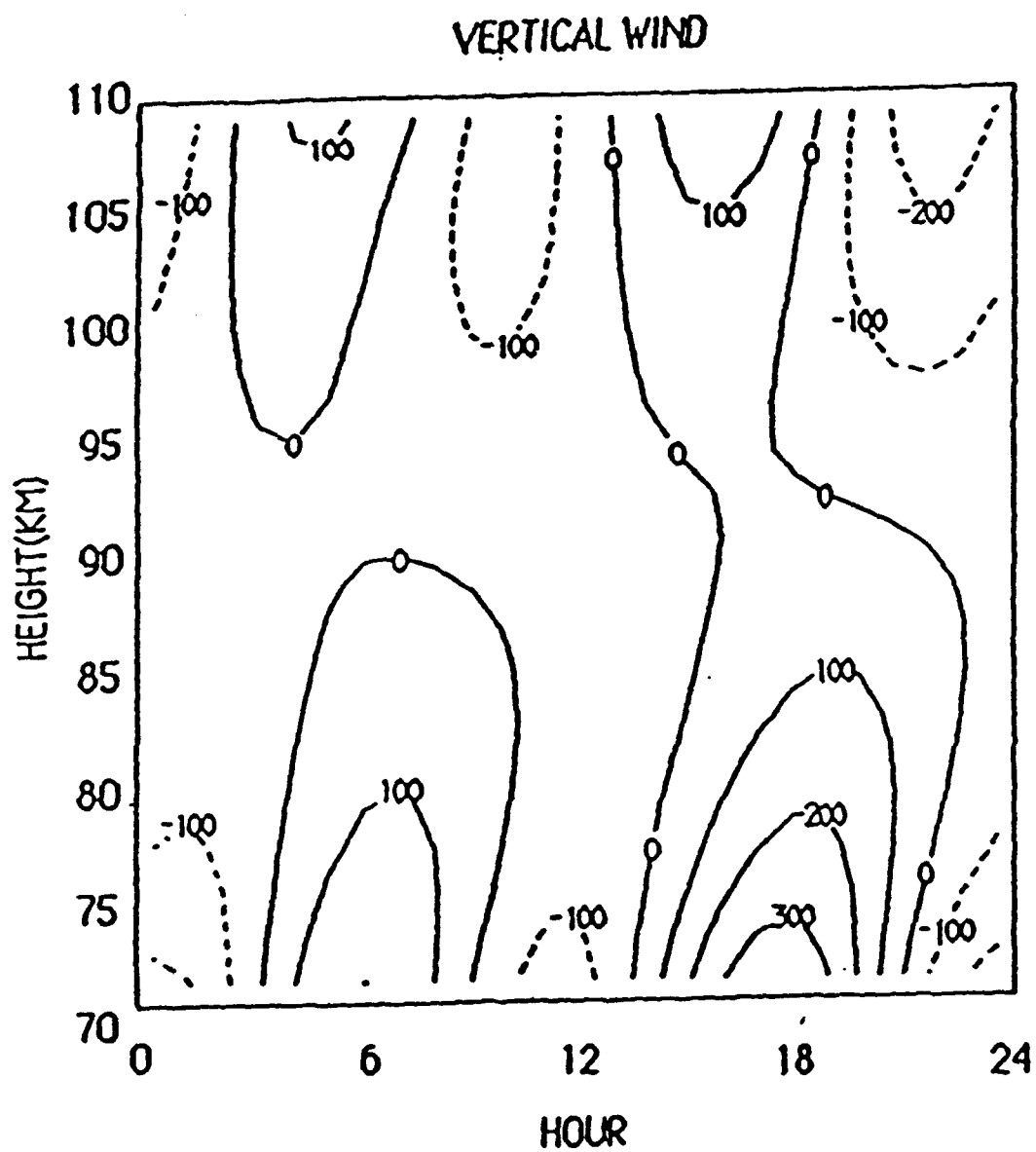
Figure 3c.   As for Figure 3a, but for the vertical wind component. Note that the vertical velocity is in centimeters per second.
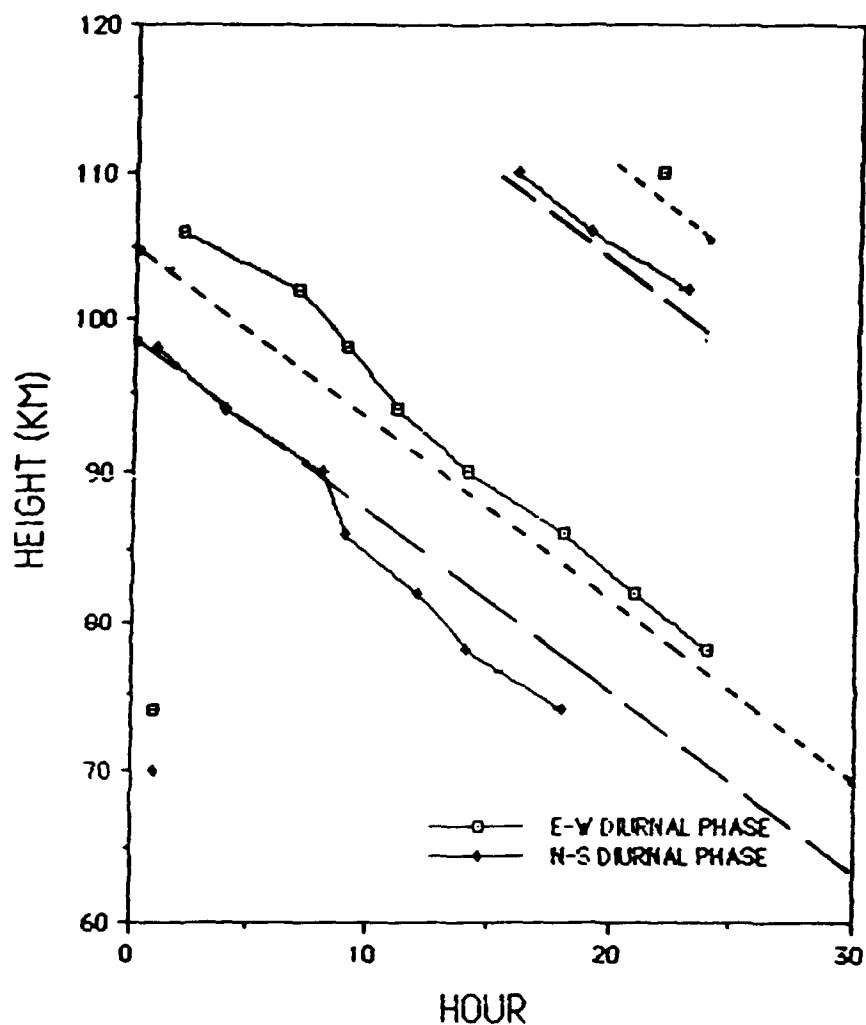
Figure 4.   The average variation with height of the zonal and
             meridional diurnal tidal phases for the April 5-11, 1989
             interval. The phase of each is the hour of the respective
             eastward and northward amplitude maximum relative to
             midnight. The short dashed line is the zonal and the long
             dashed line the meridional phase for the S_1^1 mode for equinox
             at 15° latitude (from Lindzen and Chapman, 1969).

66
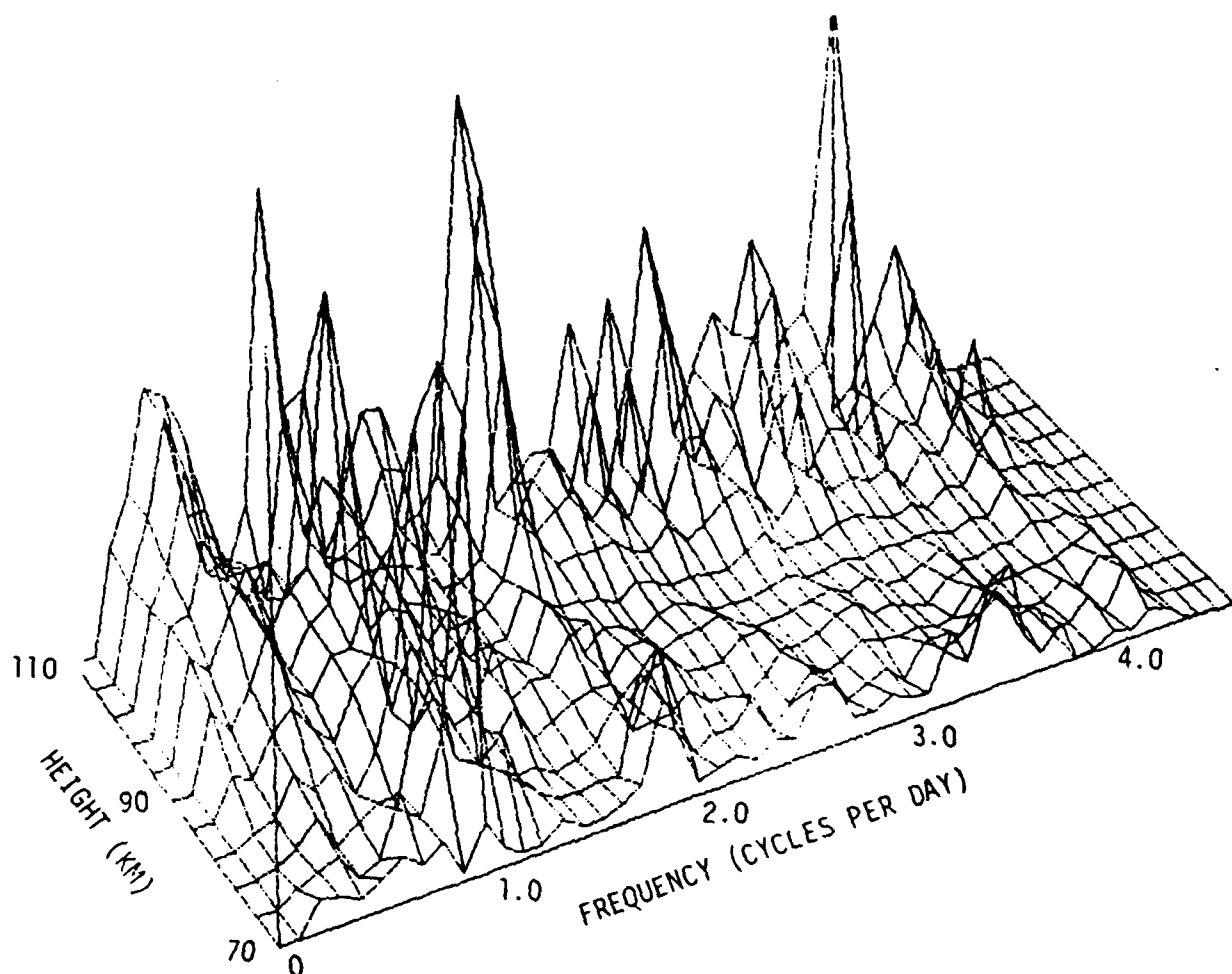
Figure 5.   3D surface plot of the wind energy spectrum (determined by a periodogram analysis from 0.2 to 4.5 cpd in steps of 0.1 cpd) over the 70 to 110km height range. The wind energy is expressed as the sum of the squares of the zonal, meridional and vertical velocities in m/s.
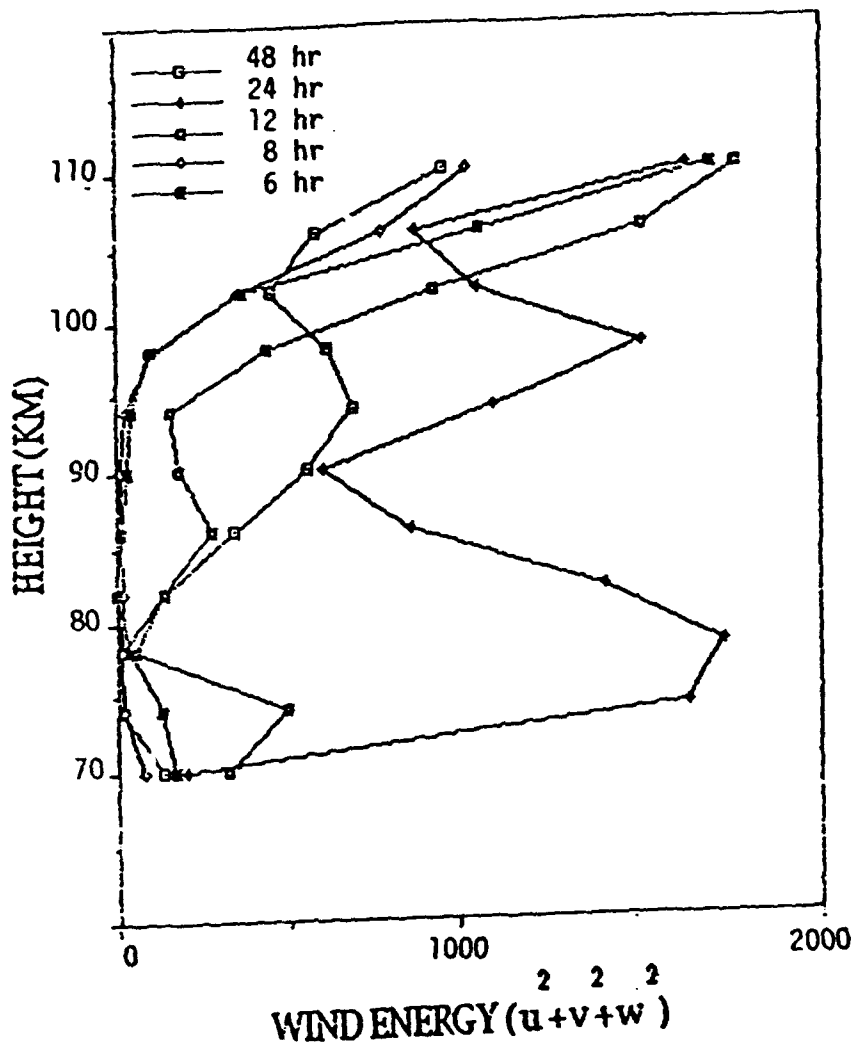
Figure 6.   The variation with height of the energy of the two day (48
hour), 24, 12, 8 and 6 hour components. Again, wind energy
is the sum of the squares of the zonal, meridional and vertical
wind velocities in m/s. The diurnal is the most significant
component below 100km.

ZONAL WIND, ARECIBO APRIL 5-11, 1989
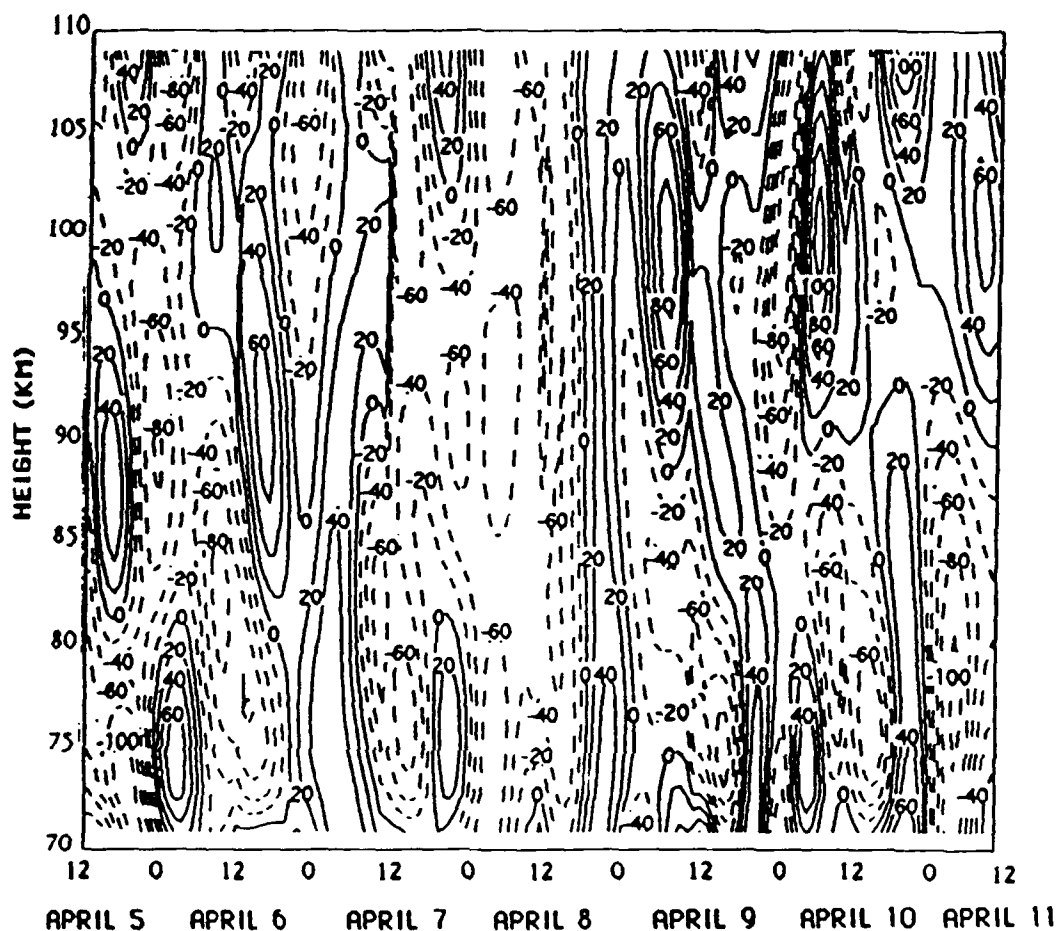
Figure 7a.   A montage of the contour plots of winds determined from the application of Groves' analysis to six 24 hour segments of IDI data, commencing from noon local mean solar time (LMST) on April 5.

MERIDIONAL WIND, ARECIBO APRIL 5-11, 1989
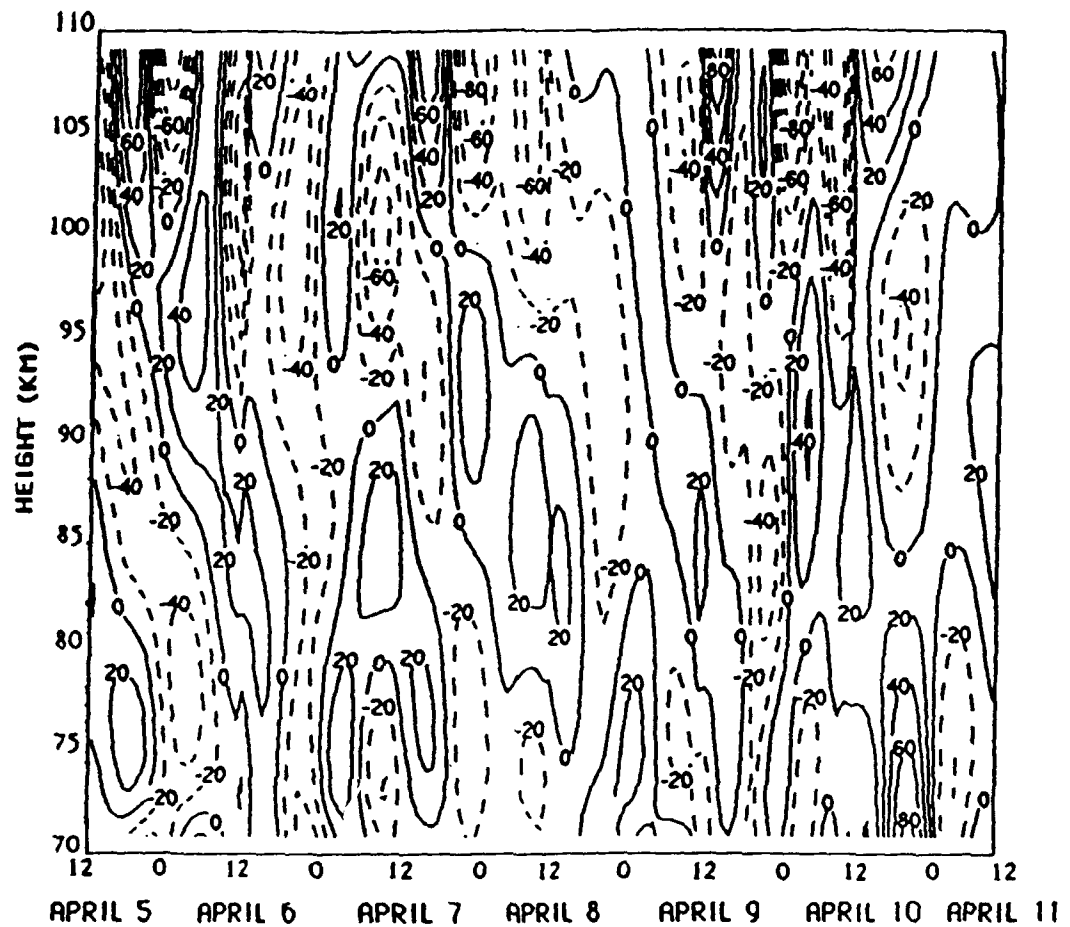
Figure 7b.   As for Figure 7a but for the meridional component.

VERTICAL WIND, ARECIBO APRIL 5-11, 1989
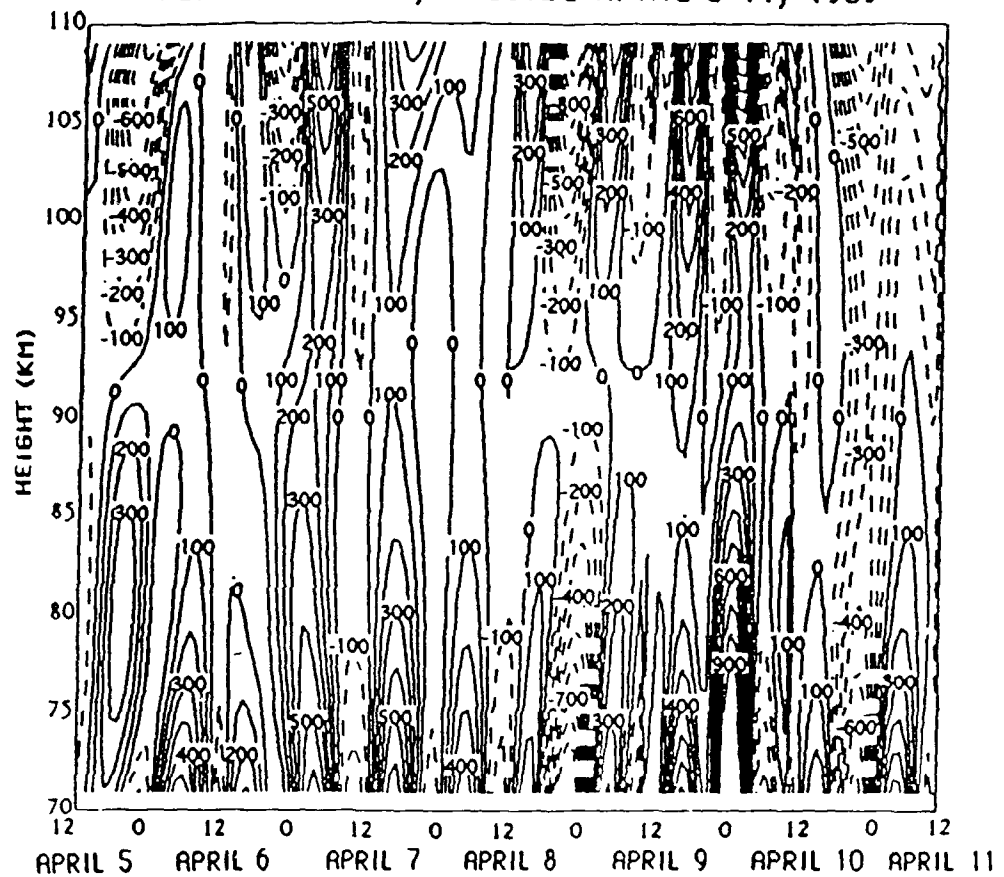
Figure 7c   As for figure 7a but for the vertical component, Note that the vertical winds are in centimeters per second.
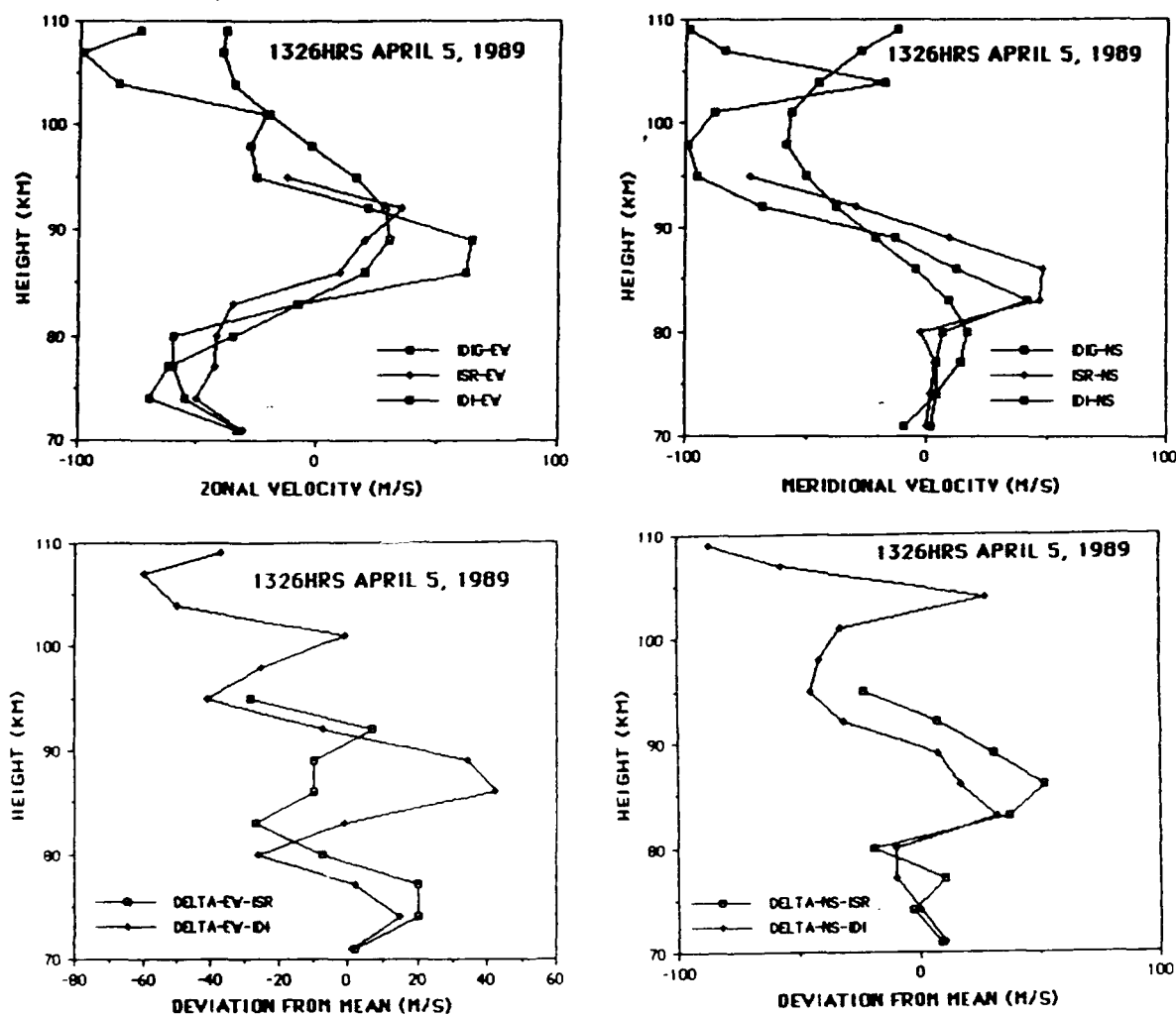
Figure 8a   Comparison between the IDI zonal and meridional wind
              profiles over Arecibo at 1326hrs on April 5, 1989 and
              the profiles defined as the mean wind, which are derived
              from the IDI/MSC April 5-6 data (from noon to noon)
              subjected to Groves (1959) analysis to determine the
              background wind consisting of prevailing, 24 and 12 hour
              components only. See text for details of the parameters fitted
              to the data. Also plotted are the respective ISR wind
              components as measured below 95km (from Hines et al.
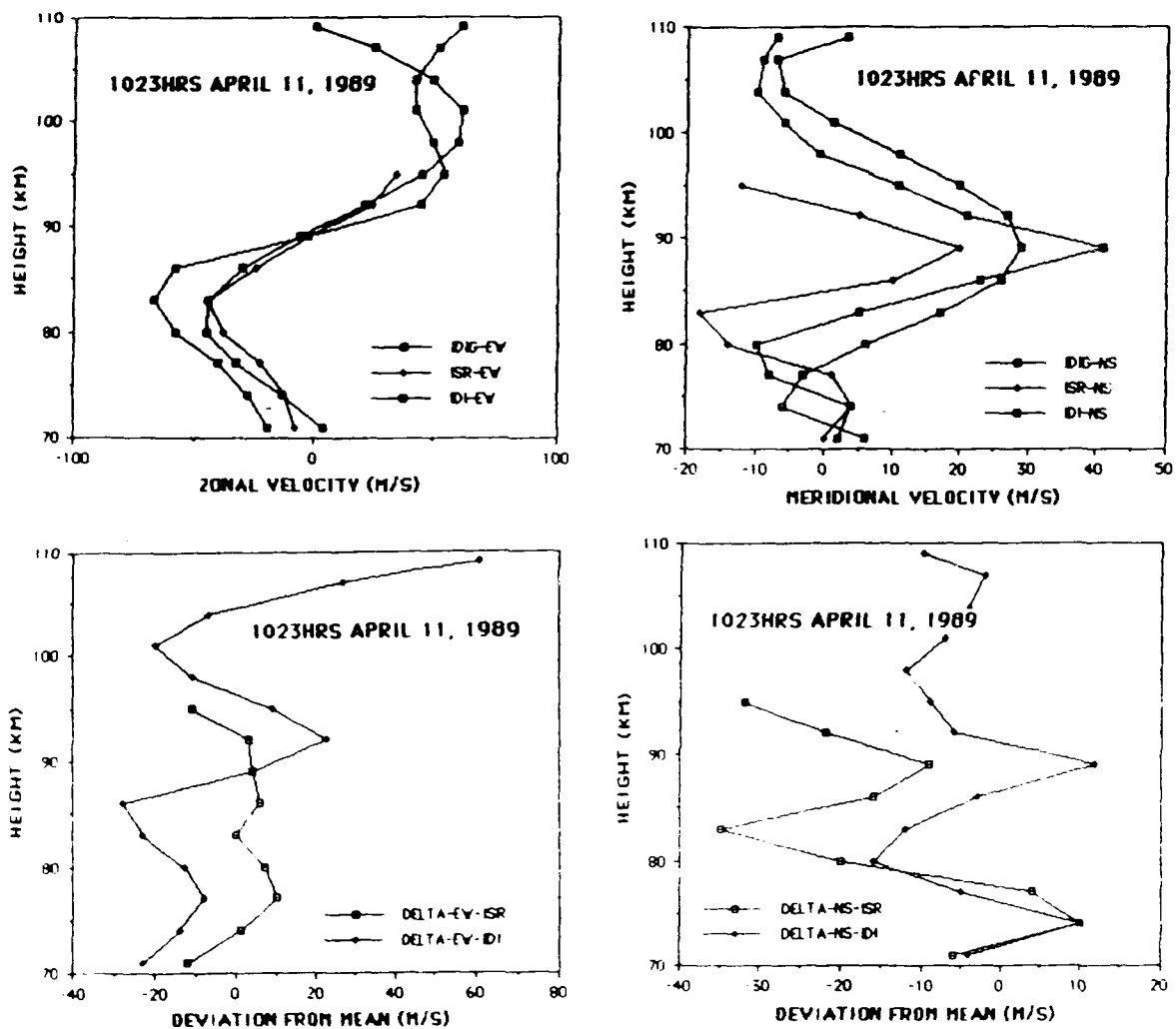   1992)
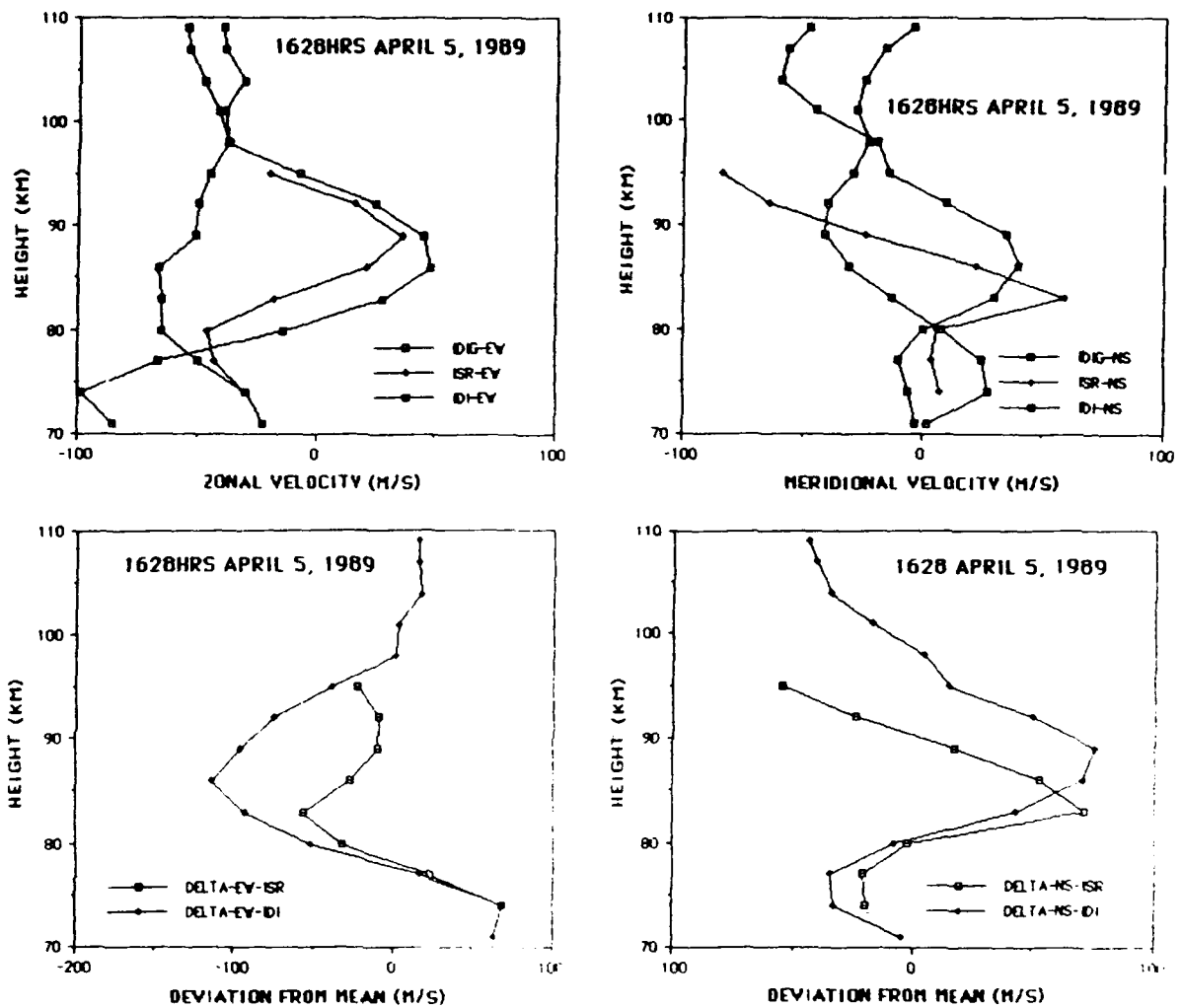
Figure 8b   As for Figure 8a, except for 1628hrs on April 5.
             Note that the same (April 5-6) prevailing plus tidal
   winds apply to this comparison also
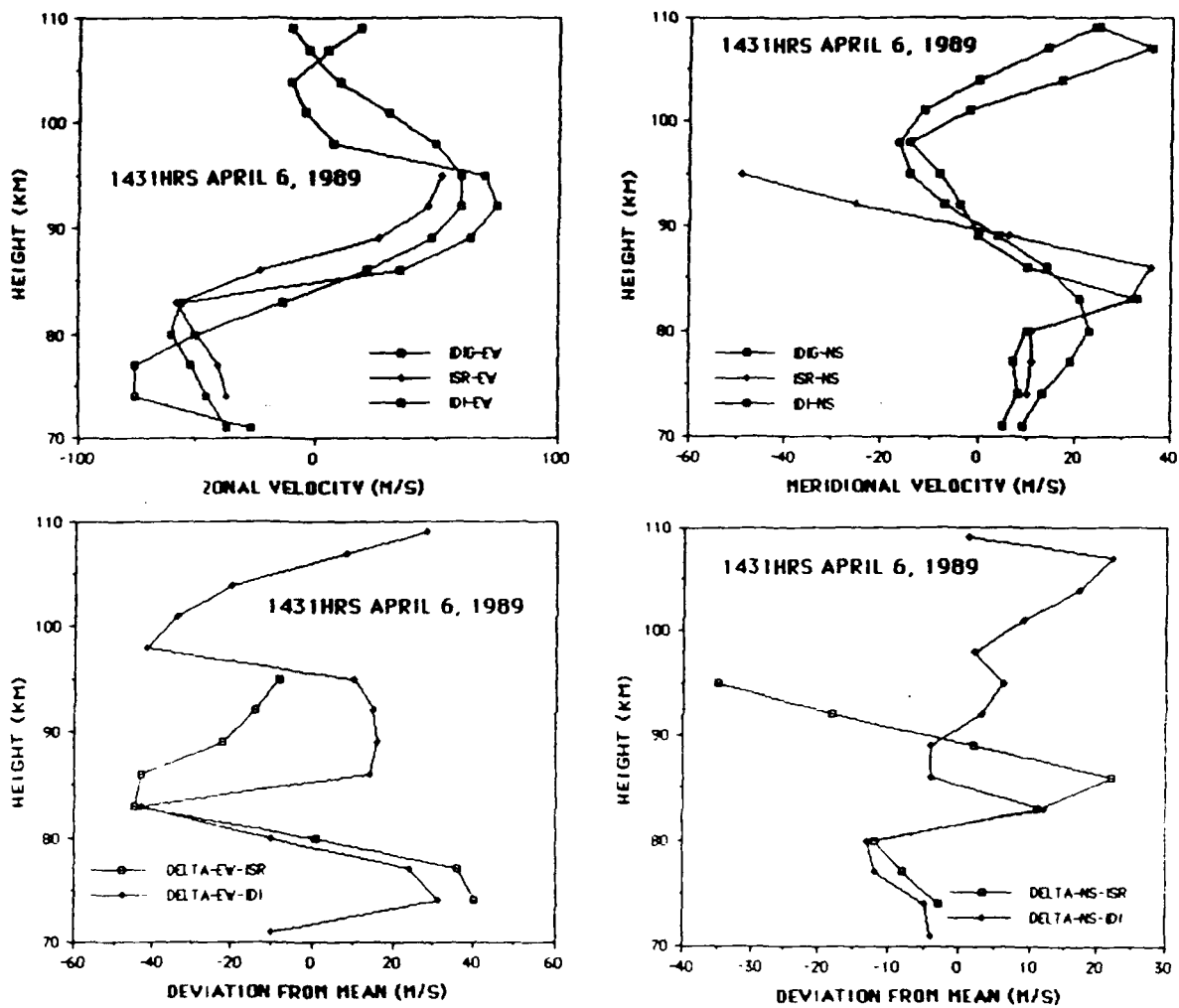
Figure 8c   As for Figure 8a, except for 1431 hrs on April 6.
A new set of Groves' coefficients has been determined
for April 6-7.
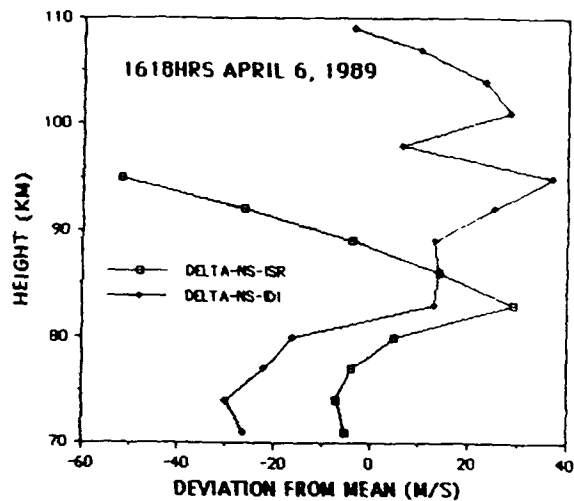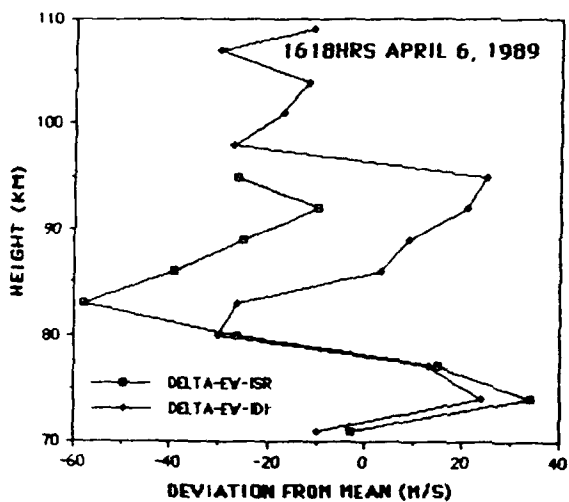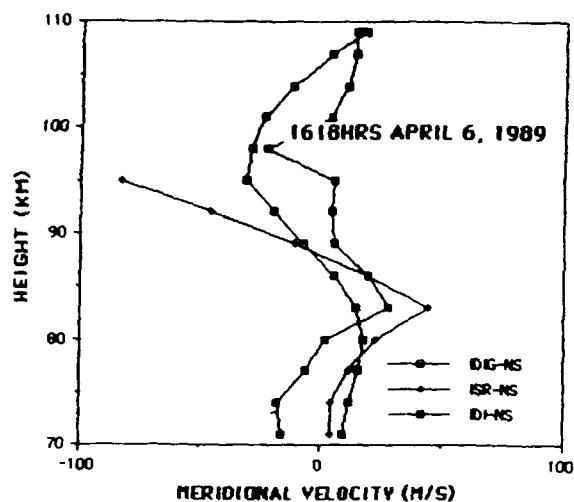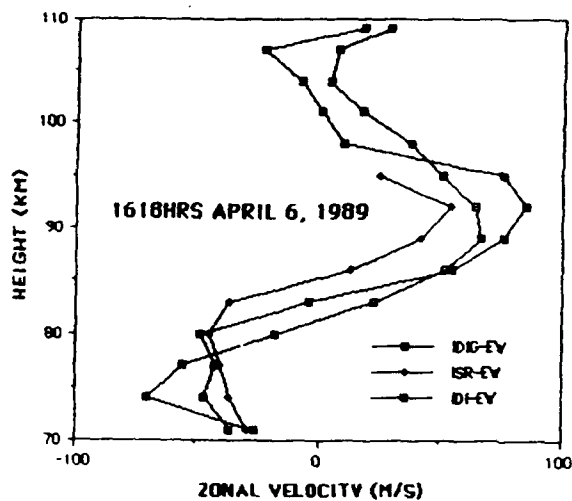
Figure 8d   As for Figure 8a, except for 1618hrs on April 6.
             Note that the same (April 6-7) prevailing plus tidal
             winds apply to this comparison also.
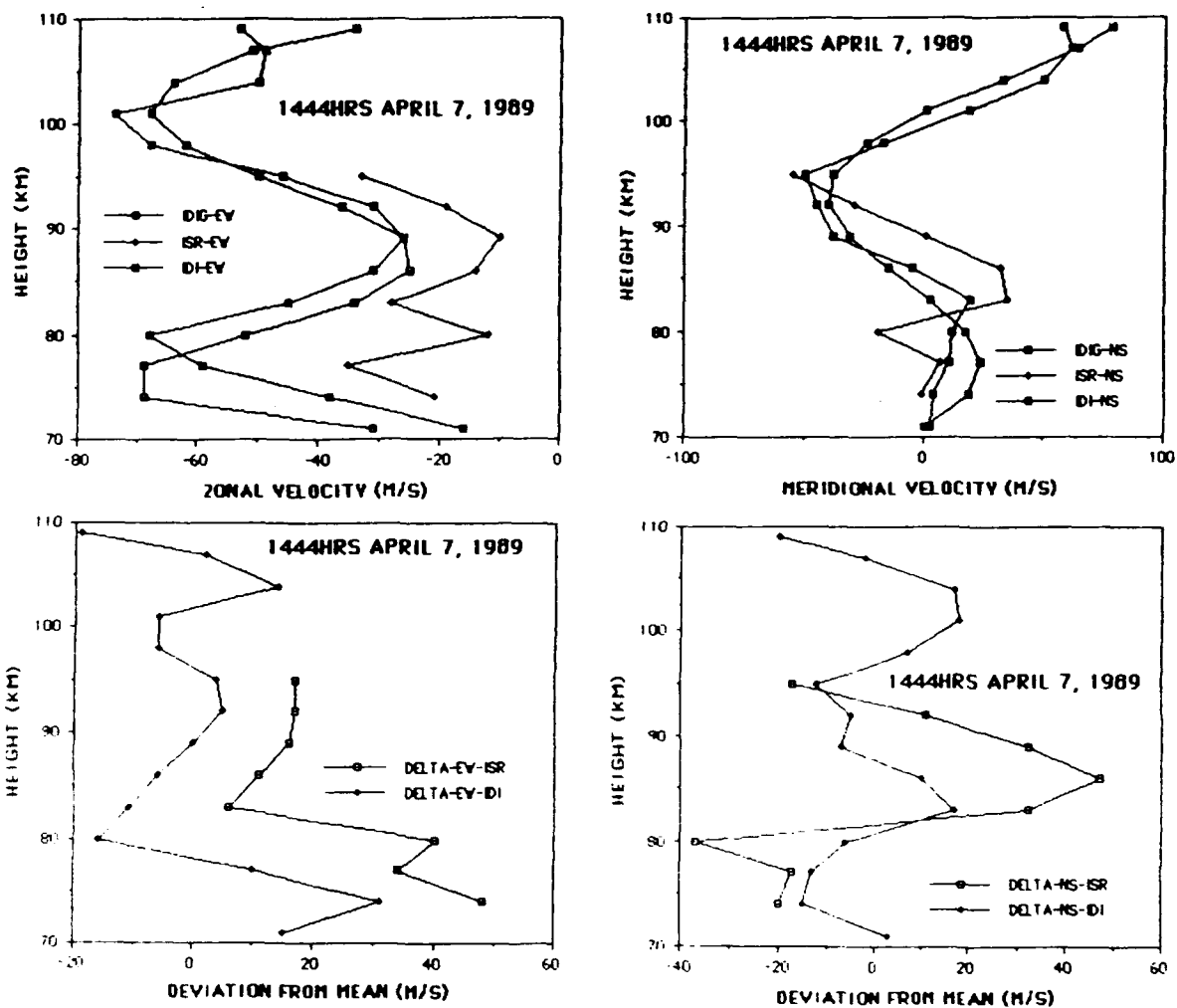
Figure 8e   As for Figure 8a, except for 1444hrs on April 7.
             A new set of Groves' coefficients has been determined
             for April 7-8.
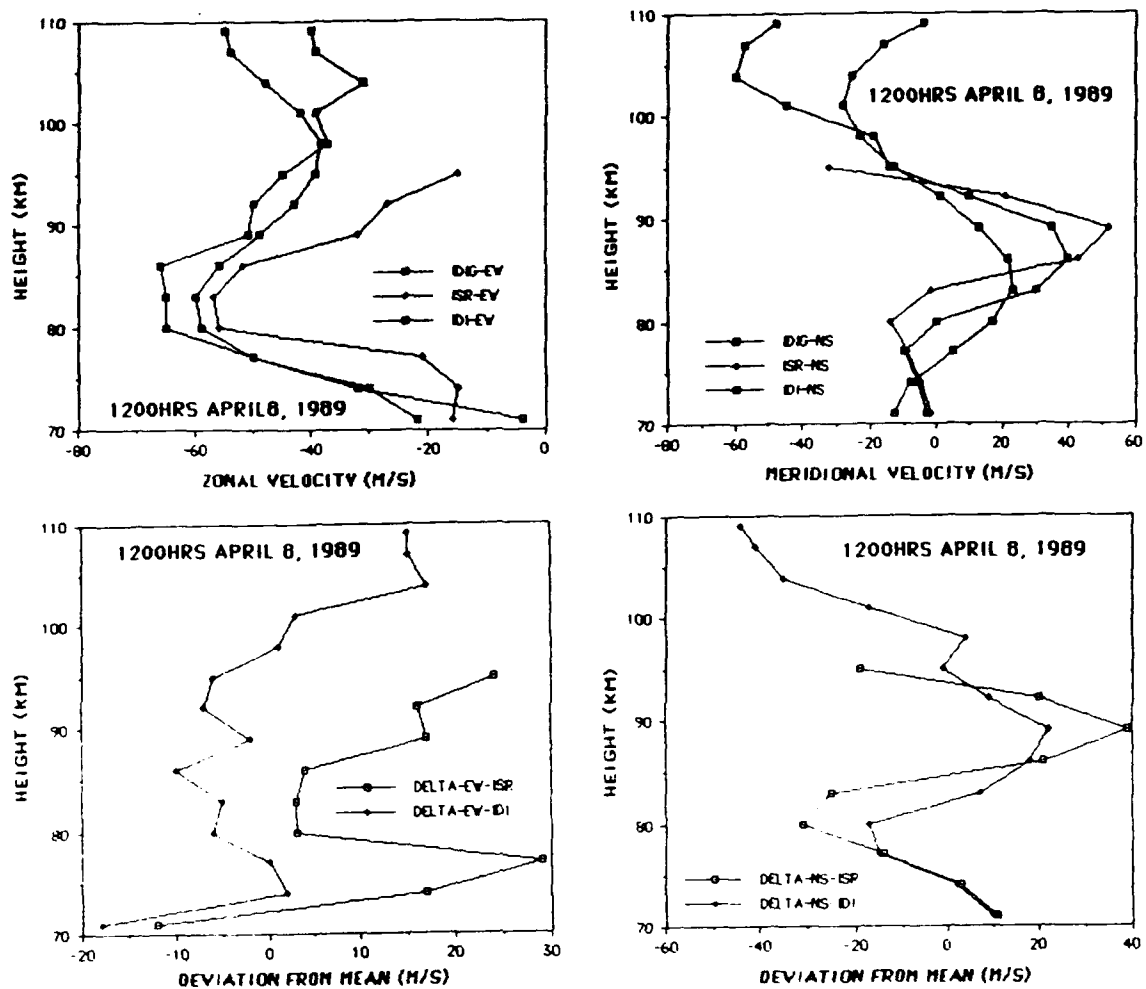
Figure 8f   As for Figure 8a, except for 1200hrs on April 8.
                 A new set of Groves' coefficients has been determined
                 for April 8-9.
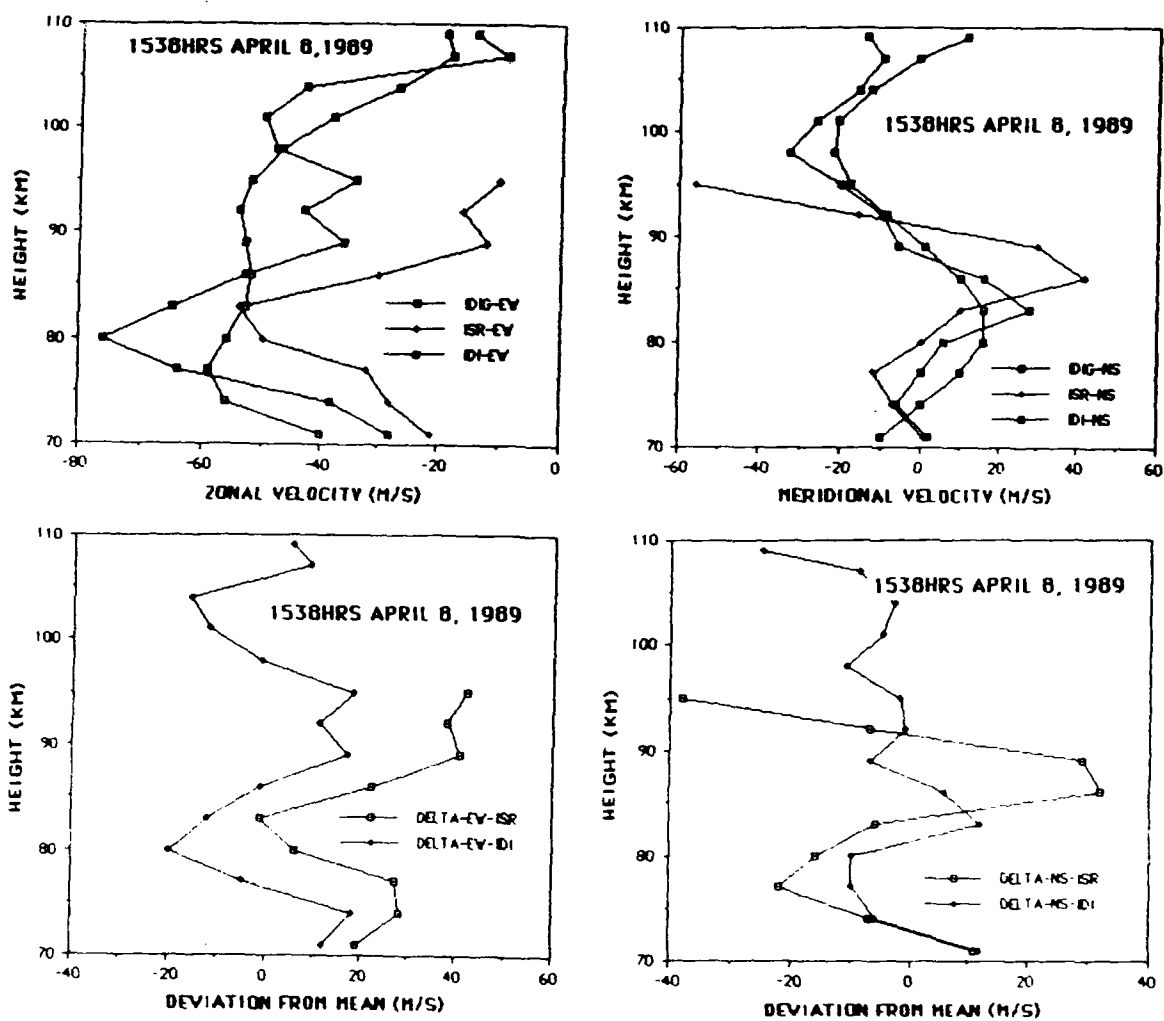
Figure 8g   As for Figure 8a, except for 1538hrs on April 8.
               Note that the same (April 8-9) prevailing plus tidal
               winds apply to this comparison also.
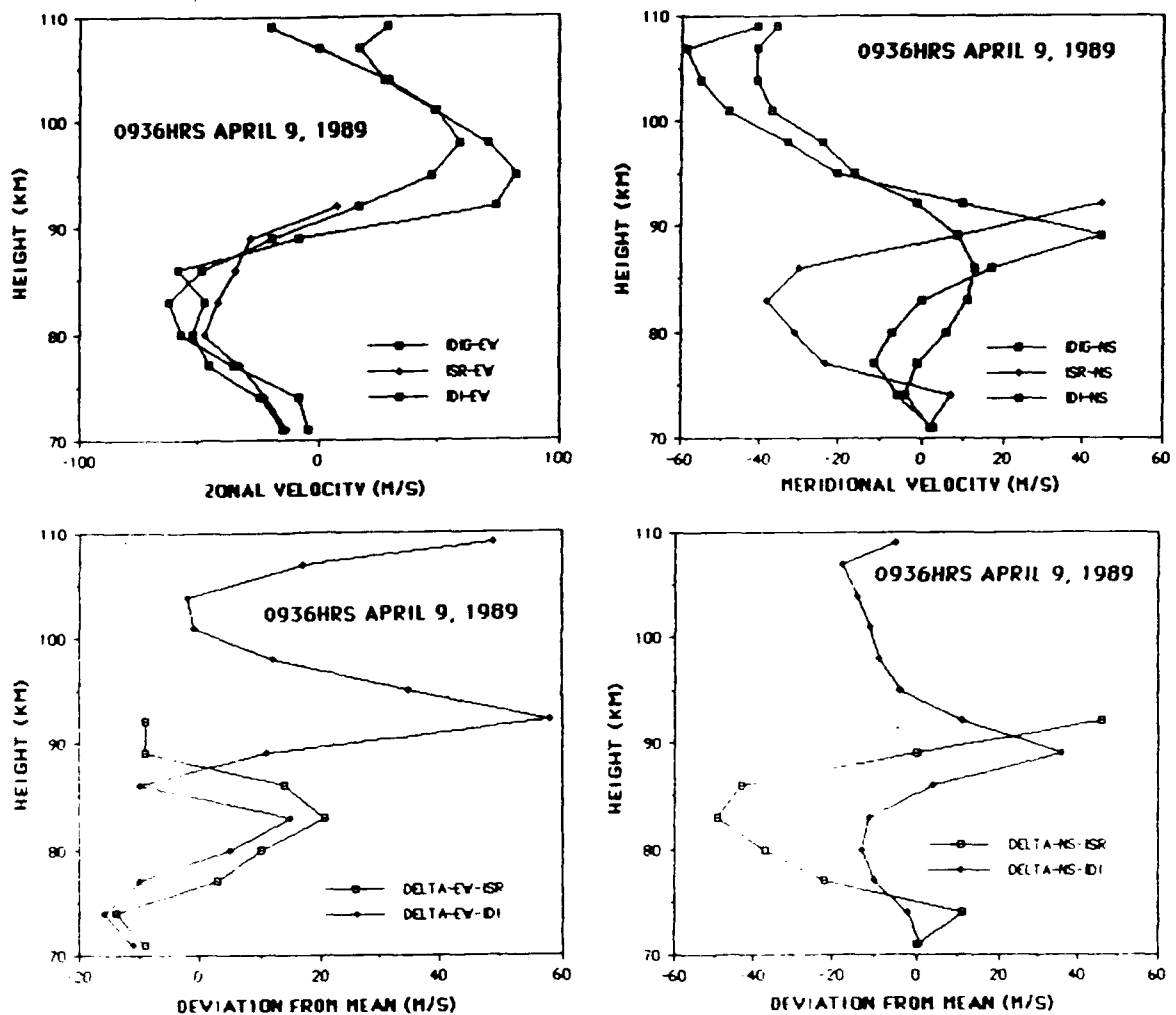
Figure 8h   As for Figure 8a, except for 0936hrs on April 9.
             Note that the same (April 8-9) prevailing plus tidal
             winds apply to this comparison also.
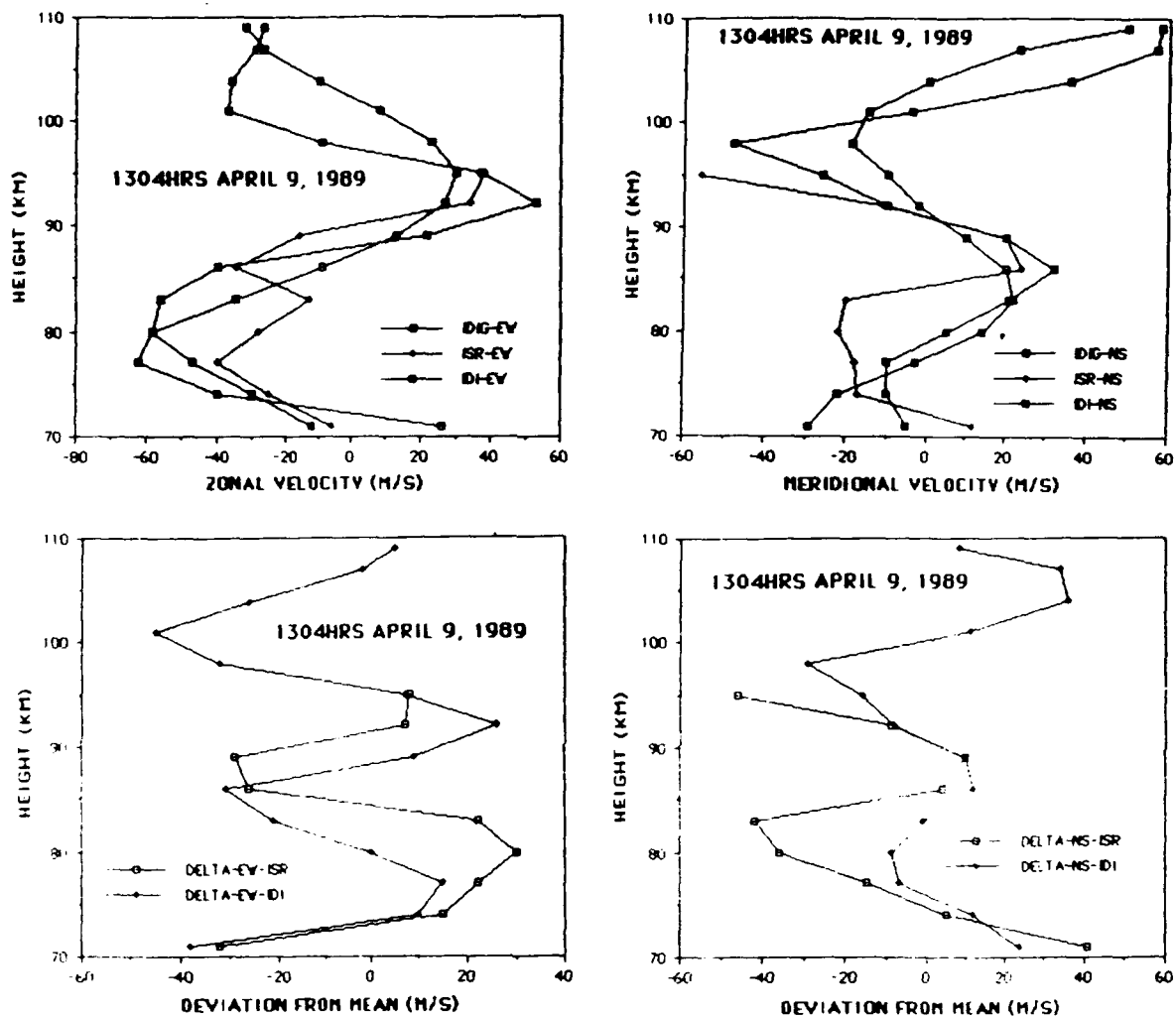
Figure 8j   As for Figure 8a, except for 1304hrs on April 9.
A new set of Groves' coefficients has been determined
for April 9-10.
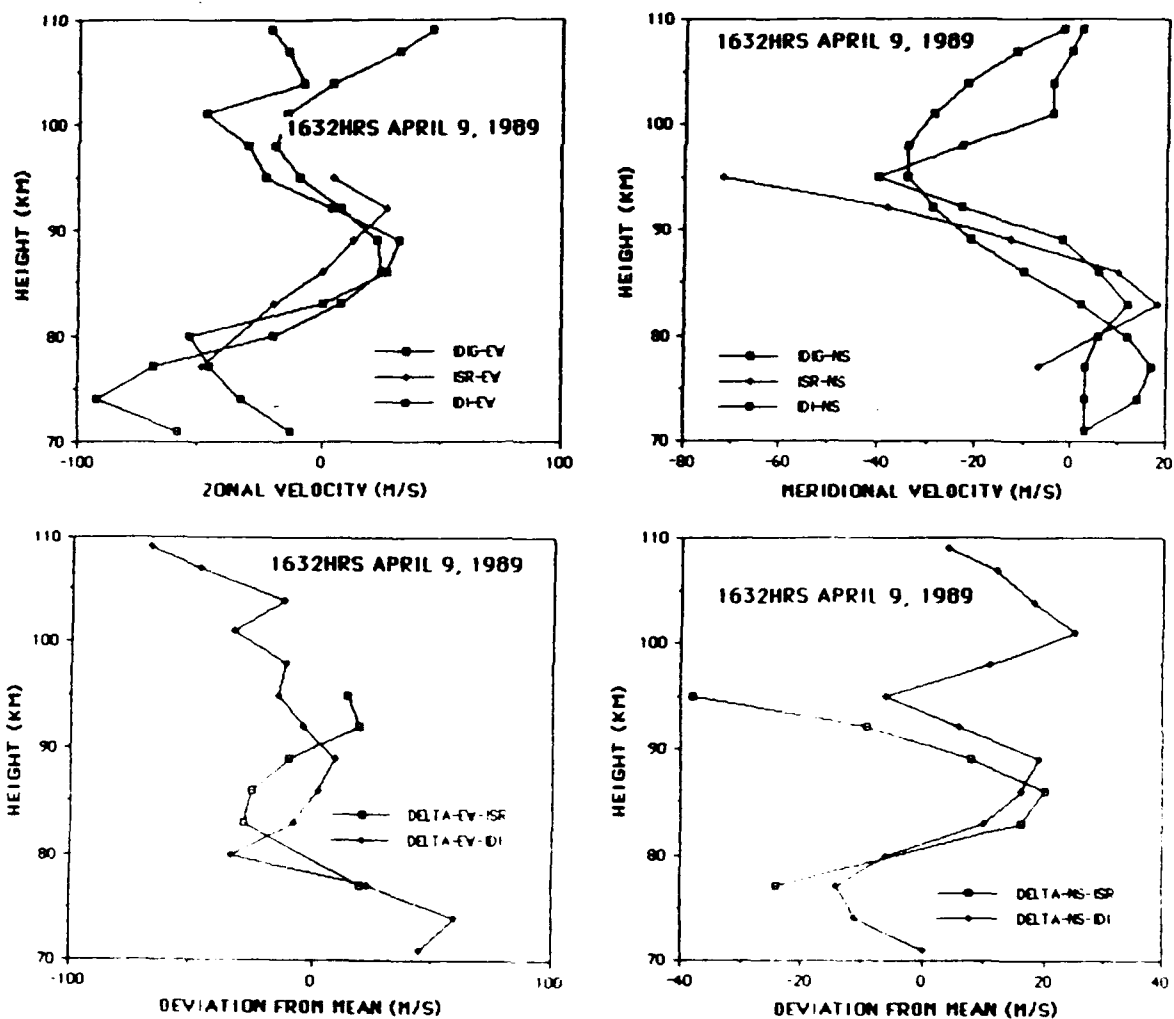
Figure 8k   As for Figure 8a, except for 1632hrs on April 9.
              Note that the same (April 9-10) prevailing plus tidal
              winds apply to this comparison also.
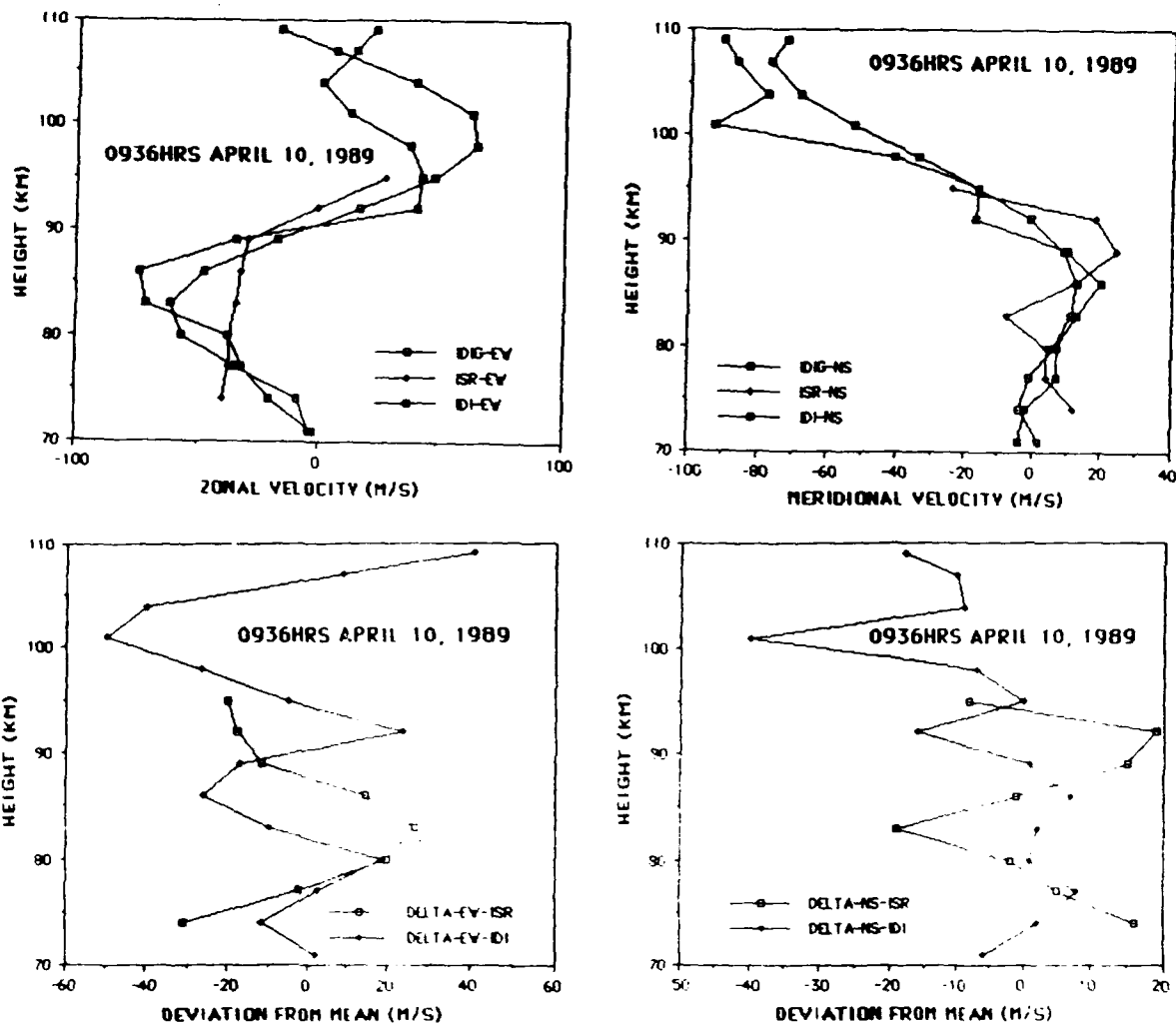
Figure 81   As for Figure 8a, except for 0936hrs on April 10.
             Note that the same (April 9-10) prevailing plus tidal
             winds apply to this comparison also.
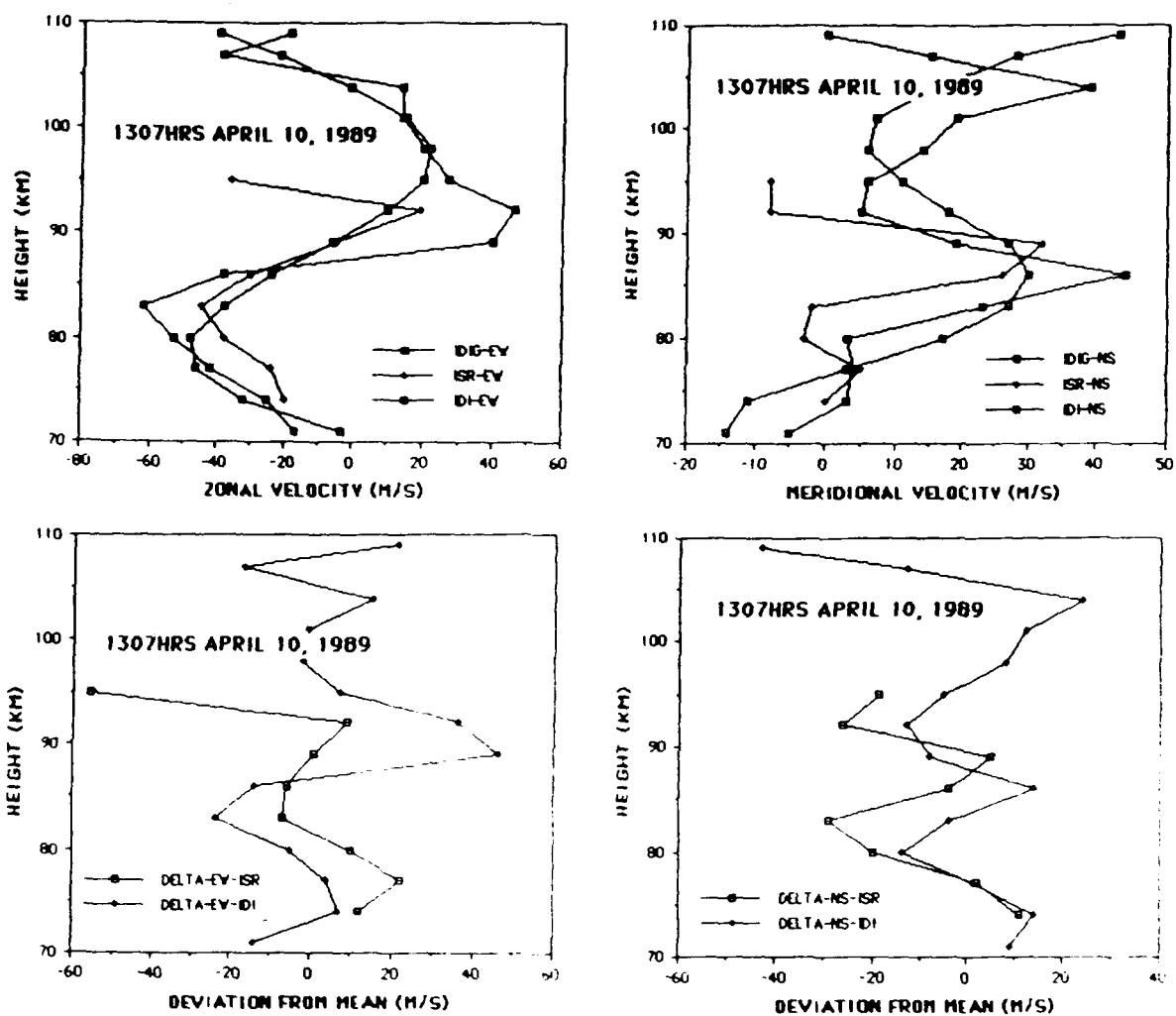
Figure 8m   As for Figure 8a, except for 1307hrs on April 10.
             A new set of Groves coefficients has been determined
             for April 10-11.

Figure 8n   As for Figure 8a, except for 1023hrs on April 11.
              Note that the same (April 10-11) prevailing plus tidal
              winds apply to this comparison also.
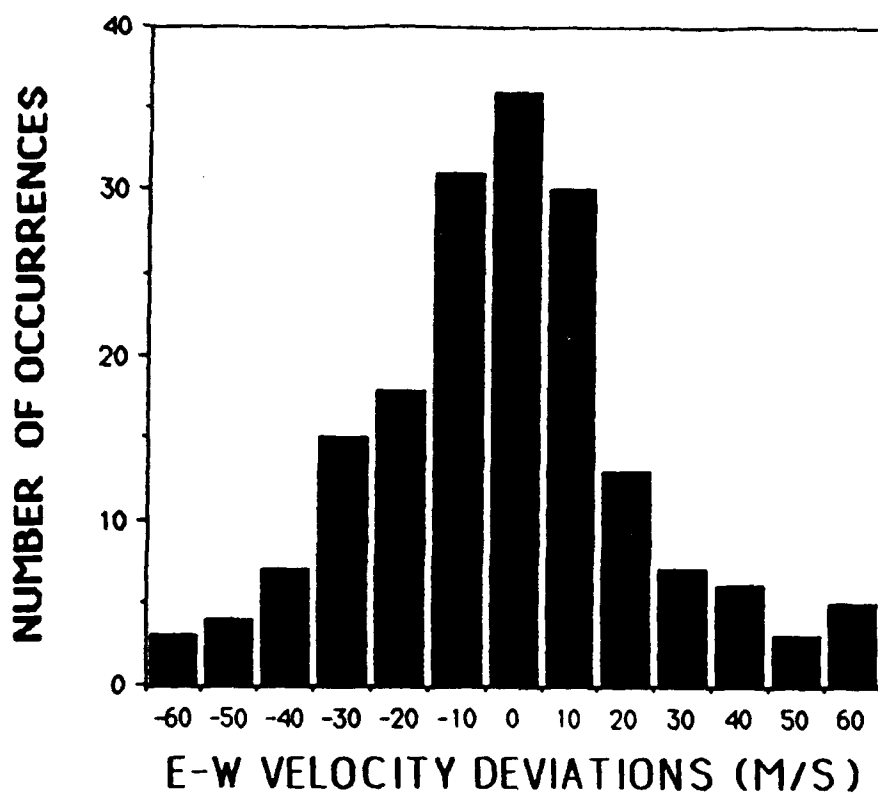
Figure 9a   The deviation of the zonal IDI wind profiles from the Groves
             mean, averaged over the 13 IDI/ISR comparative intervals
             and all heights.
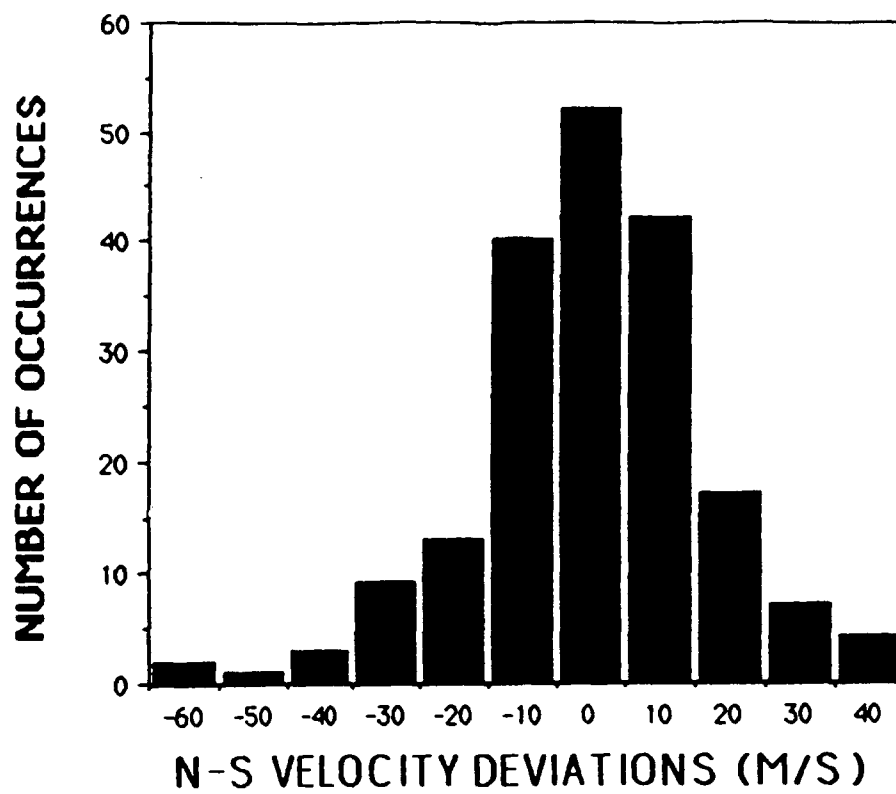
Figure 9b.   As for Figure 9a. for the meridional profiles.

ZONAL WIND, ARECIBO APRIL 5-11, 1989
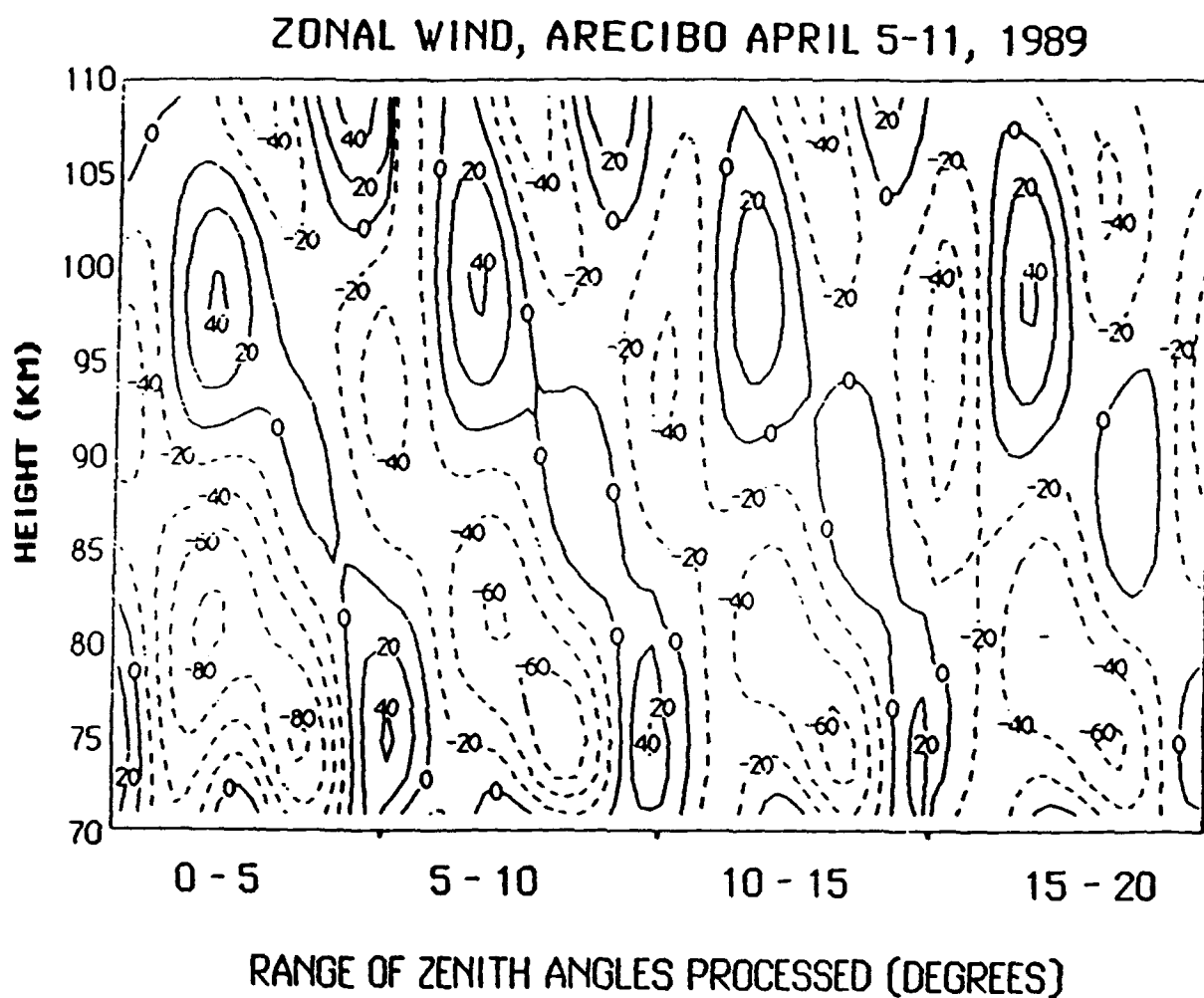
Figure 10a. Montage of the zonal wind resulting from application of the Groves analysis to the IDI data over the interval April 5 to April 11 for scattering points falling between 0 to 5, 5 to 10, 10 to 15 and 15 to 20 degrees of zenith.

MERIDIONAL WIND, ARECIBO APRIL 5-11, 1989
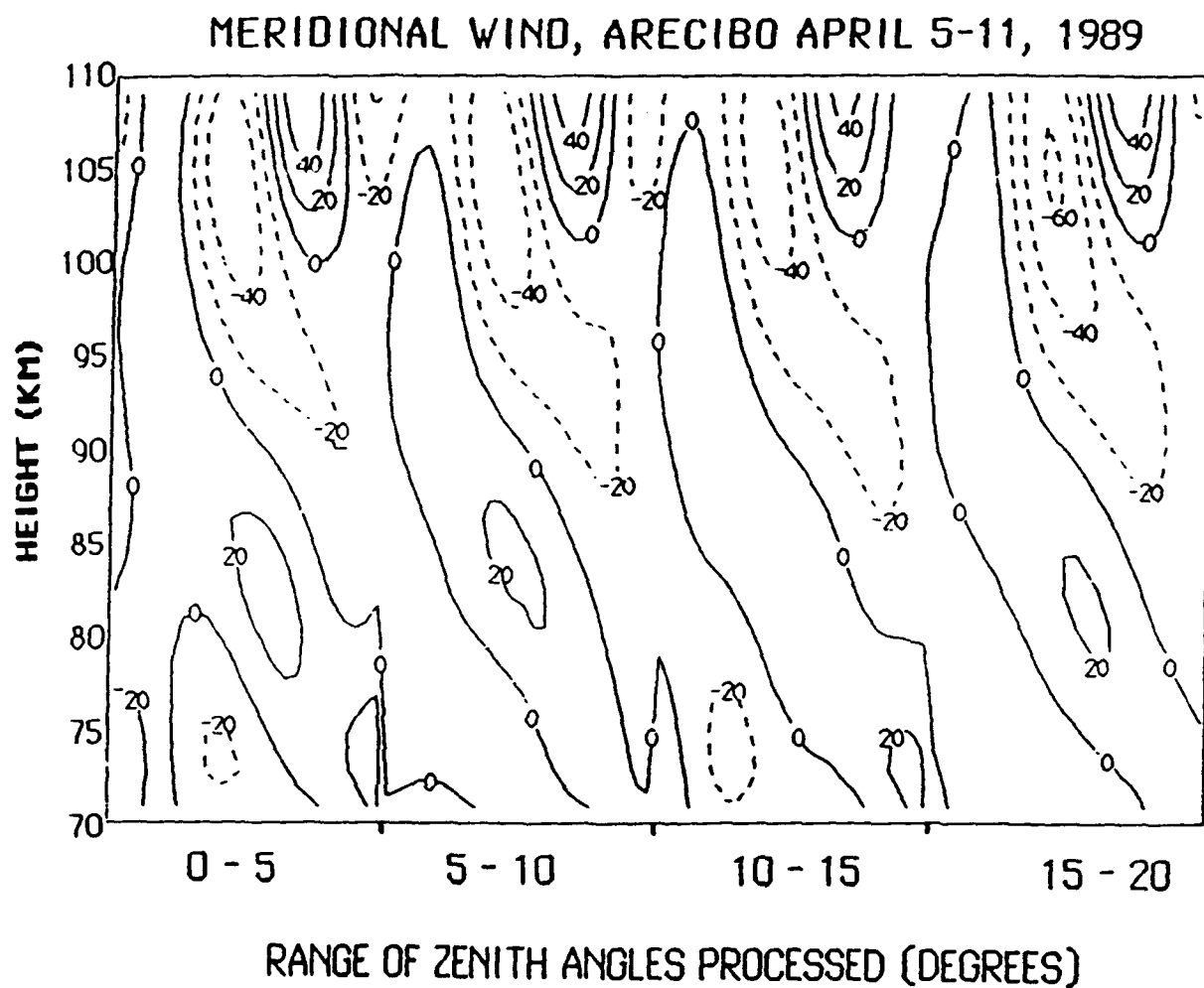
Figure 10b.   As for Figure 10a, but for the meridional wind.

VERTICAL WIND, ARECIBO APRIL 5-11, 1989

RANGE OF ZENITH ANGLES PROCESSED (DEGREES)
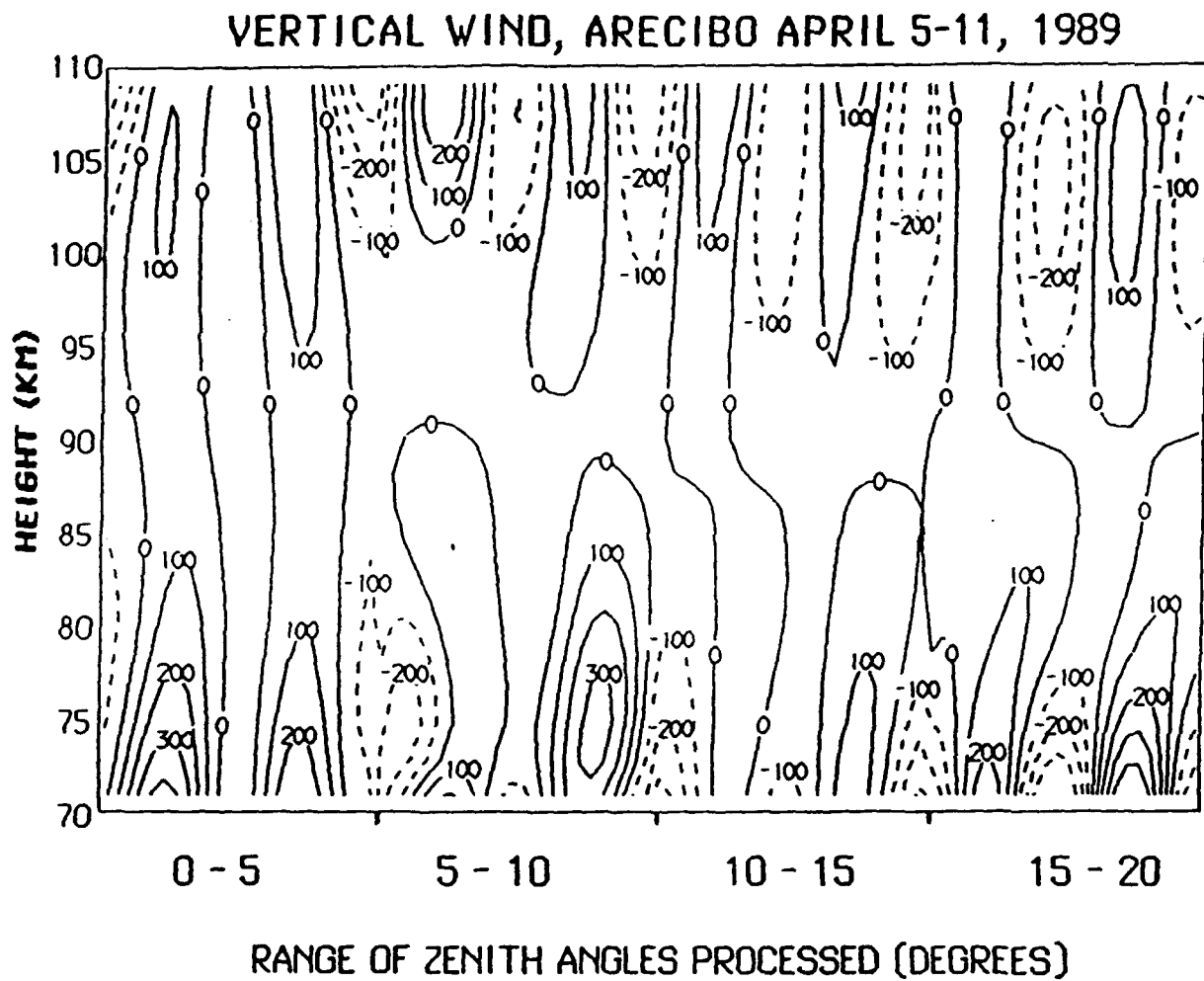
Figure 10c.   As for figure 10a, but for the vertical wind. Again, the
vertical velocity is in cm/s.
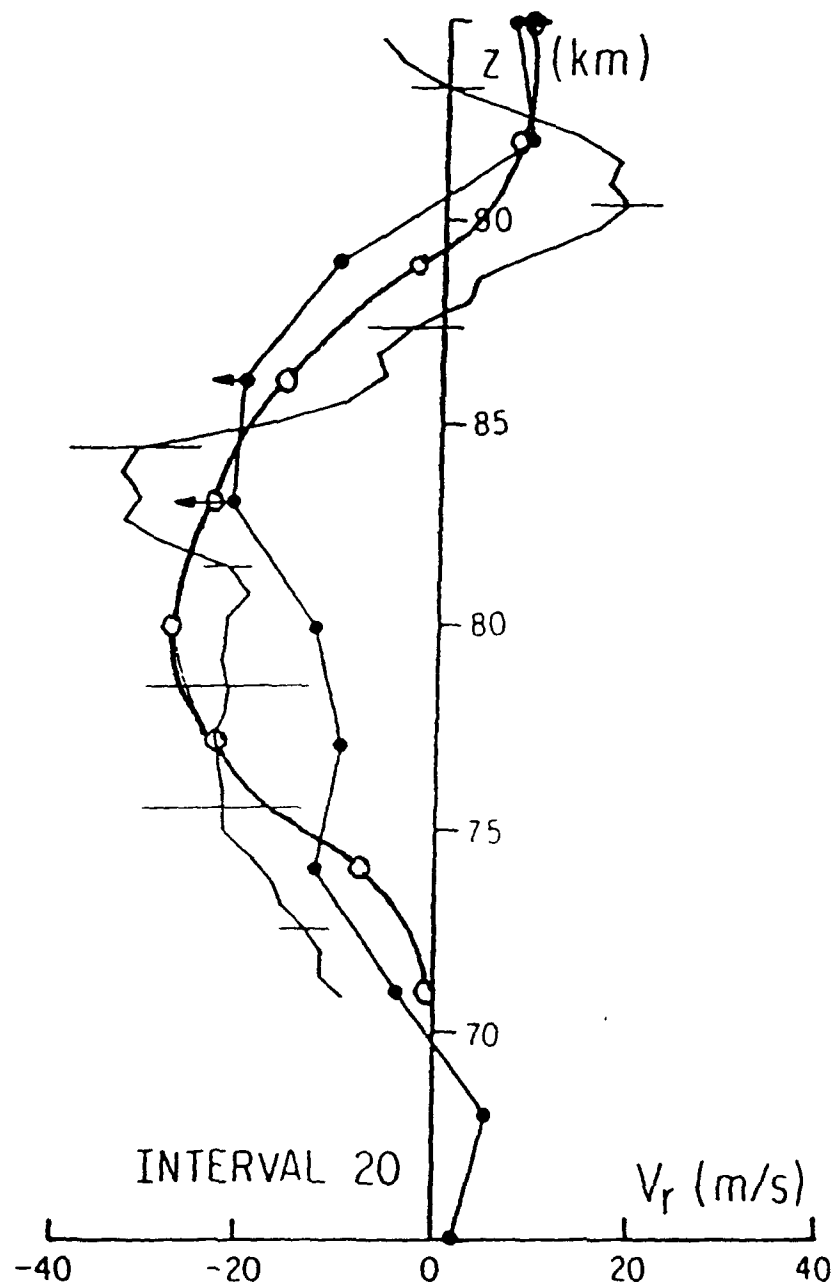
Figure 11a. Comparison between the horizontal projections of the line of sight motion as determined by the ISR (thin line) and IDI (dots) - both from Hines et al [1992] - and the Groves analysis of the IDI data (IDIG - open circles) at 0936hrs on April 10,1989. The agreement is excellent.
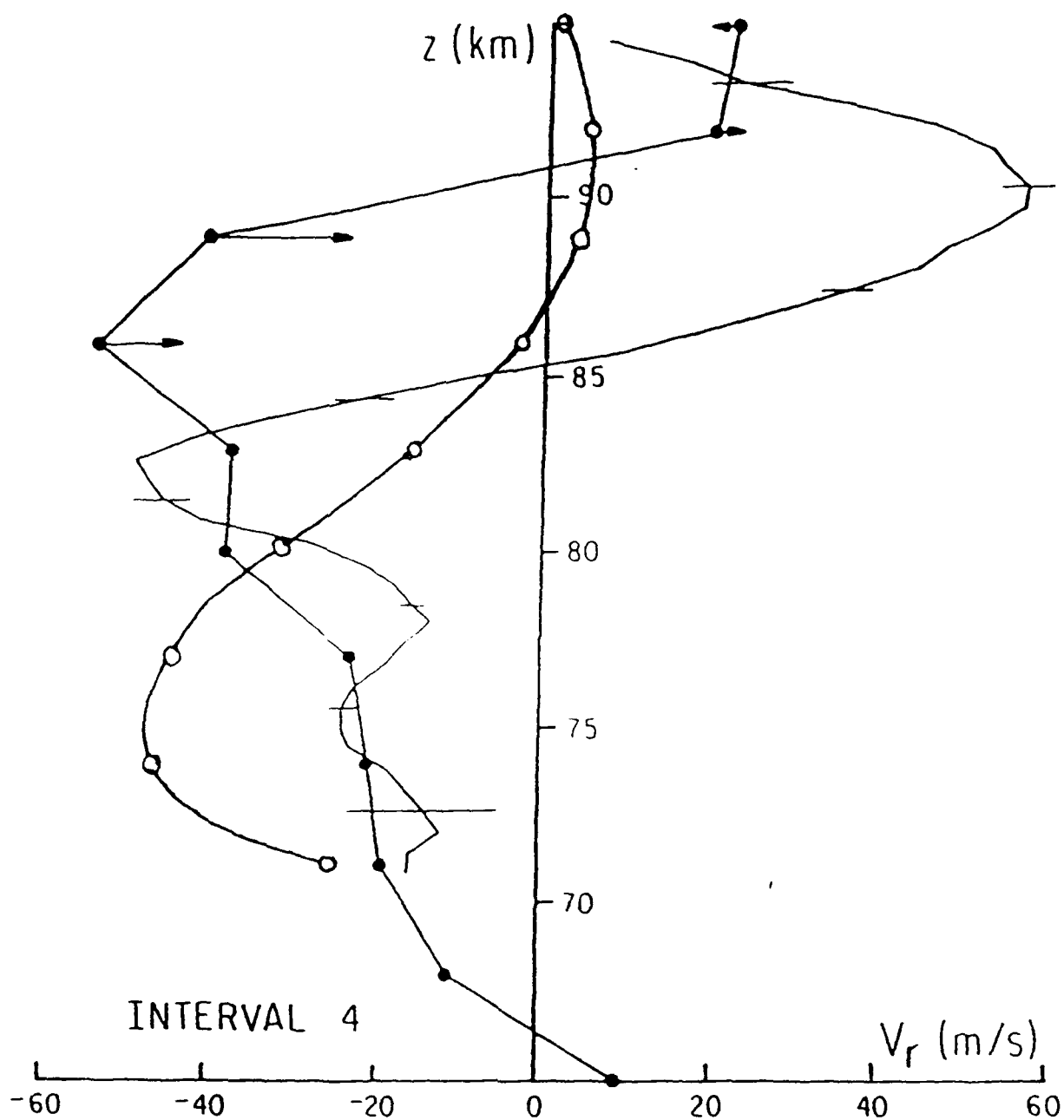
Figure 11b. As for Figure 11a, but at 1124hrs on April 6, 1989. Here, the discrepancies between the IDI and ISR measurements are as great as 80m/s (e.g. at 89km). Above 80km, the vertical phase of the IDIG profile fits that of the ISR profile better than it fits the phase of the IDI profile.
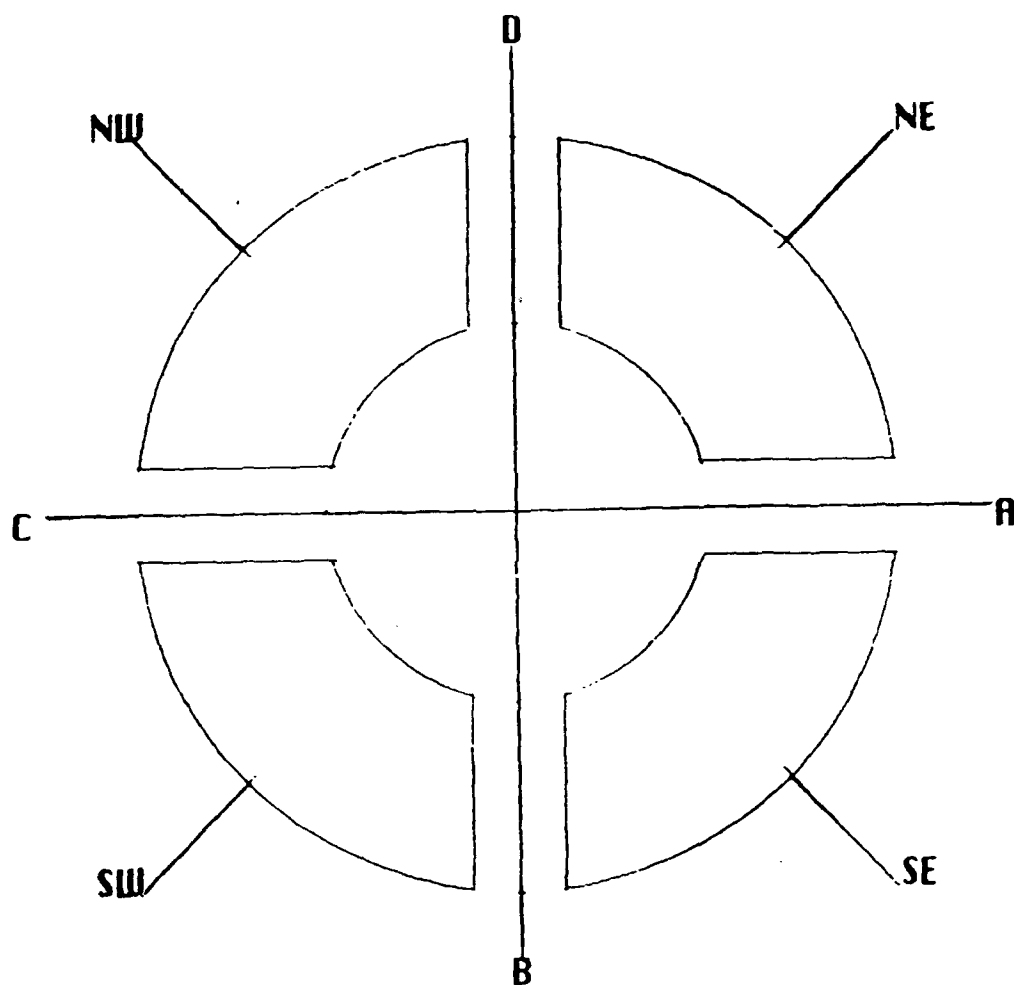
Figure 12. "Look angles" used when applying the Groves analysis as though the IDI system was a meteor radar having two orthogonal beam directions. The configuration parameters are detailed in the text.
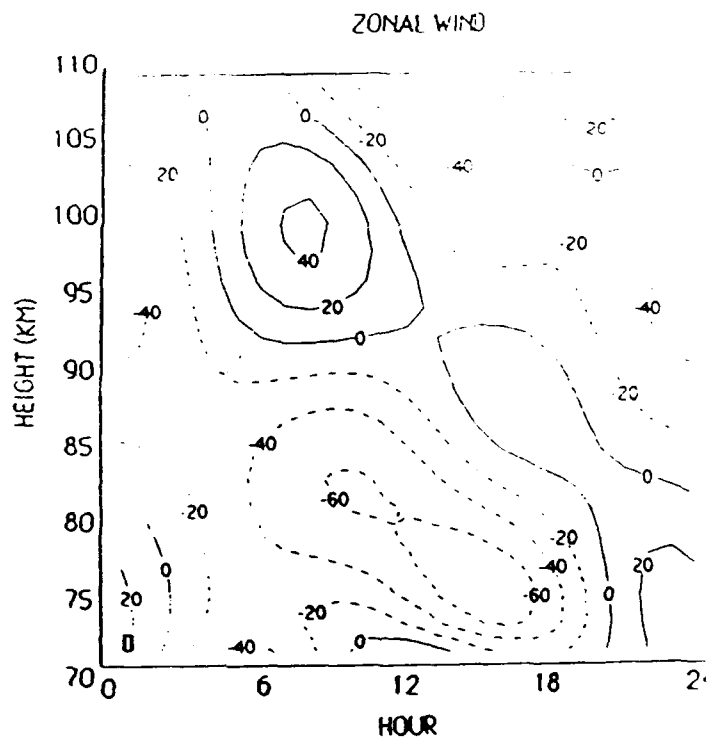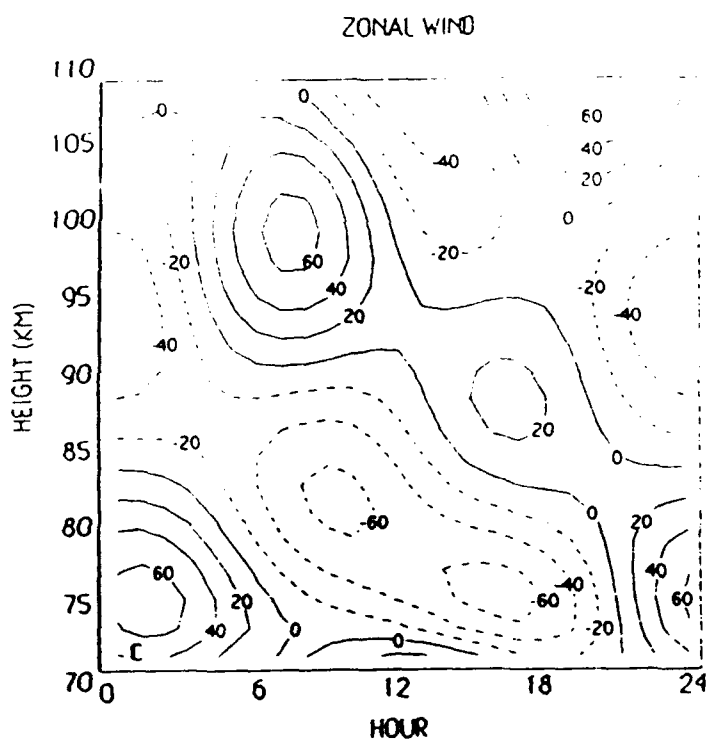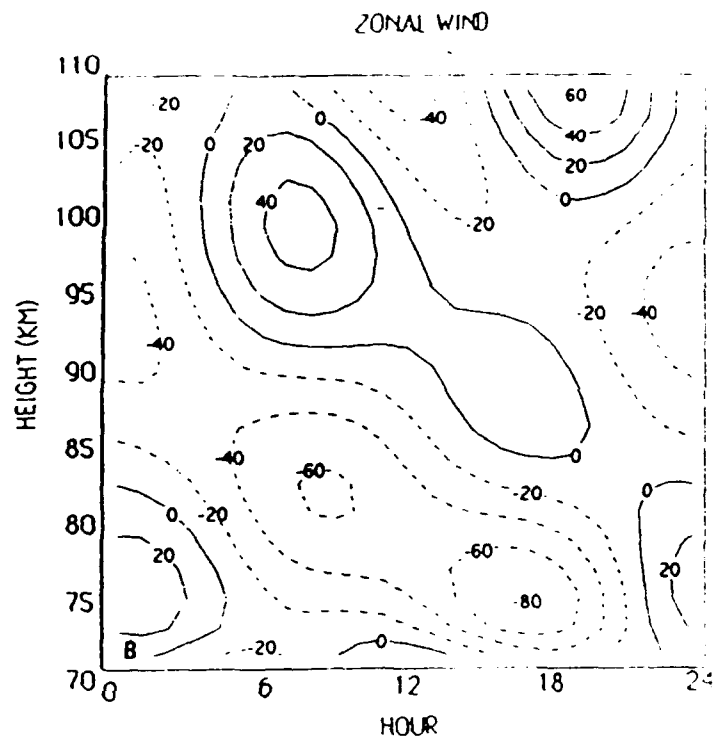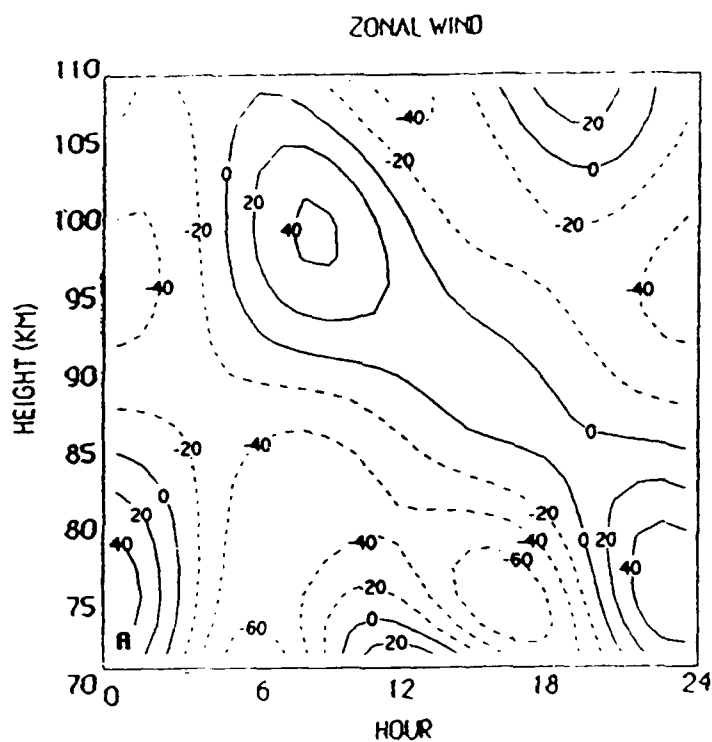
Figure 13a.   The zonal winds resulting from the four runs using antenna "beams" looking northeast and southeast (bisector A); southeast and southwest (B); southwest and northwest (C); and northwest and northeast (D), as in Figure 12.
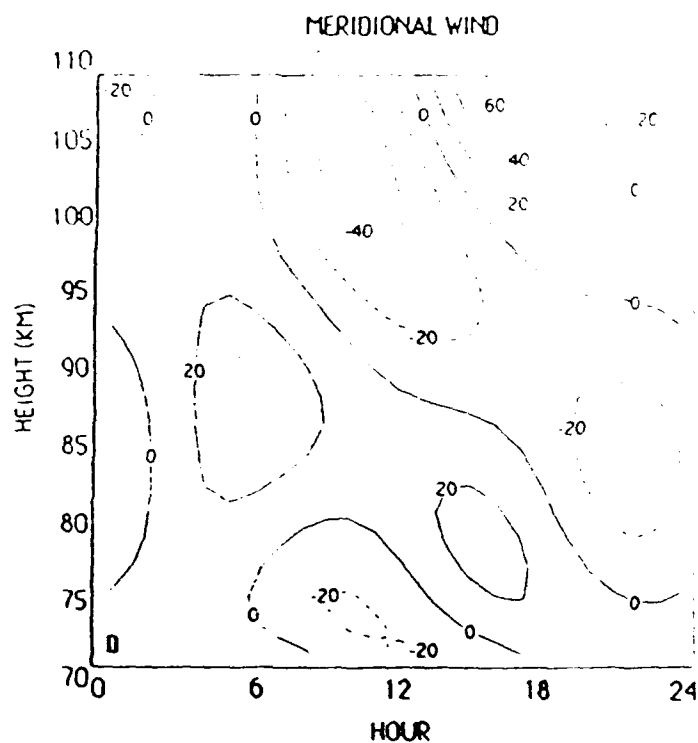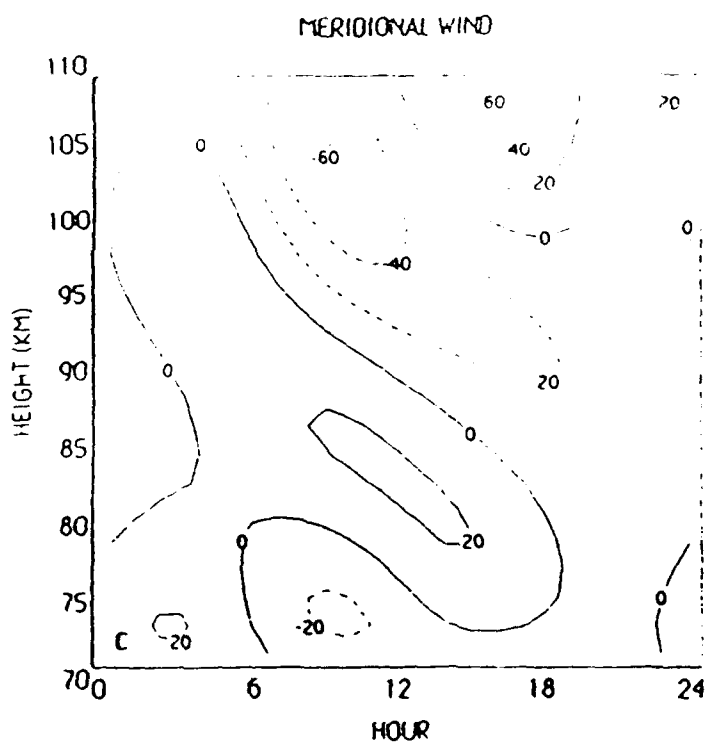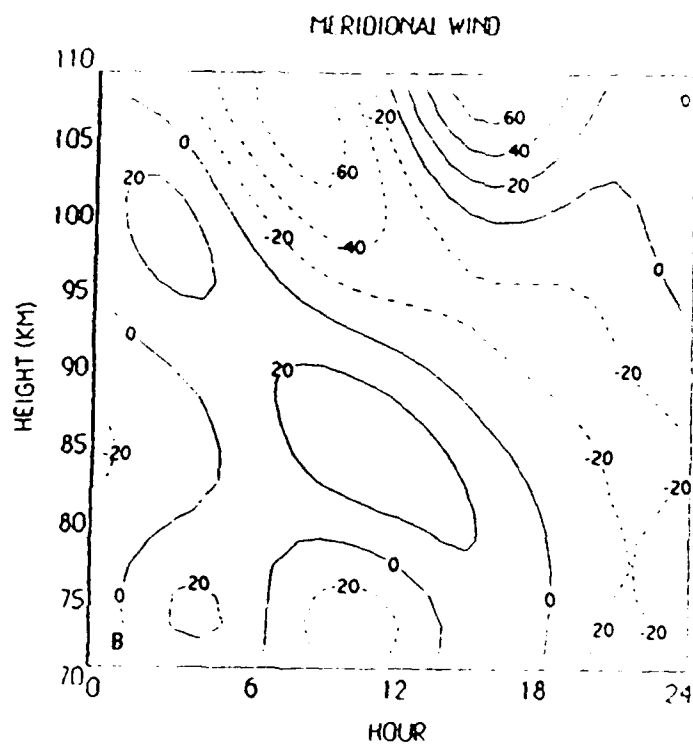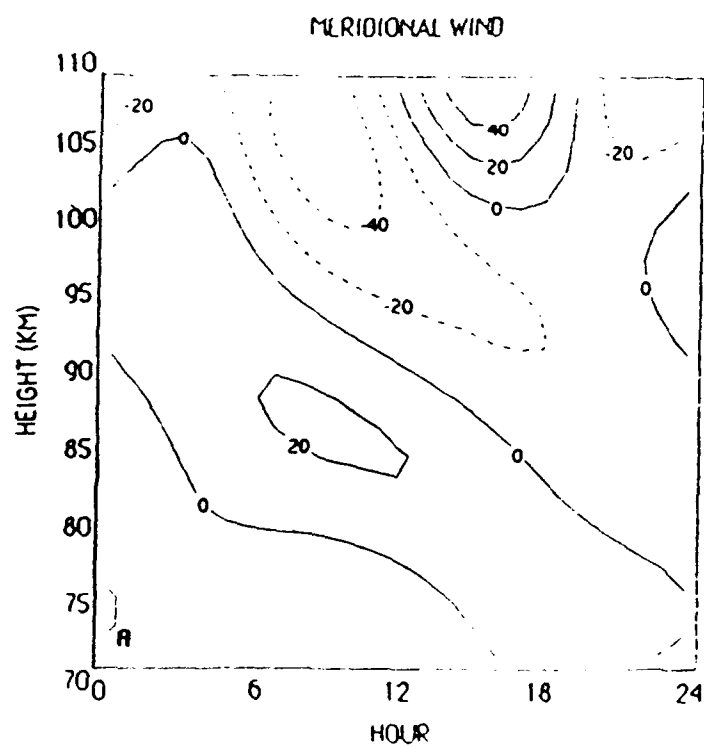
Figure 13b.　　As for 13a, but for the meridional component.